

Bulk Nanostructured Metals and Alloys: Processing, Structure, and Thermal Stability



Guest Editors: Hamed Bahmanpour, Amir Kajbafvala,
Mohammad H. Maneshian, Hamid Reza Zargar, and Khaled Youssef





**Bulk Nanostructured Metals and Alloys:
Processing, Structure, and Thermal Stability**

**Bulk Nanostructured Metals and Alloys:
Processing, Structure, and Thermal Stability**

Guest Editors: Hamed Bahmanpour, Amir Kajbafvala,
Mohammad H. Maneshian, Hamid Reza Zargar,
and Khaled Youssef



Copyright © 2012 Hindawi Publishing Corporation. All rights reserved.

This is a special issue published in "Journal of Nanomaterials." All articles are open access articles distributed under the Creative Commons Attribution License, which permits unrestricted use, distribution, and reproduction in any medium, provided the original work is properly cited.

Editorial Board

- Katerina Aifantis, Greece
Nageh K. Allam, USA
Margarida Amaral, Portugal
Xuedong Bai, China
L. Balan, France
Enrico Bergamaschi, Italy
Theodorian Borca-Tasciuc, USA
C. Jeffrey Brinker, USA
Christian Brosseau, France
Xuebo Cao, China
Shafiul Chowdhury, USA
Kwang-Leong Choy, UK
Cui ChunXiang, China
Miguel A. Correa-Duarte, Spain
Shadi A. Dayeh, USA
Claude Estournes, France
Alan Fuchs, USA
Lian Gao, China
Russell E. Gorga, USA
Hongchen Chen Gu, China
Mustafa O. Guler, Turkey
John Zhanhu Guo, USA
Smrati Gupta, Germany
Michael Harris, USA
Zhongkui Hong, USA
Michael Z. Hu, USA
David Hui, USA
Y.-K. Jeong, Republic of Korea
Sheng-Rui Jian, Taiwan
Wanqin Jin, China
Rakesh K. Joshi, India
Zhenhui Kang, China
Fathallah Karimzadeh, Iran
Alireza Khataee, Iran
- Do Kyung Kim, Korea
Kin Tak Lau, Australia
Burtrand Lee, USA
Benxia Li, China
Jun Li, Singapore
Shijun Liao, China
Gong Ru Lin, Taiwan
J.-Y. Liu, USA
Jun Liu, USA
Tianxi Liu, China
Songwei Lu, USA
Daniel Lu, China
Jue Lu, USA
Ed Ma, USA
Gaurav Mago, USA
Santanu K. Maiti, Israel
Sanjay R. Mathur, Germany
A. McCormick, USA
Vikas Mittal, UAE
Weihai Ni, Germany
Sherine Obare, USA
Abdelwahab Omri, Canada
Edward Andrew Payzant, USA
Kui-Qing Peng, China
Anukorn Phuruangrat, Thailand
Ugur Serincan, Turkey
Huaiyu Shao, Japan
Donglu Shi, USA
Suprakas Sinha Ray, South Africa
Vladimir Sivakov, Germany
Marinella Striccoli, Italy
Bohua Sun, South Africa
Saikat Talapatra, USA
Nairong Tao, China
- Titipun Thongtem, Thailand
Somchai Thongtem, Thailand
Alexander Tolmachev, Ukraine
Valeri P. Tolstoy, Russia
Tsung-Yen Tsai, Taiwan
Takuya Tsuzuki, Australia
Raquel Verdejo, Spain
Mat U. Wahit, Malaysia
Shiren Wang, USA
Yong Wang, USA
Ruibing Wang, Canada
Cheng Wang, China
Zhenbo Wang, China
Jinquan Wei, China
Ching Ping Wong, USA
Xingcai Wu, China
Guodong Xia, Hong Kong
Zhi Li Xiao, USA
Ping Xiao, UK
Shuangxi Xing, China
Yangchuan Xing, USA
N. Xu, China
Doron Yadlovker, Israel
Ying-Kui Yang, China
Khaled Youssef, USA
William W. Yu, USA
Kui Yu, Canada
Haibo Zeng, China
Tianyou Zhai, Japan
Renyun Zhang, Sweden
Yanbao Zhao, China
Lianxi Zheng, Singapore
Chunyi Zhi, Japan

Contents

Bulk Nanostructured Metals and Alloys: Processing, Structure, and Thermal Stability,

Hamed Bahmanpour, Amir Kajbafvala, Mohammad H. Maneshian, Hamid Reza Zargar, and Khaled Youssef
Volume 2012, Article ID 193734, 2 pages

Synthesis and Characterization of Metal Hydride/Carbon Aerogel Composites for Hydrogen Storage,

Kuen-Song Lin, Yao-Jen Mai, Su-Wei Chiu, Jing-How Yang, and Sammy L. I. Chan
Volume 2012, Article ID 201584, 9 pages

Consolidation of Amorphous $Al_{80}Fe_{10}Ti_5Ni_5$ Powders by Hot Pressing, M. Tavoosi, F. Karimzadeh,

M. H. Enayati, and H. S. Kim
Volume 2012, Article ID 814915, 10 pages

Elastic Modulus Determination of Al-Cu Film Alloys Prepared by Thermal Diffusion, E. Huerta,

A. I. Oliva, F. Avilés, J. González-Hernández, and J. E. Corona
Volume 2012, Article ID 895131, 8 pages

Synthesis of Bulk Nanostructured DO_{22} Superlattice of $Ni_3(Mo, Nb)$ with High Strength, High Ductility, and High Thermal Stability, H. M. Tawancy

Volume 2012, Article ID 387694, 7 pages

Align Ag Nanorods via Oxidation Reduction Growth Using RF-Sputtering, Zhan-Shuo Hu, Fei-Yi Hung,

Shouou-Jinn Chang, Wei-Kang Hsieh, and Kuan-Jen Chen
Volume 2012, Article ID 345086, 6 pages

Thermal Stability of Neodymium Aluminates High- κ Dielectric Deposited by Liquid Injection MOCVD Using Single-Source Heterometallic Alkoxide Precursors, P. Taechakumput, C. Z. Zhao, S. Taylor,

M. Werner, P. R. Chalker, J. M. Gaskell, H. C. Aspinall, A. C. Jones, and Susu Chen
Volume 2012, Article ID 891079, 4 pages

Editorial

Bulk Nanostructured Metals and Alloys: Processing, Structure, and Thermal Stability

**Hamed Bahmanpour,¹ Amir Kajbafvala,² Mohammad H. Maneshian,³
Hamid Reza Zargar,⁴ and Khaled Youssef²**

¹Department of Chemical Engineering and Materials Science, University of California, Davis, CA 95616, USA

²Department of Materials Science and Engineering, North Carolina State University, Raleigh, NC 27695-7907, USA

³Department of Materials Science and Engineering, University of North Texas, Denton, TX 76203, USA

⁴Department of Metals and Materials Engineering, University of British Columbia, Vancouver, BC, Canada V6T 1Z4

Correspondence should be addressed to Hamed Bahmanpour, hbahman@ncsu.edu

Received 21 October 2012; Accepted 21 October 2012

Copyright © 2012 Hamed Bahmanpour et al. This is an open access article distributed under the Creative Commons Attribution License, which permits unrestricted use, distribution, and reproduction in any medium, provided the original work is properly cited.

Nanostructured metals and alloys have been the focus of research during the past few decades due to their interesting microstructures and promising mechanical properties. Despite the fact that this class of materials shows intriguing properties, there are roadblocks that prevent large-scale production and industrial application of these materials that include but not limited to low ductility and poor thermal stability. In this regard, tailoring mechanical and microstructural properties by developing new alloys and inducing different microstructural features via various processing routes have been the major point of interest for researchers to overcome the difficulties in industrialization of nanomaterials. High tendency of nanograins to reduce their energy by grain coalescence and growth brings the thermodynamics and kinetics of grain growth to attention in order to understand the phenomena and develop thermally stable nanostructures. Attempts in this regard include reducing the mobility of a grain boundary by means of mechanisms such as solute drag, second-phase particle pinning, and chemical ordering. On the other hand, the demand for producing large-sized bulk parts, especially in structural applications, has led to the emergence of new processing techniques and further application-based approaches to the issue of the nanostructured metals and alloys. This special issue addresses the different challenges for up scaling the production of nanostructured metals and alloys with emphasis on processing, microstructure, and thermal stability. We would like to express our appreciation to all authors in this special issue for their help and efforts

in addressing these current issues in the field. Furthermore, thanks are extended to all reviewers for enhancing the quality of these papers.

This special issue contains six papers related to synthesis and characterization of nanostructured metals and alloys. In “*Thermal stability of neodymium aluminates high-k dielectric deposited by liquid injection MOCVD using single-source heterometallic alkoxide precursors*,” P. Taechakumput et al. studied the effects of high-temperature post deposition annealing (PDA) on the properties of the NdAlO_x thin films, deposited by metalorganic chemical vapor deposition (MOCVD) using single-source precursor. These NdAlO_x thin films were shown to remain amorphous up to 50°C as indicated by XRD. No significant level of crystallinity or movement of metal ions was evident after annealing at 950°C as indicated by MEIS energy spectra. Good electrical integrity was maintained even after 950°C PDA showing the extracted dielectric permittivity of 12, a low leakage density of $7 \times 10^{-7} \text{ Acm}^{-2}$ at 2 MV cm^{-1} , and a density of interface states at flat band D_{it} of $4.01 \times 10^{11} \text{ cm}^{-2} \text{ eV}^{-1}$. These features make the neodymium aluminate a potential candidate for the dielectric replacement.

In their paper, Z. S. Hu et al. studied “*Align Ag nanorods via oxidation reduction growth using RF-sputtering*” and demonstrated an oxidation reduction growth (ORG) technique with mixed-gas sputtering to create Ag nanorod arrays via oxide-assisted growth without any chemical solutions or contamination from aqueous solution. The ORG methodology is used to deposit an Ag buffer layer with

silver oxide nanoclusters to obtain Ag nanorod arrays using a two-step mixed gaseous process. The Ag nanorods grew in the original locations of reduced metal nuclei after thermal composition of silver oxide nanoclusters. The Ag nanorods stood vertically on the Ag buffer interlayer and grew from the interface between the Ag grains and the Ag buffer interlayer. The success of the technique provides support for the oxidation reduction growth (ORG) mechanism and proves suitable for fabrication of Ag nanorods in the semiconductor industry. Due to photoactivation caused by radiative recombination of Fermi level electrons and d-band holes, the observed photoluminescence spectra of the Ag nanorods were observed to be 2.17 eV in both air and vacuum.

In “*Synthesis of bulk nanostructured DO₂₂ superlattice of Ni₃(Mo, Nb) with high strength, high ductility, and high thermal stability*,” H. M. Tawancy showed that bulk nanostructured DO₂₂-type superlattice with high strength, high ductility, and high thermal stability can be synthesized in a Ni-Mo-Nb alloy with a composition approaching Ni₃(Mo, Nb) by a simple aging heat treatment at 700°C. Upon thermal aging, the grains of the high temperature fcc phase are subdivided into ordered crystals on the nanoscale (10–20 nm) with room-temperature yield strength of about 820 MPa and tensile ductility of 35%. Plastic deformation in the ordered state is found to predominantly occur by twinning on (111) planes of the parent fcc structure indicating that the superlattice preserves the twinning systems of the parent phase leading to the observed high ductility.

In their paper, E. Huerta et al. presented “*Elastic modulus determination of Al-Cu film alloys prepared by thermal diffusion*.” In this study, the elastic modulus of Al-50 at.% Cu alloy films with 50–250 nm thickness, prepared by thermal evaporation on Kapton 50HN flexible substrates and postthermal diffusion, was investigated. The morphology and mechanical properties of the Kapton foil substrate and metallic alloys were investigated to distinguish features and properties of the formed Al-Cu alloy from the bare substrate. Pure Al and Cu films with thickness of 50 nm were analyzed for comparison. The elastic modulus of 50–250 nm thick Al-50 at.% Cu alloys thermally evaporated on to Kapton substrates and postformed by thermal diffusion was investigated. Al₂Cu phase was the dominant crystalline phase formed as determined by XPS. Force-strain curves of the Al-Cu alloys were obtained by subtracting the force-strain curve of the Kapton substrate from the force-strain curve of the Al-Cu/Kapton material system. The elastic modulus was obtained from the slope of the corresponding stress-strain curves. Elastic modulus of the Al-Cu alloys decreased as the film thickness increased, and their values were determined to be in the range of 106.1 to 77.8 GPa for 50 to 250 nm thick alloys, respectively. The elastic modulus of the studied Al-Cu alloys was found to lie between the corresponding bulk values of the Al and Cu films. The elastic modulus measured for 50 nm thick Al was higher than its corresponding bulk value, while the elastic modulus of 50 nm thick Cu was smaller than its bulk value. The highest values of the mean grain size and rms-roughness were found for the 150 nm thick Al-Cu alloy. The methodology used to obtain the elastic modulus does

not yield alloy microfractures because of the small strains (<1%) applied during tensile testing.

In their paper, M. Tavoosi and coworkers studied “*Consolidation of amorphous Al₈₀Fe₁₀Ti₅Ni₅ powders by hot pressing*.” The purpose of their study was to investigate the feasibility of fabricating amorphous Al₈₀Fe₁₀Ti₅Ni₅ powders by mechanical alloying and consolidation into bulk samples by a hot-pressing technique. The crystallization process of this amorphous alloy is a one-stage mode of the Al₁₃(Fe,Ti)₄ and Al₃Ti intermetallic compounds. The results showed that the as-milled amorphous Al₈₀Fe₁₀Ti₅Ni₅ powders were consolidated successfully into bulk metallic glasses by a hot-pressing technique. The temperature and pressure for successful condensation of amorphous powders in the hot-pressing method were 550°C and 600 MPa, respectively. During the consolidation, the amorphous phase does not remain, and an AlTi intermetallic phase precipitates in the amorphous matrix.

In their paper, K. S. Lin et al. investigated “*Synthesis and characterization of metal hydride/carbon aerogel composites for hydrogen storage*.” The synthesis, characterization, and H₂ adsorption capacity of carbon aerogels (CAs)/metallic hydride nanocomposites as a catalyst were studied. Experimentally, The H₂ storage capacity of metallic samples was measured by a TGA microbalance method. In addition, fine structure and crystallinity of metallic hydride was identified by BET nitrogen adsorption isotherms, HR-TEM, FE-SEM/EDS, XRD, and XANES/EXAFS. The carbon aerogels were very effective in improving the hydrogen storage capacity of the Fe-, Ti-doped MgH₂ samples with the “hydrogen spillover” route. Additionally, metallic dispersion of Pd nanoparticles onto the CAs might improve the hydrogen adsorption abilities. Higher surface area from CAs and the defect criteria of the MgH₂ surface due to the doping of the metallic particle cause improvement in the hydrogen adsorption capacities. Conversely, Ti-doping onto the sodium aluminum hydride only improves slightly the hydrogen storage capabilities.

Hamed Bahmanpour
Amir Kajbafvala
Mohammad H. Maneshian
Hamid Reza Zargar
Khaled Youssef

Research Article

Synthesis and Characterization of Metal Hydride/Carbon Aerogel Composites for Hydrogen Storage

Kuen-Song Lin,¹ Yao-Jen Mai,¹ Su-Wei Chiu,¹ Jing-How Yang,¹ and Sammy L. I. Chan²

¹Department of Chemical Engineering and Materials Science, Fuel Cell Center, Yuan Ze University, Chungli 320, Taiwan

²School of Materials Science and Engineering, The University of New South Wales, Sydney, NSW 2052, Australia

Correspondence should be addressed to Kuen-Song Lin, kslin@saturn.yzu.edu.tw

Received 21 June 2012; Accepted 15 August 2012

Academic Editor: Hamed Bahmanpour

Copyright © 2012 Kuen-Song Lin et al. This is an open access article distributed under the Creative Commons Attribution License, which permits unrestricted use, distribution, and reproduction in any medium, provided the original work is properly cited.

Two materials currently of interest for onboard lightweight hydrogen storage applications are sodium aluminum hydride (NaAlH_4), a complex metal hydride, and carbon aerogels (CAs), a light porous material connected by several spherical nanoparticles. The objectives of the present work have been to investigate the synthesis, characterization, and hydrogenation behavior of Pd-, Ti- or Fe-doped CAs, NaAlH_4 , and MgH_2 nanocomposites. The diameters of Pd nanoparticles onto CA's surface and BET surface area of CAs were 3–10 nm and 700–900 m^2g^{-1} , respectively. The H_2 storage capacity of metal hydrides has been studied using high-pressure TGA microbalance and they were 4.0, 2.7, 2.1, and 1.2 wt% for MgH_2 -FeTi-CAs, MgH_2 -FeTi, CAs-Pd, and 8 mol% Ti-doped NaAlH_4 , respectively, at room temperature. Carbon aerogels with higher surface area and mesoporous structures facilitated hydrogen diffusion and adsorption, which accounted for its extraordinary hydrogen storage phenomenon. The hydrogen adsorption abilities of CAs notably increased after inclusion of metal hydrides by the “hydrogen spillover” mechanisms.

1. Introduction

Hydrogen is recognized as a clean fuel because of its almost complete combustion in air with notably high energy delivery ability. Recently, owing to the need for efficient and safe H_2 storage, enormous attention has been paid on the advantages of synthesizing composite metal hydrides [1–3]. Complex metal hydride composites in the form of ABH_4 , where A is an alkali metal and B is a group III element, have been widely studied in solution as proton acceptors to enhance H_2 adsorption abilities [4–7]. NaAlH_4 is different from any other metal hydrides and borohydrides with similar structures since it is capable of reversibly store H_2 after doping with transition metals (e.g., Ti, Fe, or Zr) [8–10]. Ti-doping also improves significantly the kinetic and cycling performance of NaAlH_4 at moderate temperatures around 373 K and ambient pressures. All these properties make it suitable as mobile, lightweight H_2 storage materials for potential application on a hydrogen fuel cell [11–23]. Practically, achievable H_2 storage capacity for Ti- NaAlH_4 is only 3.7 wt%, falls short of the theoretical value of 5.6 wt% for NaAlH_4 [20–23].

Magnesium and its alloys are potential hydrogen storage material because of their very high hydrogen storage abilities. MgH_2 is also relatively light and cheaper when compared with other metal hydrides. Magnesium is often alloyed with transition metals (e.g., Fe, Ti, Zr, Zn, or Mn) to increase the adsorption and desorption rates [24–29]. Similarly, FeTi is a viable compound with a hydrogen adsorption capacity of around 1.90 wt%. However, activation process of FeTi is necessary to get rid of the TiO_2 layer, which would otherwise hinder the hydrogenation/dehydrogenation. Consequently, higher temperatures and pressures are frequently required to achieve reproducible, maximum hydrogen adsorption/desorption capacities in the compounds [30].

Palladium-doped monolithic carbon aerogels (CAs) show a high surface area and pore volume. These characteristics are strongly influenced by the chemical nature, distribution and dispersion of the palladium particles [31–33]. Furthermore, addition of 1 wt% Pd can be effective for the hydrogen adsorption capacity of FeTi to achieve its theoretical hydrogen storage capacity of 1.9 wt% [31–33]. As carbon materials such as graphite or CAs have been shown to reduce the hydrogen adsorption and desorption

temperatures of Mg [34], it is not unreasonable to expect that CA addition could also be able to improve the hydrogen adsorption behavior of the FeTi system. There is a further advantage of using Pd-doped CAs as it has been shown that an addition of 1 wt% Pd in the FeTi can effectively enhance its hydrogen adsorption capacity [31–33].

X-ray absorption near edge structure (XANES)/extended X-ray absorption fine structure (EXAFS) spectroscopy offers a powerful tool to understand the oxidation states and fine structures of Ti atoms in the microstructure of metal hydride composites [35–38]. Thus, a thorough study of the location of Ti species in metal hydrides may be helpful to explain the enhancement of hydrogen adsorptive kinetics by identifying the compounds in the hydrides. XANES/EXAFS spectroscopy is also an excellent technique for characterizing the valency and local structure of Ti species in a complex Ti-metal hydride with short-range orders [37–41]. These studies are conducted to identify the optimum hydrogen storage capacity for hydrogen storage system. In this work, synthesis and characterization, and advantages/disadvantages of different metal-hydride systems such as Mg, TiFe, or Na-based metal hydrides, complex hydrides compounds, were investigated by field-emission scanning electron microscopy (FE-SEM), X-ray diffraction (XRD), and XANES/EXAFS spectroscopy. In addition, the adsorptive H₂ storage capacity was also studied using a high-pressure thermogravimetric analyzer.

2. Experimental

2.1. Preparation of Metal-Doped Carbon Aerogels. Metal-loaded organic aerogels were prepared following the method developed by Pekala [42] for resorcinol-formaldehyde aerogels. In a typical procedure, CA was synthesized by first stirring vigorously resorcinol (20.70 g), Na₂CO₃ (0.04 g), and equal amount of deionized water in a polypropylene jar at room temperature until resorcinol dissolved. Formaldehyde (30.94 g of purity 36.5%) was then added to the solution, followed by 0.01 M PdCl₂ (Reagent ACS R.D.H., Germany) to acquire the doping of palladium. The solution was left at room temperature for 24 h, then at 323 K for the next 24 h, and finally at 365 K for another 72 h to obtain a dark black monolith. The product was rinsed with acetone three times and soaked overnight at room temperature, yielding the hydrogel materials. After drying at room temperature, the hydrogels were isolated by heating in an oven at temperatures from 273 to 1,100 K under an Ar atmosphere for several hours to obtain the Pd-doped CAs.

2.2. Preparation of Metal Hydrides. As received TiCl₃ (Aldrich, 99.99%, anhydrous) was used as the catalyst precursor. Crystalline NaAlH₄ (Fluka, 99.9%) was purified by tetrahydrofuran (THF) (Aldrich, 99.9%, anhydrous) solution and vacuum-dried while being filtered through 0.7 μm filter paper to remove any residual Al powder and other solids from the solution. The purified NaAlH₄ was mixed with the catalyst precursor in THF to produce a Ti-doped sample containing up to 20 mol% metal (relative

to either Na or Al). The THF was evaporated while the NaAlH₄ and catalyst precursor were mixed manually for about 30 min, using a mortar and pestle, or until the sample appeared to be completely dry. A Ti-NaAlH₄ sample was then ball-milled for 2 h using a SPEX 8000 high-energy mixer/mill at a milling speed of 1,000 rpm, and the weight ratio of ball to powder was 10 : 1. 0.5–1.0 gram of sample was subjected to ball-milling each time in a 65 cm³ SUS 304 vial by ZrO₂ balls of 1.3 cm in diameter. Fe- and Ti-doped MgH₂ was prepared following Yao et al. [43], where MgH₂ was obtained by heating Mg powders (Alfa Aesar) to 400°C in a hydrogen storage rig. 90 wt% conversion to MgH₂ was achieved according to the volumetric calculations. 1.5–2.0 grams of nanophase iron powder (100 nm), Ti (Aldrich Co), and MgH₂ samples were mixed in the composition of MgH₂-5.0 wt% (2Fe + Ti, molar ratio) and mechanically ball-milled by using a ZrO₂ ball mixer/mill (model SPEX 8000). The samples were subjected to ball-milling as described above for 2 h, using a weight ratio of ball to powder of 8 : 1. The powder was then ball-milled again with 5.0 wt% of CAs for an additional 10 h at a milling speed of 1,000 rpm. All procedures described above were carried out in a flowing argon gas glove box to prevent the metal hydride samples from oxidation. The samples were then used for hydrogen adsorption property tests and microstructure characterization.

2.3. Hydrogen Adsorption Measurements. The hydrogen isotherms were measured gravimetrically at different temperatures using a method previously described by Eddaoudi et al. [44]. A Cahn Thermax 500 microgravimetric balance with a sensitivity of 1 μg was used to measure the change in mass of samples suspended within a glass enclosure under a certain atmosphere. A pressure sensor, with a range of 0 to 68 atm (at 1,000°C) and sensitivity of 0.011 atm, was used to measure the hydrogen pressure in the chamber. Samples were outgassed overnight until a constant mass was attained; these varied from 0.2 to 2.0 g. Prior to admittance of argon gas, the entire chamber and manifold were evacuated overnight. The system was purged at room temperature three times with the argon gas before cooling to 77 K, and gases were passed through a molecular sieve trap immersed in liquid nitrogen to remove any condensable impurities or moisture before being exposed to the sample. Pressures were measured with the range covering 1 to 30 atm. Hydrogen was added incrementally, and data points were recorded when no further change in mass was observed. The dynamic hydrogen adsorption data on Pd-, Ti-, Fe-doped CAs, NaAlH₄, or MgH₂ batch adsorption experiments were also conducted at room temperature (298 K) and different pressures. The adsorbed amount of hydrogen was calculated after the buoyancy correction.

2.4. Characterization of Carbon Aerogels and Metal Hydrides. The morphologies, crystallinity, particle size distribution, and the compositions of as-synthesized metal hydrides and metal-doped CAs were determined by FE-SEM equipped with EDS (Hitachi, S-4700 Type II) and HR-TEM (Zeiss

10C). XRD (MAC Science, MXP18) was performed to identify the phases and crystallinities in the samples. Complex of metallic hydride and CAs was scanned from 20 to 80° (2θ) with a scan rate of 4° (2θ) min^{-1} , and monochromatic $\text{CuK}\alpha$ radiation was used. The recorded specific peak intensities and 2θ values can be further identified by a computer database system (JCPDS). The surface areas of the CAs were measured by BET (Brunauer-Emmett-Teller) nitrogen adsorption (Micromeritics ASAP 2010 Instrument). For the BET surface area measurement, the samples were scraped from the sample tube substrate and powdered so as to avoid any influence from the steel tube. Prior to measurement, all samples were degassed at 423 K for 1 h. For the calculation of the BET surface areas, the relative pressure range P/P_0 from 0.05 to 0.2 was used. The pore radius distribution was determined by Barrett, Joyner, and Halenda (BJH) method.

The XANES/EXAFS spectra were collected at BL16A1 and BL01C1 (SWLS) beamlines at the National Synchrotron Radiation Research Center (NSRRC) of Taiwan. The electron storage ring was operated with the energy of 1.5 GeV and a current of 100 – 200 mA. A Si(111) double crystal monochromator (DCM) was used for providing highly monochromatized photon beams with energies of 1 to 15 keV (BL16A1) and 5 to 30 keV (BL01C1) and resolving power ($E/\Delta E$) of up to $7,000$. Data were collected in fluorescence or transmission mode with a Lytle ionization detector [39] for Ti ($4,966$ eV) and Pd ($24,350$ eV) K-edge experiments at room temperature. The photon energy was calibrated by characteristic pre-edge peaks in the absorption spectra of Ti standards. The raw absorption data in the region of 50 to 200 eV below the edge position were fit to a straight line using the least-square algorithms [37–40]. The XANES was extended to energy of the order of 50 eV above the edge. The k^2 -weighted and EXAFS spectra were Fourier transformed to R space over the range between 2.5 and 12.5 \AA^{-1} . The EXAFS data were analyzed by using the UWXAFS 3.0 program and FEFF 8.2 codes [37–41].

3. Results and Discussion

3.1. Morphology of Metal-Doped Carbon Aerogels and Metal Hydrides. The HR-TEM image and FE-SEM micrographs of metal hydride and CAs complexes synthesized are shown in Figure 1. Figure 1(a) is an HR-TEM observation of the Pd-doped aerogel structure consisting of spherical primary Pd(0) nanoparticles. It can be seen that palladium particles of size 3 to 10 nm were uniformly distributed throughout the gel. FE-SEM micrograph in Figure 1(b) reveals the pellet-like or irregularly shaped Ti-NaAlH₄ crystalline nanoparticle, with diameters approximately 50 – 80 nm. Correspondingly, Fe and Ti nanoparticles with an average diameter of 50 – 80 nm were dispersed uniformly on the surface of the doped MgH₂ surface as shown in Figure 1(c).

3.2. X-Ray Powder Diffraction. The structure of the compound was confirmed by structural refinement of X-ray diffraction patterns shown in Figure 2. The intensive peaks

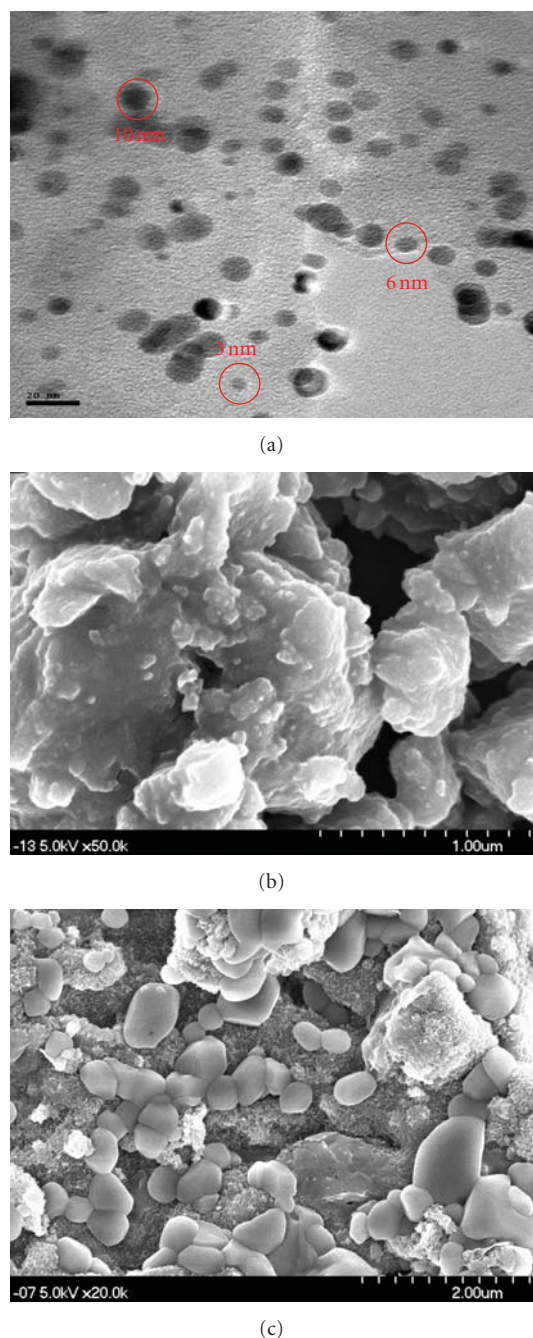


FIGURE 1: (a) HR-TEM image of 5 wt% Pd-doped carbon aerogels, FE-SEM microphotos of (b) 20 mol% Ti-NaAlH₄, and (c) 5 wt% FeTi-CAs-MgH₂ (Fe : Ti = 2 : 1, molar ratio).

appearing at small 2θ angles were characteristics of porous materials which possess numerous pores or cavities. Whereas Figure 2(a) shows the characteristic peaks of $2\theta = 27.46$, 31.75 , 45.53 , 56.54 , 66.29 , 75.36 , and 84.06° , respectively, which indicates that the structure of Ti-NaAlH₄ composites might not be affected by Ti added during ball-milling. From the intensity of (200) peak, the minimum grain size was measured to be around 60 nm [17–20]. This grain particle size was calculated from Scherrer's equation (with Warren's

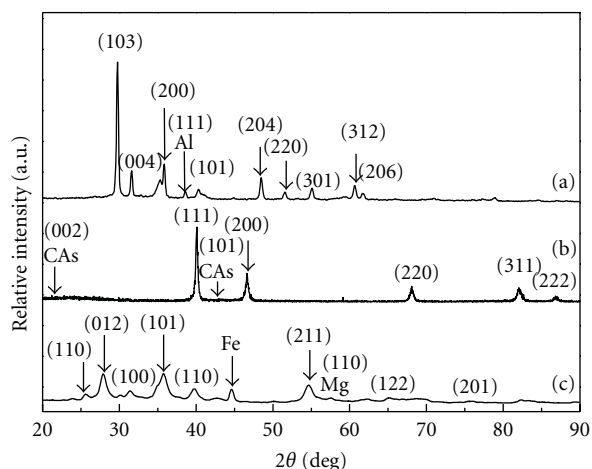


FIGURE 2: XRD patterns of (a) 20 mol% Ti-NaAlH₄, (b) 5 wt% Pd-doped carbon aerogels, and (c) 5 wt% FeTi-MgH₂ (Fe:Ti = 2:1, molar ratio).

correction for instrumental broadening) applied to the half-height of the maximum intensity diffraction peak. Metallic Na₃AlH₆ and Al were consistent with the characteristic peak at 32.92 and 38.6°, respectively [24]. From the FE-SEM measurement and XRD patterns, the titanium compound distributed on the surface of the NaAlH₄ can be confirmed.

The X-ray diffraction patterns of the Pd-doped CAs indicate that the Pd nanoparticles have a crystalline structure (Figure 2(b)). According to FE-SEM micrographs, the well dispersion of metallic Pd nanoparticles in the CAs apparently facilitated the porous structure. The XRD patterns of Pd-doped CAs show those two characteristic 2θ sharp peaks with higher intensities around 40.12 and 46.77°, indicating a largely crystalline structure. The mean particle size was about 5–8 nm from HR-TEM observation that may help the mesoporous structure of CAs to adsorb hydrogen. The diffraction angles at around 20 and 44°, corresponding to the (002) and (101) diffraction peaks of graphite, respectively, are represented in Figure 2(b). In addition, hexagonal structure of the CAs started to become disordered with the heat treatment, owing to the progressive graphitization of the sample. Figure 2(c) represents the XRD patterns of FeTi-doped MgH₂ structure. The peak of the Fe sample at 44.6° indicates that the decomposition of Fe onto the metal hydrides, whereas characteristic peaks of β -MgH₂ were observed at 27.81, 31.23, 39.7, 54.57, 65.45, and 75.54°, respectively. Thus, β -MgH₂ morphology was dominated in the sample, and the metallic Mg with β -MgH₂ structure represents the peaks at 36, 57.76, and 25.67°, respectively [43].

3.3. XANES and EXAFS. Figures 3(a)–3(e) show the pre-edge XANES spectra of Ti K-edge (4,966 eV) in nanophase Ti-NaAlH₄ nanoparticles and anatase-typed TiO₂ standard [45]. These spectra exhibit an absorbance feature of 4,966 eV for the $1s$ to $3d$ transition, which is forbidden by the selection rule in case of perfect octahedral symmetry. The sharp feature at 4,987 eV, due to the dipole allowed of $1s$ to $3p_{xy}$ electron transition, indicates the existence of Ti(IV). The

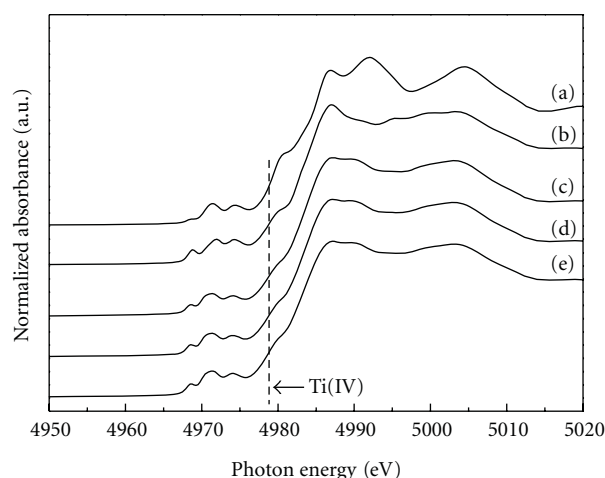
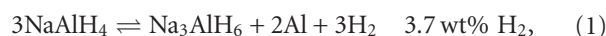


FIGURE 3: Ti K-edge XANES spectra of (a) rutile and (b) anatase-typed TiO₂ standards; (c) 20, (d) 12, and (e) 8 mol% Ti-NaAlH₄ metal hydride composites after ball-milling for 2 h using a high-energy mixer/mill.

intensity of the $1s$ to $3p_{xy}$ transition is proportional to the population of Ti(IV) of the Ti-NaAlH₄ complexes. Oxygen atoms are the major atoms coordinated to the central Ti atoms in the Ti-NaAlH₄ complexes.

The reversible hydrogenation of NaAlH₄ and dehydrogenation to NaH and Al occurred in two steps summarized as follows [1–6].



Remarkably, the addition of the Ti species lowers the activation energy of the adsorption/desorption processes and enhanced the kinetic rates of these reactions by several orders of magnitude [46–50]. However, the exact mechanism still required further investigations. Notably, the hydrogen-depleted multicomponent products resulting from (2) were found to form large crystallites of the complex metal hydride upon the reverse reaction in the presence of Ti during hydrogenation [45–47]. This is an important clue to understand the role of Ti where it implies a concerted migration of metal atoms over large distances. Local structural arrangements without the involvement of large-scale atomic migration would instead result in an amorphous or nanocrystalline structure.

The main scientific issues concerning the chemical forms (or speciation) of active species ultimately depend on molecular-scale structure and properties. Basic understanding at this scale is essential for further understanding the catalytic behaviors of Ti-NaAlH₄ complexes synthesized at different mol% values of Ti. Generally, Ti K-edge EXAFS spectroscopy in Figure 4 can provide the information on the Ti atomic arrangement of catalysts in terms of bond distance, bond angle, coordination number, kind of near neighbors, and thermal or static disorders. Experimentally, the Ti species with a central Ti atom have a Ti–O bond

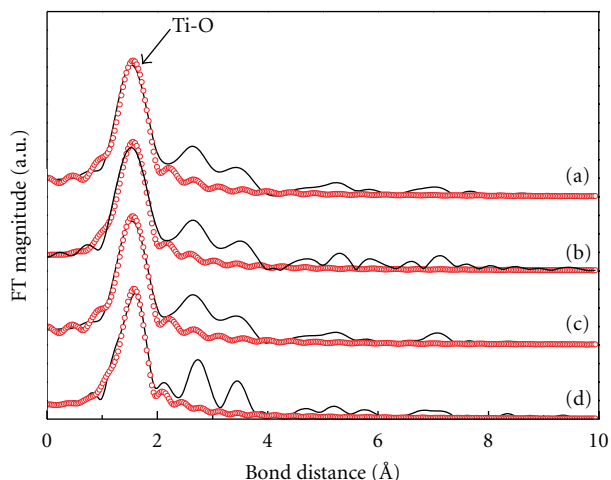


FIGURE 4: Fourier transformation (FT) spectra of (a) Ti-NaAlH₄, (b) 20, (c) 12, and (d) 8 mol% Ti-NaAlH₄ metal hydride composites after ball-milling for 2 h using a high-energy mixer/mill. The best fitting of the EXAFS spectra are expressed by the dotted lines.

distance of $1.95 \pm 0.02 \text{ \AA}$ and a coordination number of 4.07, in a Ti-NaAlH₄ composite after ball-milling for 2 h using a high-energy mixer/mill. Comparatively, however, a rutile-typed TiO₂ has a central Ti atom with a Ti-Ti and a Ti(O)-Ti bonds, and their bond distances are $2.96 \pm 0.02 \text{ \AA}$ and $3.57 \pm 0.02 \text{ \AA}$, respectively [29–32, 40]. Since the differences of mass density (ρ) and band structures between anatase- and rutile-typed TiO₂, bond distances of Ti-O are $1.95 \pm 0.02 \text{ \AA}$ and $1.93 \pm 0.02 \text{ \AA}$, respectively [9–14].

The EXAFS data shown in Figure 4 reveals that the peak intensity of first-shell Ti-O bond increased with decreasing mol% values of Ti-dopants for a Ti-NaAlH₄ composite after ball-milling for 2 h using a high-energy mixer/mill. These results may offer a further explanation on the higher oxidation states of Ti species for a Ti-NaAlH₄ complex after ball-milling at higher rates and temperatures. Moreover, each Ti(IV) ion in the framework of nanophase Ti-NaAlH₄ complex crystals is surrounded by six O²⁻ ions [9–14]. Since the bond lengths of the first and second shells for Ti-O bonding are $1.94 \pm 0.02 \text{ \AA}$ and $1.97 \pm 0.02 \text{ \AA}$, similarly with the coordination numbers of four and two, respectively, an octahedral structure of the Ti-NaAlH₄ composites was found using EXAFS measurement [45]. As shown in Table 1 and Figure 5, the Ti species with a central Ti atom have a Ti-O bond distance of $2.81 \pm 0.02 \text{ \AA}$ and a coordination number of 1.83, in a Ti-NaAlH₄ composite in 8 mol% Ti-NaAlH₄ metal hydride composites (more than 2 mol%) after the hydrogen adsorption processes. It can be seen that all Ti species in Ti-NaAlH₄ metal hydride composites can be reduced in the hydrogen adsorption processes and be kept in the metallic Ti form.

3.4. N₂ Gas Adsorption Isotherms Analyses. Nonspecific physical adsorption of the CAs was carried out to measure the total surface area and pore size distribution for Pd-doped CAs, as shown in Figure 6. The surface area, pore size distribution, and crystalline diameter of CAs were calculated according to the adsorption data summarized

in Table 2. A large surface area was generally observed for Pd-doped CAs and beneficial characteristic for a great variety of applications. The microcrystalline structure of Pd on the CAs is confirmed from the HR-TEM analysis (Figure 1(a)), resulting in an increase of the surface area. The nitrogen adsorption-desorption isotherms exhibit a hysteresis behavior, indicating the microstructural nature of the porous specimens. Moreover, the type IV hysteresis isotherm obtained is represented in Figure 6(a). The adsorption hysteresis was observed in the region of a relative pressure P/P_0 above 0.4. The specific surface areas of CAs and Pd-doped CAs are 687 and 725 m² g⁻¹, with the pore volumes of 0.62 and 0.64 cm³ g⁻¹, respectively, as shown in Table 2. It also indicates that these resulting factors of surface enhancement depended on the doping of the Pd on the CAs and consisted of higher porous structure [49, 50]. These results may be caused by the dispersion of the Pd on the CAs surface and that indicated the metallic dispersion would be helpful for adsorption criteria.

The intensive peak of the Pd(0) K-edge region around 24,368 eV and the stronger peak at 24,392 eV were due to the orbital $3d \rightarrow 5s$ or $4p$ hybridization caused by unoccupied d bands, as shown in Figure 7. These quantified the doping of Pd on the surface of carbon aerogels. Therefore, in the absorption where the orbital $3d \rightarrow 5s$ or $4p$ hybridization was intensive, the p -like density of states was notably enhanced and the absorption increased like the second absorption peak in the XANES/EXAFS spectra of the Pd standards (Figures 7(b) and 8(a)). The structural parameters of the Pd powder and the palladium doped CAs, obtained from the best fit to the EXAFS data, are shown in Table 1. The coordination numbers and bond lengths also were well compared with the Pd metal and palladium-doped CAs crystal structure data. The Debye-Waller factors ($\Delta\sigma^2$) were less than 0.015 (\AA^2), which indicated that the palladium confirmatively has center Pd atoms coordinated by Pd-Pd bonding. The bulk Pd metal possessed Pd-Pd bond distance of $2.74 \text{ \AA} \pm 0.02 \text{ \AA}$ and a coordination number of 9.59. For comparison, fresh CAs-Pd clusters were found to have a Pd-Pd bond distance of 2.12 \AA with a coordination number of 6.18. This shortening of the bond distance with a lower coordination number was caused by random motion of surface atom on the small Pd particles and was responsible for the increase in the surface area of the palladium doped CAs samples, whereas hydrogen reduced bulk CA-doped Pd cluster consisted with the Pd-Pd bond distance of 2.73 \AA and a coordination number of 9.23. This revealed that the Pd nanoparticles were notably activated in the reduction process [48]. Moreover, the shortening of the bond distance with coordination number probably was caused by the random motion of surface atom on the small Pd particles and therefore increases the surface area of the Pd-doped CAs samples. Furthermore, this result also revealed that the Pd nanoparticles were well dispersed on the surface of CAs, which might improve the amount of hydrogen storage efficiency significantly.

3.5. Hydrogen Gas Adsorption Isotherms Analyses. Comparisons of the hydrogen adsorption of metal hydride and

TABLE 1: Fine structural parameters Pd/Ti atoms in Pd/Ti powder standards, 5 wt% Pd-doped carbon aerogels with or without hydrogen reduction, and 20 mol% Ti-NaAlH₄ metal hydride composites analyzed by using EXAFS.

Samples	Shell	CN ^a (± 0.05)	R ^b (± 0.02 Å)	σ^2 (Å ²) ^c
Pd species				
Pd powder standard	Pd-Pd	9.59	2.74	0.0056
Fresh 5 wt% Pd-doped CAs ^d	Pd-O	6.18	2.12	0.0061
H ₂ reduced 5 wt% Pd-doped CAs ^e	Pd-Pd	9.23	2.73	0.0073
Ti species				
Metallic Ti standard	Ti-Ti	1.78	2.93	0.0044
TiO standard	Ti-O	2.14	2.53	0.0083
Ti ₂ O ₃ standard	Ti-O	3.02	2.12	0.0023
Rutile-typed TiO ₂ standard	Ti-O	4.11	1.94	0.0015
Anatase-typed TiO ₂ standard	Ti-O	4.15	1.93	0.0026
Ball-milled 20 mol% Ti-NaAlH ₄	Ti-O	4.07	1.95	0.0048
H ₂ -adsorbed 20 mol% Ti-NaAlH ₄	Ti-Ti	1.83	2.81	0.0051

^aCN denotes ‘‘coordination number’’;

^bR denotes ‘‘bond distance’’;

^c σ denotes ‘‘Debye-Waller factor’’;

^dFresh 5 wt% Pd-doped carbon aerogel samples denote the as-synthesized materials that were oxidized and converted into PdO species instantly in the synthetic processes;

^e5 wt% Pd-doped carbon aerogel samples were reduced at 453 K under flowing hydrogen gas for six hours.

TABLE 2: Values of specific surface area and pore size distribution of as-synthesized carbon aerogel samples calculated using BET or BJH nitrogen isotherms method.

Samples	S_{BET} ^a (m ² g ⁻¹)	V_t ^b (cm ³ g ⁻¹)
Carbon aerogel	687	0.69
5 wt% Pd-doped carbon aerogel	725	0.71

^a S_{BET} : specific surface area computed and calculated by using BET nitrogen isotherms equation;

^b V_t : total pore volume estimated and calculated at a related pressure of 0.98 by using BJH nitrogen isotherms equation.

doped metal hydride with carbon aerogel are given in Figures 9(a)–9(e). Under a typical reaction condition of 298 K and 1–30 atm, the hydrogen adsorption curves of pure MgH₂ (Figure 9(e)) were consistent with lowest adsorption criteria, whereas the FeTi with CA-doped MgH₂ (Figure 9(a)) possessed the highest hydrogen adsorption capacity of 4.02 wt%. Mesoporous structure of the CAs, which has a very high surface area as confirmed from the BET nitrogen isotherm analysis, improved the hydrogen adsorption behavior. This is inline with the finding of Imamura et al. [34], who reported that the uptake of hydrogen in a C-Mg composite took place at a significantly lower temperature than that in pure magnesium. Similarly, Jung et al. [51] suggested that the faster adsorption kinetics of MgH₂ systems may result from the very high defect densities of the damaged MgH₂ surfaces caused by the ball-milling of Mg with hard and small oxide particles. Defects provide hydrogen an easy path to go into Mg powders. Therefore, the hydrogen adsorption capacity of 2.7 wt% was obtained with the addition of FeTi nanoparticles into the MgH₂ samples by ball-milling (Figure 9(b)). Thus, minute particles of FeTi were found to be the most useful catalyst to improve the hydrogen adsorption properties of MgH₂. Nitrogen adsorption by the

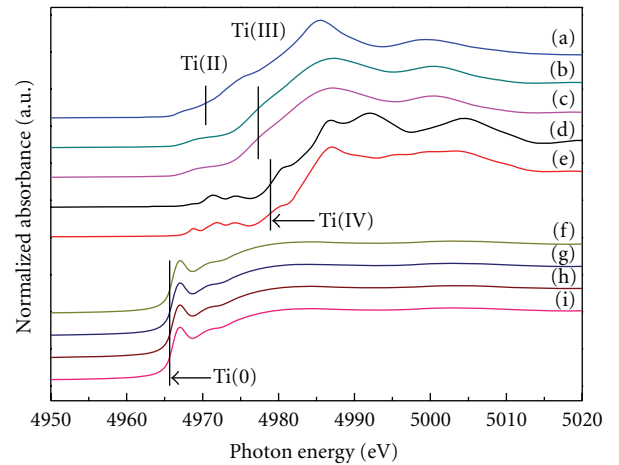


FIGURE 5: Ti K-edge XANES spectra of (a) TiO, (b) Ti₂O₃, (c) TiCl₃, (d) rutile-, (e) anatase-typed TiO₂ standards, (f) metallic Ti standard; (g) 20, (h) 12, and (i) 8 mol% Ti-NaAlH₄ metal hydride composites after the hydrogen adsorption processes.

CAs or Pd-doped CAs material clearly shows reversible type IV isotherms at each of the activation stages, indicative of permanent porosity in Figure 6(a). The selectivity of H₂ adsorption over Pd-doped CAs was 1.6 wt%, as shown in Figure 9(c). Due to the doping of Pd on CAs, access of hydrogen was easier in the vacancies created by the mesoporous structure with a higher surface area that was confirmed with the BET nitrogen isotherms measurement. In addition, this suggests that an antidispersive force plays an important role in case of Pd-doped CAs samples and the expected specific interaction with Pd active sites. Thus, this work confirmed that metal doping by Pd on CAs may improve the hydrogen adsorption criteria. An intriguing observation concerns the dependence of the rehydrogenation

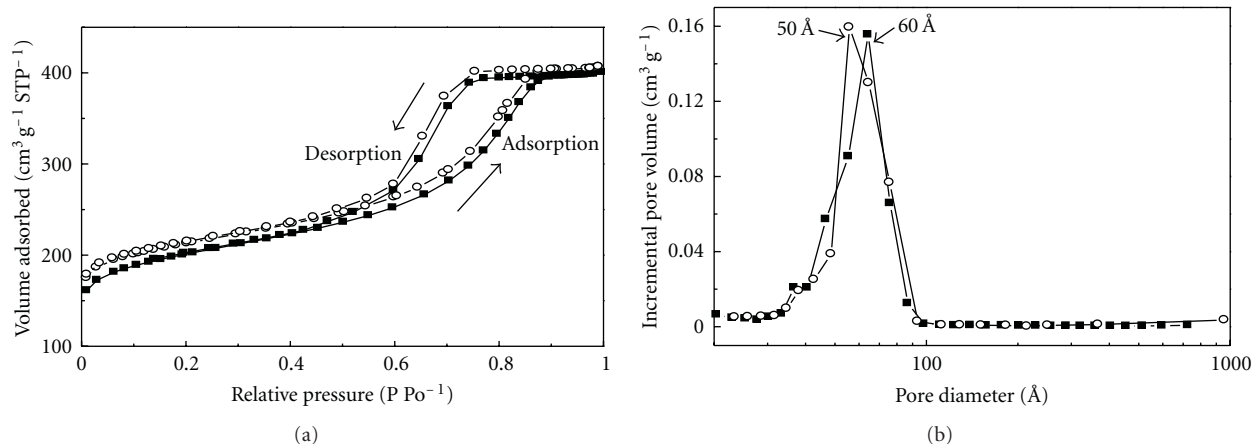


FIGURE 6: (a) Nitrogen adsorption/desorption isotherms and (b) pore size distribution for the as-synthesized (■) carbon aerogels, and (○) 5 wt% Pd-doped carbon aerogels. Arrow mark in the upward direction is the adsorption process and downward is the desorption process, respectively.

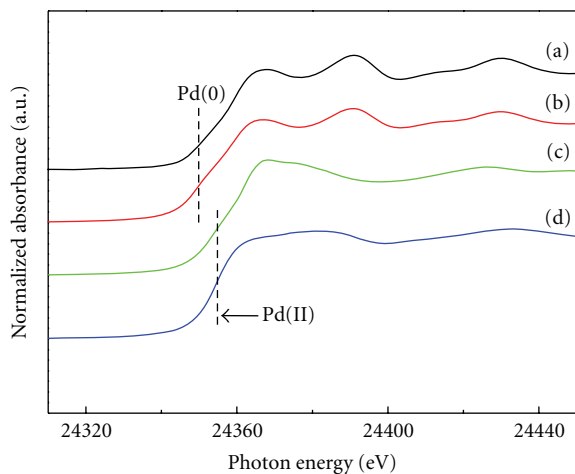


FIGURE 7: Pd K-edge XANES spectra of (a) 5 wt% Pd-CAS, (b) metallic Pd, (c) PdO, and (d) PdCl₂ standards.

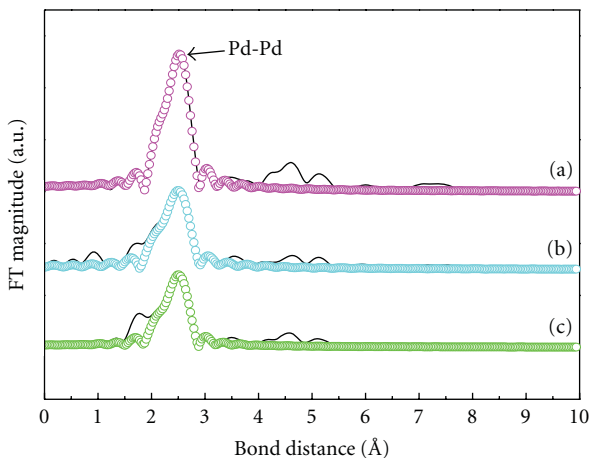


FIGURE 8: Fourier transformation (FT) spectra of (a) 5 wt% Pd-CAS, (b) metallic Pd, (c) PdO, and (d) PdCl₂ standards. The best fitting of the EXAFS spectra is expressed by the dotted lines.

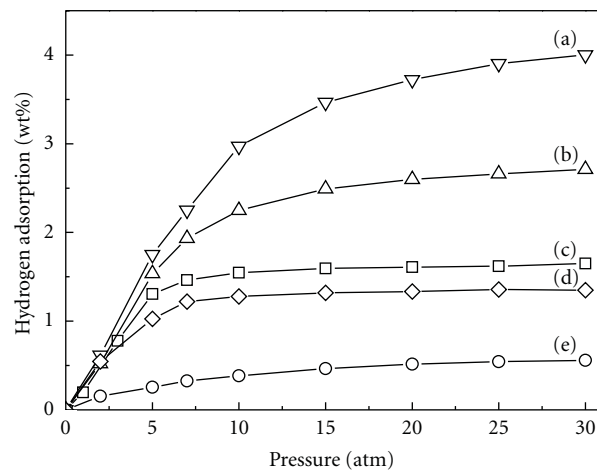


FIGURE 9: Hydrogen adsorption curves of (a) 5 wt% FeTi-CAS-MgH₂ (Fe:Ti = 2:1, molar ratio), (b) 5 wt% FeTi-MgH₂ (Fe:Ti = 2:1, molar ratio), (c) 5 wt% Pd-CAS, (d) 8 mol% Ti-NaAlH₄, and (e) fresh MgH₂. The pressures of hydrogen adsorption processes for as-synthesized metal hydride composites ranged from 1–30 atm.

kinetics on the amount of Ti doping. Moreover, as shown in Figure 9(a), it was observed that the hydrogen uptakes of FeTi-CAS-MgH₂ systems could be enhanced markedly by the phenomenon of “hydrogen spillover” via a simple technique for building carbon bridges [52]. One of the possible reasons is that the hydrogen molecules do not readily dissociate on Mg surface. Experimentally, the catalytic effect was found on hydrogen adsorption of mixing transition metal of Ti atoms into Mg hydride powder during ball-milling. The likely mechanism proposed for the FeTi-CAS-MgH₂ hetero-structures can be also summarized concisely: (1) adsorption of hydrogen on the Ti surface, (2) dissociation of hydrogen and chemisorption of atomic hydrogen on the surface, (3) migration of atomic hydrogen onto the CAS support, and finally (4) chemisorptive spillover onto the

MgH₂ substrate. In addition, spillover is facilitated through the use of a carbon bridging compound between the Ti/CAs complex and the MgH₂ substrate. Typically, an 8 mol% Ti-dop onto the NaAlH₄ (Figure 9(d)) revealed the maximum hydrogen adsorption capacity of 1.2 wt% within this class of adsorptive materials. In addition, perfect single crystal TiO₂ was inert toward reaction with H₂ [51]. However, H₂ was absorbed by TiO₂-surfaces that contained a higher density of defects in the crystal structure. Therefore, surface of MgH₂ in the presence of the metal-doped Fe and Ti with CAs created a high defect density that introduced a higher hydrogen adsorption behavior in the adsorption or desorption processes.

4. Conclusions

The synthesis, characterization, and H₂ adsorption capacity of CAs/metallic hydride nanocomposites as a catalyst were investigated in the present work. Experimentally, the H₂ storage capacity of metallic samples was conducted and measured by a TGA microbalance method. In addition, fine structures and crystallinity of metallic hydride were identified by BET nitrogen adsorption isotherms, HR-TEM, FE-SEM/EDS, XRD, and XANES/EXAFS. The CAs were very effective in improving the hydrogen storage capacity of the Fe-, Ti-doped MgH₂ samples with the “hydrogen spillover” route. Metallic dispersion such as Pd nanoparticles onto the CAs may improve the hydrogen adsorption abilities. Higher surface area from CAs and the defect criteria of the MgH₂ surface due to the doping of the metallic particle caused to improve the hydrogen adsorption capacities. On the other hand, Ti-doping onto the sodium aluminum hydride can only improve slightly the hydrogen storage capabilities.

Acknowledgment

The authors gratefully acknowledge the financial support of National Science Council (Contract no. NSC-95-2623-7-155-011) of Taiwan.

References

- [1] W. Lohstroh, M. Fichtner, and W. Breitung, “Complex hydrides as solid storage materials: first safety tests,” *International Journal of Hydrogen Energy*, vol. 34, no. 14, pp. 5981–5985, 2009.
- [2] J. Brouwer, “On the role of fuel cells and hydrogen in a more sustainable and renewable energy future,” *Current Applied Physics*, vol. 10, no. 2, pp. S9–S17, 2010.
- [3] M. Fichtner, O. Fuhr, O. Kircher, and J. Rothe, “Small Ti clusters for catalysis of hydrogen exchange in NaAlH₄,” *Nanotechnology*, vol. 14, no. 7, pp. 778–785, 2003.
- [4] F. S. Yang, G. X. Wang, Z. X. Zhang, X. Y. Meng, and V. Rudolph, “Design of the metal hydride reactors—a review on the key technical issues,” *International Journal of Hydrogen Energy*, vol. 35, no. 8, pp. 3832–3840, 2010.
- [5] E. Rönnebro, “High-pressure techniques for discovering and re-hydrogenation of metal hydride materials,” *Journal of Physics and Chemistry of Solids*, vol. 71, no. 8, pp. 1154–1158, 2010.
- [6] H. W. Brinks, C. M. Jensen, S. S. Srinivasan, B. C. Hauback, D. Blanchard, and K. Murphy, “Synchrotron X-ray and neutron diffraction studies of NaAlH₄ containing Ti additives,” *Journal of Alloys and Compounds*, vol. 376, no. 1-2, pp. 215–221, 2004.
- [7] D. J. Ross, M. D. Halls, A. G. Nazri, and R. F. Aroca, “Raman scattering of complex sodium aluminum hydride for hydrogen storage,” *Chemical Physics Letters*, vol. 388, no. 4-6, pp. 430–435, 2004.
- [8] R. A. Varin, T. Czujko, C. Chiu, R. Pulz, and Z. S. Wronski, “Synthesis of nanocomposite hydrides for solid-state hydrogen storage by controlled mechanical milling techniques,” *Journal of Alloys and Compounds*, vol. 483, no. 1-2, pp. 252–255, 2009.
- [9] P. Wang and C. M. Jensen, “Preparation of Ti-doped sodium aluminum hydride from mechanical milling of NaH/Al with off-the-shelf Ti powder,” *Journal of Physical Chemistry B*, vol. 108, no. 40, pp. 15827–15829, 2004.
- [10] E. Bruster, T. A. Dobbins, R. Tittsworth, and D. Anton, “Decomposition behavior of Ti-doped NaAlH₄ studied using X-ray absorption spectroscopy at the titanium K-edge,” in *Proceedings of the Materials Research Society Symposium*, pp. 47–52, December 2004.
- [11] O. Kircher and M. Fichtner, “Kinetic studies of the decomposition of NaAlH₄ doped with a Ti-based catalyst,” *Journal of Alloys and Compounds*, vol. 404-406, pp. 339–342, 2005.
- [12] I. P. Jain, P. Jain, and A. Jain, “Novel hydrogen storage materials: a review of lightweight complex hydrides,” *Journal of Alloys and Compounds*, vol. 503, no. 2, pp. 303–339, 2010.
- [13] R. Krishnan, D. Agrawal, and T. Dobbins, “Microwave irradiation effects on reversible hydrogen desorption in sodium aluminum hydrides (NaAlH₄),” *Journal of Alloys and Compounds*, vol. 470, no. 1-2, pp. 250–255, 2009.
- [14] X. Fan, X. Xiao, J. Hou et al., “Reversible hydrogen storage behaviors and microstructure of TiC-doped sodium aluminum hydride,” *Journal of Materials Science*, vol. 44, no. 17, pp. 4700–4704, 2009.
- [15] J. W. Kim, J. H. Shim, S. C. Kim et al., “Catalytic effect of titanium nitride nanopowder on hydrogen desorption properties of NaAlH₄ and its stability in NaAlH₄,” *Journal of Power Sources*, vol. 192, no. 2, pp. 582–587, 2009.
- [16] Z. Xueping, L. Shenglin, and L. Donglin, “The effect of additives on the hydrogen storage properties of NaAlH₄,” *International Journal of Hydrogen Energy*, vol. 34, no. 6, pp. 2701–2704, 2009.
- [17] P. Wang, X. D. Kang, and H. M. Cheng, “Exploration of the nature of active Ti species in metallic Ti-doped NaAlH₄,” *Journal of Physical Chemistry B*, vol. 109, no. 43, pp. 20131–20136, 2005.
- [18] S. Zhang, C. Lu, N. Takeichi, T. Kiyobayashi, and N. Kuriyama, “Reaction stoichiometry between TiCl₃ and NaAlH₄ in Ti-doped alanate for hydrogen storage: the fate of the titanium species,” *International Journal of Hydrogen Energy*, vol. 36, no. 1, pp. 634–638, 2011.
- [19] H. W. Brinks, B. C. Hauback, S. S. Srinivasan, and C. M. Jensen, “Synchrotron X-ray studies of Al_{1-y}Ti_y formation and re-hydrogenation in Ti-enhanced NaAlH₄,” *Journal of Physical Chemistry B*, vol. 109, no. 33, pp. 15780–15785, 2005.
- [20] E. H. Majzoub, J. L. Herberg, R. Stumpf, S. Spangler, and R. S. Maxwell, “XRD and NMR investigation of Ti-compound formation in solution-doping of sodium aluminum hydrides: solubility of Ti in NaAlH₄ crystals grown in THF,” *Journal of Alloys and Compounds*, vol. 394, no. 1-2, pp. 265–270, 2005.
- [21] T. Schmidt and L. Röntzsch, “Reversible hydrogen storage in Ti-Zr-codoped NaAlH₄ under realistic operation conditions,” *Journal of Alloys and Compounds*, vol. 496, no. 1-2, pp. L38–L40, 2010.

- [22] M. Onkawa, S. Zhang, H. T. Takeshita, N. Kuriyama, and T. Kiyobayashi, "Dehydrogenation kinetics of Ti-doped NaAlH_4 —influence of Ti precursors and preparation methods," *International Journal of Hydrogen Energy*, vol. 33, no. 2, pp. 718–721, 2008.
- [23] X. Xiao, L. Chen, X. Wang, Q. Wang, and C. Chen, "The hydrogen storage properties and microstructure of Ti-doped sodium aluminum hydride prepared by ball-milling," *International Journal of Hydrogen Energy*, vol. 32, no. 13, pp. 2475–2479, 2007.
- [24] C. Milanese, A. Girella, G. Bruni et al., "Hydrogen storage in magnesium-metal mixtures: reversibility, kinetic aspects and phase analysis," *Journal of Alloys and Compounds*, vol. 465, no. 1-2, pp. 396–405, 2008.
- [25] M. Danaie, S. X. Tao, P. Kalisvaart, and D. Mitlin, "Analysis of deformation twins and the partially dehydrogenated microstructure in nanocrystalline magnesium hydride (MgH_2) powder," *Acta Materialia*, vol. 58, no. 8, pp. 3162–3172, 2010.
- [26] R. Domènech-Ferrer, M. Gurusamy Sridharan, G. Garcia, F. Pi, and J. Rodríguez-Viejo, "Hydrogenation properties of pure magnesium and magnesium-aluminium thin films," *Journal of Power Sources*, vol. 169, no. 1, pp. 117–122, 2007.
- [27] K. J. Jeon, A. Theodore, and C. Y. Wu, "Enhanced hydrogen absorption kinetics for hydrogen storage using Mg flakes as compared to conventional spherical powders," *Journal of Power Sources*, vol. 183, no. 2, pp. 693–700, 2008.
- [28] S. G. Chalk and J. F. Miller, "Key challenges and recent progress in batteries, fuel cells, and hydrogen storage for clean energy systems," *Journal of Power Sources*, vol. 159, no. 1, pp. 73–80, 2006.
- [29] I. E. Malka, T. Czujko, and J. Bystrzycki, "Catalytic effect of halide additives ball milled with magnesium hydride," *International Journal of Hydrogen Energy*, vol. 35, no. 4, pp. 1706–1712, 2010.
- [30] B. Sakintuna, F. Lamari-Darkrim, and M. Hirscher, "Metal hydride materials for solid hydrogen storage: a review," *International Journal of Hydrogen Energy*, vol. 32, no. 9, pp. 1121–1140, 2007.
- [31] J. Wang, A. D. Ebner, R. Zidan, and J. A. Ritter, "Synergistic effects of co-dopants on the dehydrogenation kinetics of sodium aluminum hydride," *Journal of Alloys and Compounds*, vol. 391, no. 1-2, pp. 245–255, 2005.
- [32] S. Chaudhuri and J. T. Muckerman, "First-principles study of Ti-catalyzed hydrogen chemisorption on an Al surface: a critical first step for reversible hydrogen storage in NaAlH_4 ," *Journal of Physical Chemistry B*, vol. 109, no. 15, pp. 6952–6957, 2005.
- [33] E. H. Majzoub, J. L. Herberg, R. Stumpf, S. Spangler, and R. S. Maxwell, "XRD and NMR investigation of Ti-compound formation in solution-doping of sodium aluminum hydrides: solubility of Ti in NaAlH_4 crystals grown in THF," *Journal of Alloys and Compounds*, vol. 394, no. 1-2, pp. 265–270, 2005.
- [34] H. Imamura, Y. Takesue, S. Tabata, N. Shigetomi, Y. Sakata, and S. Tsuchiya, "Hydrogen storage composites obtained by mechanical grinding of magnesium with graphite carbon," *Chemical Communications*, no. 22, pp. 2277–2278, 1999.
- [35] S. Carter, A. S. Fisher, P. S. Goodall, M. W. Hinds, S. Lancaster, and S. Shore, "Atomic spectrometry update. Industrial analysis: metals, chemicals and advanced materials," *Journal of Analytical Atomic Spectrometry*, vol. 25, no. 12, pp. 1808–1858, 2010.
- [36] A. Léon, O. Kircher, M. Fichtner, J. Rothe, and D. Schild, "Evolution of the local structure around Ti atoms in NaAlH_4 doped with TiCl_3 or $\text{Ti}_{13}\cdot 6\text{THF}$ by ball milling using X-ray absorption and X-ray photoelectron spectroscopy," *Journal of Physical Chemistry B*, vol. 110, no. 3, pp. 1192–1200, 2006.
- [37] P. Canton, M. Fichtner, C. Frommen, and A. Léon, "Synchrotron X-ray studies of Ti-doped NaAlH_4 ," *Journal of Physical Chemistry B*, vol. 110, no. 7, pp. 3051–3054, 2006.
- [38] A. Léon, A. Balerna, G. Cinque, C. Frommen, and M. Fichtner, "Al K edge XANES measurements in NaAlH_4 doped with TiCl_3 by ball milling," *Journal of Physical Chemistry C*, vol. 111, no. 9, pp. 3795–3798, 2007.
- [39] F. W. Lytle, "The EXAFS family tree: a personal history of the development of extended X-ray absorption fine structure," *Journal of Synchrotron Radiation*, vol. 6, no. 3, pp. 123–134, 1999.
- [40] S. D. Conradson, "Application of X-ray absorption fine structure spectroscopy to materials and environmental science," *Applied Spectroscopy*, vol. 52, no. 7, pp. 252A–279A, 1998.
- [41] G. Vlaic, D. Andreatta, and P. E. Colavita, "Characterisation of heterogeneous catalysts by EXAFS," *Catalysis Today*, vol. 41, no. 1-3, pp. 261–275, 1998.
- [42] R. W. Pekala, "Organic aerogels from the polycondensation of resorcinol with formaldehyde," *Journal of Materials Science*, vol. 24, no. 9, pp. 3221–3227, 1989.
- [43] X. Yao, C. Wu, A. Du et al., "Mg-based nanocomposites with high capacity and fast kinetics for hydrogen storage," *Journal of Physical Chemistry B*, vol. 110, no. 24, pp. 11697–11703, 2006.
- [44] M. Eddaoudi, H. Li, and O. M. Yaghi, "Highly porous and stable metal-organic frameworks: structure design and sorption properties," *Journal of the American Chemical Society*, vol. 122, no. 7, pp. 1391–1397, 2000.
- [45] C. P. Baldé, A. M. J. van der Eerden, H. A. Stil, F. M. F. de Groot, K. P. de Jong, and J. H. Bitter, "On the local structure of Ti during in situ desorption of $\text{Ti}(\text{O}i\text{Bu})_4$ and TiCl_3 doped NaAlH_4 ," *Journal of Alloys and Compounds*, vol. 446–447, pp. 232–236, 2007.
- [46] J. Wang, A. D. Ebner, T. Prozorov, R. Zidan, and J. A. Ritter, "Effect of graphite as a co-dopant on the dehydrogenation and hydrogenation kinetics of Ti-doped sodium aluminum hydride," *Journal of Alloys and Compounds*, vol. 395, no. 1-2, pp. 252–262, 2005.
- [47] T. Vegge, "Equilibrium structure and Ti-catalyzed H_2 desorption in NaAlH_4 nanoparticles from density functional theory," *Physical Chemistry Chemical Physics*, vol. 8, no. 42, pp. 4853–4861, 2006.
- [48] Y. Yamamoto, T. Matsuzaki, K. Ohdan, and Y. Okamoto, "Structure and electronic state of $\text{PdCl}_2\text{-CuCl}_2$ catalysts supported on activated carbon," *Journal of Catalysis*, vol. 161, no. 2, pp. 577–586, 1996.
- [49] S. Cacchi, C. L. Cotet, G. Fabrizi et al., "Efficient hydroxycarbonylation of aryl iodides using recoverable and reusable carbon aerogels doped with palladium nanoparticles as catalyst," *Tetrahedron*, vol. 63, no. 11, pp. 2519–2523, 2007.
- [50] L. C. Cotet, M. Gich, A. Roig et al., "Synthesis and structural characteristics of carbon aerogels with a high content of Fe, Co, Ni, Cu, and Pd," *Journal of Non-Crystalline Solids*, vol. 352, no. 26-27, pp. 2772–2777, 2006.
- [51] K. S. Jung, E. Y. Lee, and K. S. Lee, "Catalytic effects of metal oxide on hydrogen absorption of magnesium metal hydride," *Journal of Alloys and Compounds*, vol. 421, no. 1-2, pp. 179–184, 2006.
- [52] C.-S. Tsao, M.-S. Yu, C.-Y. Wang et al., "Nanostructure and hydrogen spillover of bridged metal-organic frameworks," *Journal of the American Chemical Society*, vol. 131, no. 4, pp. 1404–1406, 2009.

Research Article

Consolidation of Amorphous $\text{Al}_{80}\text{Fe}_{10}\text{Ti}_5\text{Ni}_5$ Powders by Hot Pressing

M. Tavoosi,^{1,2} F. Karimzadeh,¹ M. H. Enayati,¹ and H. S. Kim²

¹Department of Material Engineering, Nanotechnology and Advanced Material Institute, Isfahan University of Technology (IUT), Isfahan 84156-83111, Iran

²Department of Materials Science and Engineering, Pohang University of Science and Technology (POSTECH), Pohang 790-784, Republic of Korea

Correspondence should be addressed to H. S. Kim, hskim@postech.ac.kr

Received 13 May 2012; Accepted 8 July 2012

Academic Editor: Mohammad H. Maneshian

Copyright © 2012 M. Tavoosi et al. This is an open access article distributed under the Creative Commons Attribution License, which permits unrestricted use, distribution, and reproduction in any medium, provided the original work is properly cited.

The current study investigates the feasibility of fabricating amorphous $\text{Al}_{80}\text{Fe}_{10}\text{Ti}_5\text{Ni}_5$ powders by mechanical alloying and consolidating them into bulk samples by a hot-pressing technique. As-milled and hot-pressed samples were examined by X-ray diffraction, scanning electron microscopy, transition electron microscopy, and differential scanning calorimetry. The results showed that milling of $\text{Al}_{80}\text{Fe}_{10}\text{Ti}_5\text{Ni}_5$ powder for 40 h and hot pressing at 550°C under 600 MPa led to a fully dense bulk sample. During consolidation, an AlTi intermetallic phase with average crystallite size of 10 nm precipitates in the amorphous matrix.

1. Introduction

Alloys with Al content of 80 to 90 at.% have attracted considerable attention due to their combination of good ductility and high strength [1–7]. Among the various aluminum alloys, Al-Fe systems are of technological interest due to their advantageous properties, including high specific strength, high specific stiffness, good strength at intermediate temperatures, and excellent corrosion resistance at elevated temperatures under oxidizing, carburizing, and sulfidizing atmospheres [8–12]. A new class of Al-based alloys, which has received a great deal of attention in recent years, is amorphous as well as nanocrystalline [13–23].

Indeed, amorphous alloys exhibit several superior properties that cannot be obtained in crystalline materials. In general, bulk amorphous alloys can be fabricated by two main processes: direct solidification from the melt and consolidation of an amorphous powder or ribbons. Generally, very high cooling rates are required for the formation of an amorphous phase from the liquid state and only a few amorphous alloys with high glass-forming ability can be applied to the fabrication of bulk amorphous alloys by a direct solidification process. Due to the requirement of a

high cooling rate, amorphous alloys have largely been fabricated in the form of powders, ribbons, and wires with small thickness or diameter [14–17], and hence the application of amorphous alloys as a structural material has been limited.

The glass-forming ability of Al-based alloys is so low and there is not any report about formation of bulk amorphous structure for these alloys by the use of direct solidification methods [11–13]. Nevertheless, a great number of amorphous alloys in Al-based alloys have been synthesized by various preparation methods of rapid quenching from liquid or vapor and solid-state reactions [13]. However, the maximum thicknesses of the resulting amorphous alloys have usually been limited. The limitation of the maximum sample thickness has prevented a wide extension of application fields of amorphous alloys. Consequently, great efforts have been devoted to preparation of a bulk amorphous alloy from amorphous alloy powder by using various techniques of warm pressing, warm extrusion, explosive compaction, hot pressing, and spark plasma sintering [13, 24]. The powder metallurgy process promotes high strength bonding between particles and a microstructure similar to that of a wrought product [25–30].

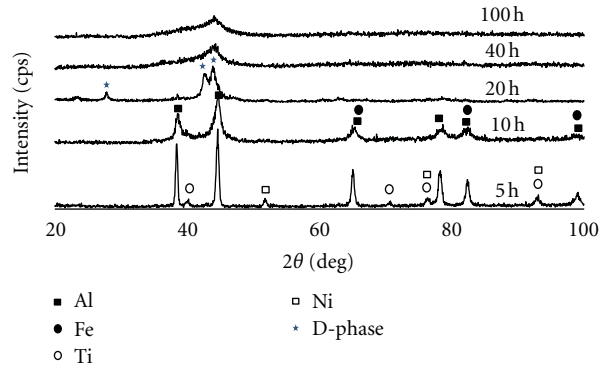


FIGURE 1: XRD patterns of the Al-10%Fe-5%Ni-5%Ti powder mixture after various milling times.

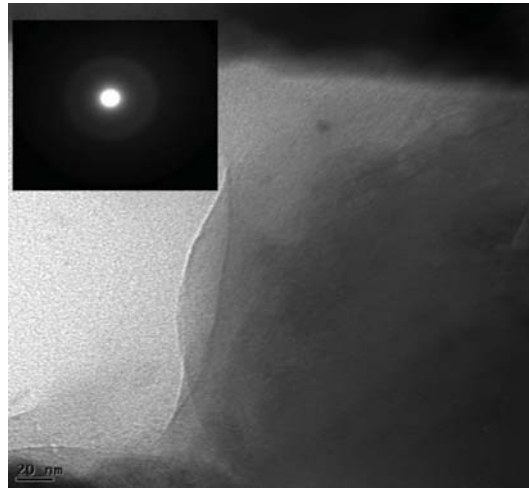


FIGURE 2: TEM image of the Al-10%Fe-5%Ti-5%Ni powder mixture after 40 h of MA.

The purpose of this study is the investigation of the feasibility of fabricating amorphous $\text{Al}_{80}\text{Fe}_{10}\text{Ti}_5\text{Ni}_5$ powders by mechanical alloying and consolidating them into bulk samples by a hot-pressing technique.

2. Experimental Procedure

Commercial elemental powders of Al (99%), Fe (99.9%), Ti (99%), and Ni (99.99%) were used as raw materials. The mixture of elemental powders with a composition of $\text{Al}_{80}\text{Fe}_{10}\text{Ti}_5\text{Ni}_5$ (in atomic percentage) was mechanically alloyed in a planetary ball mill under an argon atmosphere in a steel container at room temperature. A rotation speed of 250 rpm and a ball to powder ratio of 10 : 1 were employed. 1 wt% stearic acid powder supplied by Merck was used as the process control agent (PCA).

The produced amorphous powders were consolidated in a vacuum hot-pressing machine to prepare bulk amorphous discs with 10 mm diameter and 1 mm thickness. Hot pressing was performed at different temperatures and pressures. The hot-pressing chamber was evacuated and pressure was applied during the entire consolidating process.

The as-milled powders and consolidated samples were characterized by X-ray diffraction (XRD) analysis, scanning

electron microscopy (SEM), transition electron microscopy (TEM), and differential scanning calorimetry. The XRD analysis was performed using a Philips diffractometer (40 kV) with Cu $K\alpha$ radiation ($\lambda = 0.15406$ nm). The XRD patterns were recorded in the 2θ range of $30\text{--}70^\circ$ (step size 0.03° and time per step 1 s). The morphology, fracture surface, and cross-sections of prepared samples were examined using SEM. The microstructure of the produced amorphous powder was investigated by TEM and a selected area diffraction (SAD) pattern analysis carried out at an accelerating voltage of 200 kV resolution of 0.19 nm. A differential thermal analysis (DTA) was conducted to study the thermal stability of the produced amorphous alloy using a Reometric STA 1500 differential thermal analyzer. The samples were placed in Al_2O_3 pans and heated in a dynamic Ar atmosphere up to 1200°C at a constant heating rate of $40^\circ\text{C}/\text{min}$.

3. Results and Discussion

3.1. Production of $\text{Al}_{80}\text{Fe}_{10}\text{Ti}_5\text{Ni}_5$ Amorphous Phase. The XRD patterns of the Al-10%Fe-5%Ni-5%Ti powder mixture after various milling times are shown in Figure 1. In the early stage of milling, broadening of Al, Fe, Ni, and Ti peaks

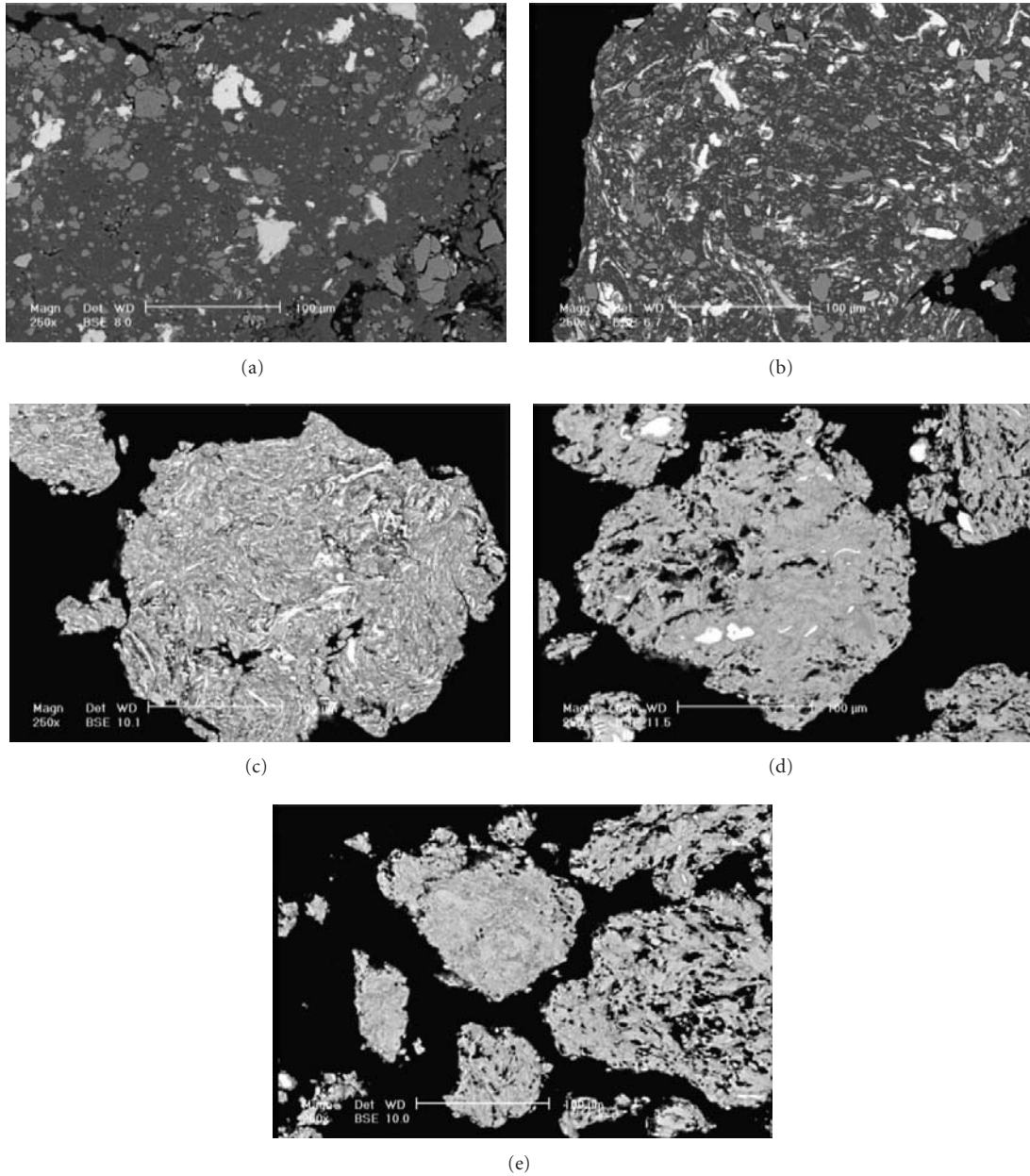


FIGURE 3: SEM cross-sectional micrographs of Al-10%Fe-5%Ti-5%Ni powder mixture after different milling times: (a) 0.25 h, (b) 0.5 h, (c) 1 h, (d) 5 h, and (e) 10 h.

accompanied by a remarkable decrease in their intensities occurred as a result of refinement of crystallite size and enhancement of lattice strain. Increasing milling time up to 10 h led to the disappearance of Fe, Ti, and Ni peaks. This may be due to dissolution of these elements in the Al lattice. By increasing the milling time, two narrow peaks corresponding to the decagonal phase (D-phase) are observed in the XRD patterns. Analysis of the XRD patterns in Figure 1 reveals that the D-phase, which formed from the solid solution during milling, could be amorphized by further milling (after 40 h) and there is no significant change as the milling time is prolonged to 100 h. A TEM micrograph

and SAD pattern of powders ball milled for 40 h are also presented in Figure 2. As can be seen in this figure, the SAD pattern of this sample consists of only amorphous halo and there is no evidence of the presence of any crystalline phase, which is in agreement with the XRD result. This indicates that the product of mechanical alloying of the Al-10%Fe-5%Ni-5%Ti powder mixture is an amorphous phase.

SEM cross-sectional micrographs of powder particles after different milling times are presented in Figure 3. According to the micrographs, in the early stages of mechanical alloying (MA), the ductile components are flattened to platelet shapes, cold welded together, and form a composite

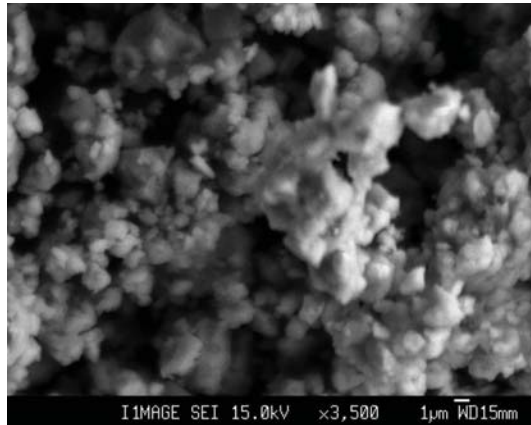


FIGURE 4: Morphology of Al-10%Fe-5%Ti-5%Ni powder mixture after 40 h of ball milling.

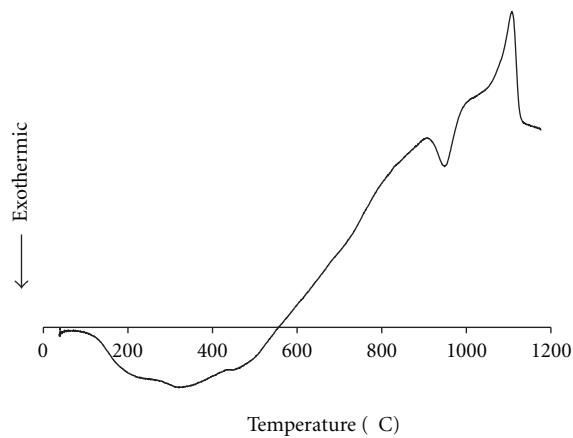


FIGURE 5: DSC curves of amorphous $\text{Al}_{80}\text{Fe}_{10}\text{Ti}_5\text{Ni}_5$ alloy at a constant heating rate of $40^\circ\text{C}/\text{min}$.

lamellar structure of the constituent metals (Figures 3(a) and 3(b)). With increasing MA time, the composite powder particles are work hardened and fragmented. With further milling (Figures 3(c) and 3(d)), the interlamellar spacing decreases and true alloying at the atomic level occurs, resulting in the formation of solid solutions, intermetallics, or even amorphous phases. In this stage, the interlayer spacing disappears or becomes so fine that it is no longer visible using SEM (Figure 3(e)). The morphology of $\text{Al}_{80}\text{Fe}_{10}\text{Ti}_5\text{Ni}_5$ powders after 40 h of ball milling is also shown in Figure 4. As seen here, the powders milled for 40 h are spherical and have an average diameter of $2\ \mu\text{m}$.

3.2. Thermal Behavior of Produced Amorphous Powder. As noted in the previous section, milling the mixed powder for 40 h led to the formation of the $\text{Al}_{80}\text{Fe}_{10}\text{Ti}_5\text{Ni}_5$ amorphous phase. The mechanically milled microstructure is in a metastable state and considerable microstructural changes can occur upon heating the milled powder. In order to

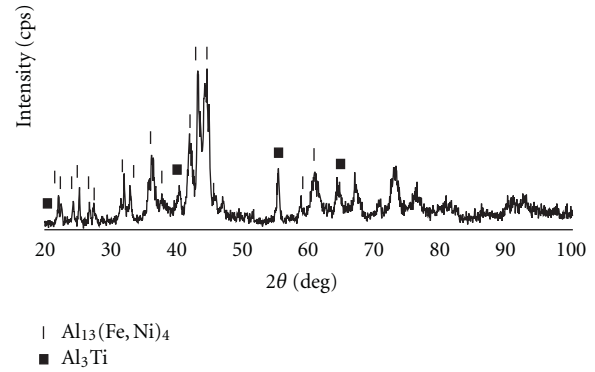


FIGURE 6: XRD pattern of amorphous $\text{Al}_{80}\text{Fe}_{10}\text{Ti}_5\text{Ni}_5$ alloy after isothermal annealing at 1000°C for 20 min.

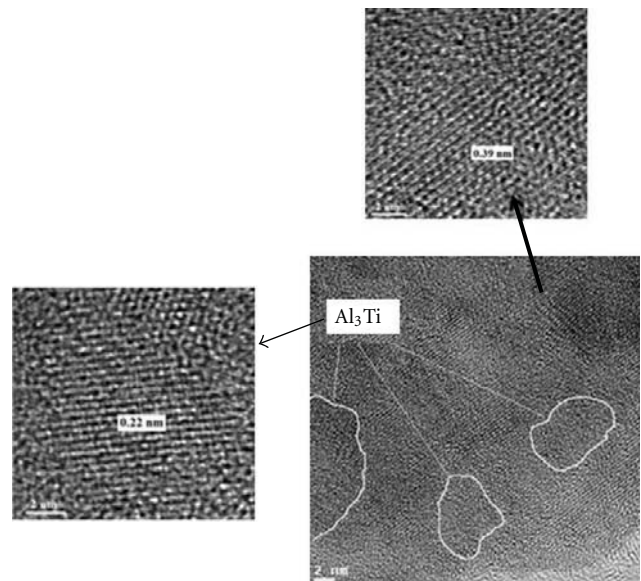


FIGURE 7: HRTEM image of amorphous $\text{Al}_{80}\text{Fe}_{10}\text{Ti}_5\text{Ni}_5$ alloy after isothermal annealing at 1000°C for 20 min.

study the thermal stability of the produced amorphous phase, the sample was examined by DSC under continuous heating conditions. Figure 5 shows the DSC heating traces of the $\text{Al}_{80}\text{Fe}_{10}\text{Ti}_5\text{Ni}_5$ amorphous alloy at a constant heating rate of $20^\circ\text{C}/\text{min}$. As seen in this figure, two peaks appear in the DSC curve (an exothermic peak at 950°C and an endothermic peak at 1100°C). To analyze the crystallization process responsible for the exothermic peak, the as-blended sample was annealed under an Ar atmosphere at 1000°C for 20 min. The XRD pattern and a TEM micrograph of the $\text{Al}_{80}\text{Fe}_{10}\text{Ti}_5\text{Ni}_5$ amorphous phase after annealing at 1000°C are presented in Figures 6 and 7, respectively. As can be seen here, the annealed sample consists mainly of an $\text{Al}_{13}(\text{Fe},\text{Ni})_4$ [31] and Al_3Ti [32] intermetallic phases. Therefore, the exothermic peak in Figure 5 is attributed to precipitation of these phases from the amorphous phase. Meanwhile,

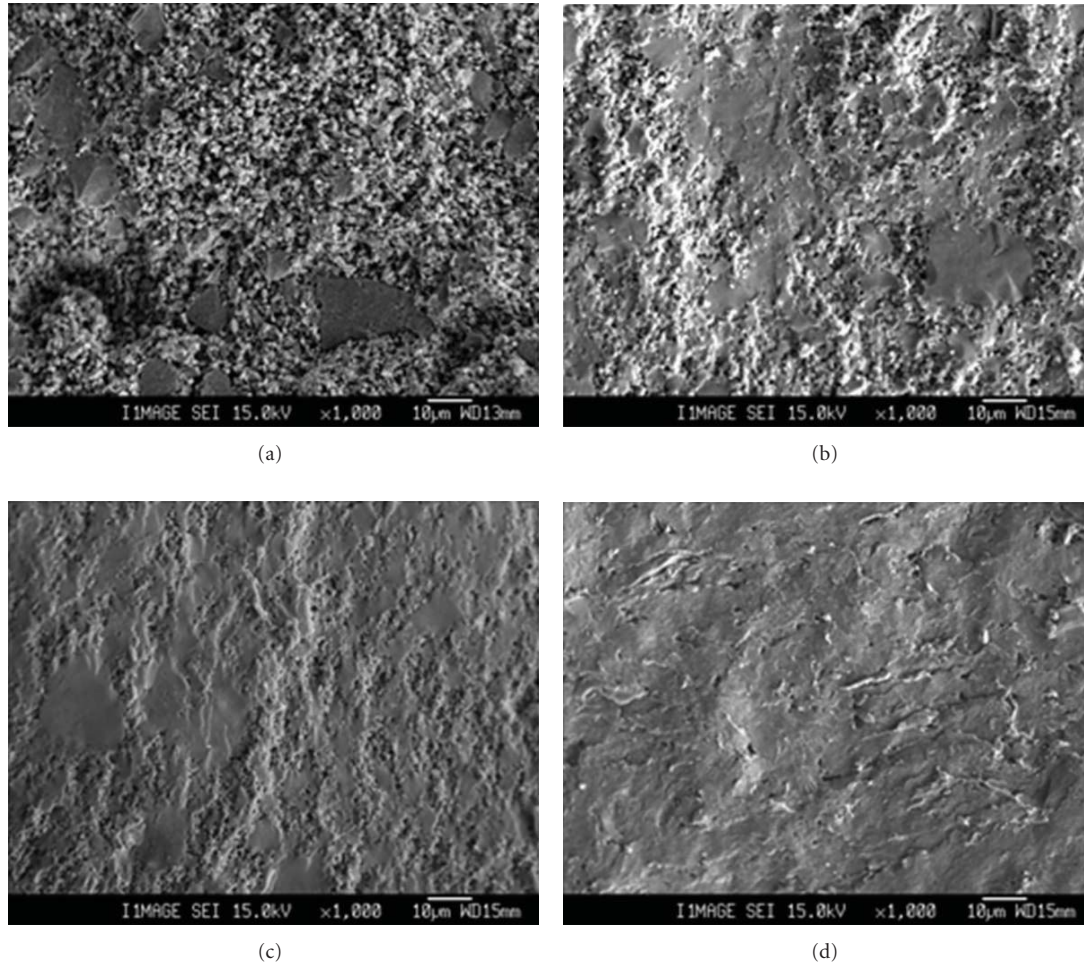


FIGURE 8: Fracture surface photographs of samples hot pressed at (a) 400°C, (b) 450°C, (c) 500°C, and (d) 550°C under a constant pressure 600 MPa.

the endothermic peak at 1100°C in Figure 5 is for the melting of the produced alloy. These results indicate that the total transformation sequence of the $\text{Al}_{80}\text{Fe}_{10}\text{Ti}_5\text{Ni}_5$ amorphous alloy is a one-stage process in the temperature range from 930°C to 980°C.

In fact, according to the DSC results, the crystallization in $\text{Al}_{80}\text{Fe}_{10}\text{Ti}_5\text{Ni}_5$ proceeds in the same manner as in the $\text{Al}_{80}\text{Fe}_{10}\text{Ti}_{10}$ [11] system and is different from that in $\text{Al}_{80}\text{Fe}_{20}$ [23] and $\text{Al}_{83}\text{Fe}_{17}$ [10] amorphous systems. In contrast to the $\text{Al}_{80}\text{Fe}_{10}\text{Ti}_5\text{Ni}_5$ amorphous alloy (which exhibits one-stage crystallization on heating), the $\text{Al}_{80}\text{Fe}_{20}$ and $\text{Al}_{83}\text{Fe}_{17}$ amorphous phases exhibit three-stage crystallization during heating.

3.3. Consolidation of the Ball-Milled Amorphous Powders.

Fully amorphous powder particles with high crystallization temperature (950°C) in $\text{Al}_{80}\text{Fe}_{10}\text{Ti}_5\text{Ni}_5$ alloy provide good conditions for the fabrication of a bulk amorphous material. In this study, the as-milled powders were consolidated by hot pressing into a disk shape. To optimize the condensation parameter, the ball-milled amorphous powders were hot

pressed at different temperatures (400, 450, 500, and 550°C) under various pressures (200, 300, 400, 500, and 600 MPa) for 30 min. In order to investigate the condensed samples, the fracture surface morphology after compression tests was examined using SEM. Fracture surface photographs of samples hot pressed at different temperatures under a constant pressure of 600 MPa and under different pressure values at a constant temperature of 550°C are shown in Figures 8 and 9, respectively. As seen in these figures, the trace of the interparticle boundaries between the powders increases and the porosity in the hot pressed samples decreases as the pressing temperature and pressure increase. These results indicate that the optimum temperature and pressure for consolidation of the amorphous powders via the hot-pressing method are 550°C and 600 MPa, respectively, in our experimental conditions. The polished cross-sectional view of the consolidated sample at 550°C under 600 MPa in Figure 10 shows no remaining pores.

Figure 11 shows the XRD pattern of the consolidated at 550°C under 600 MPa. From the peaks corresponding to AlTi, it can be concluded that the amorphous phase

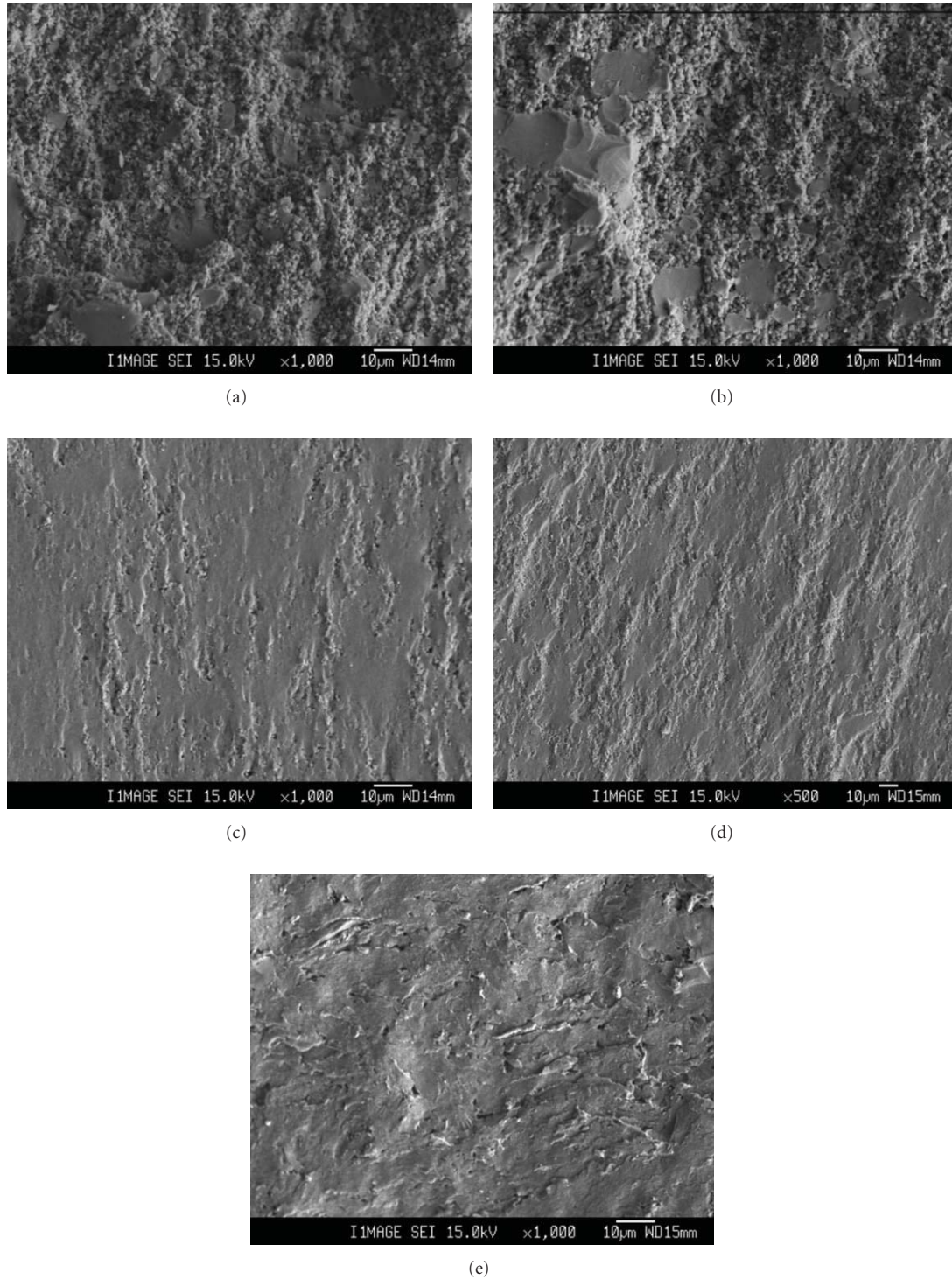


FIGURE 9: Fracture surface photographs of samples hot pressed under (a) 200 MPa, (b) 300 MPa, (c) 400 MPa, (d) 500 MPa, and (e) 600 MPa pressure at a constant temperature 550°C.

does not remain after consolidation at temperature of 550°C for 30 min. The presence of the crystalline phase in the amorphous matrix in the consolidated bulk sample can be further confirmed by TEM and elemental maps. The

TEM micrograph and elemental map of the hot-pressed sample are shown in Figures 12 and 13, respectively, where limited nanocrystallization (formation of AlTi with average size of 10 nm in the amorphous matrix) occurred during

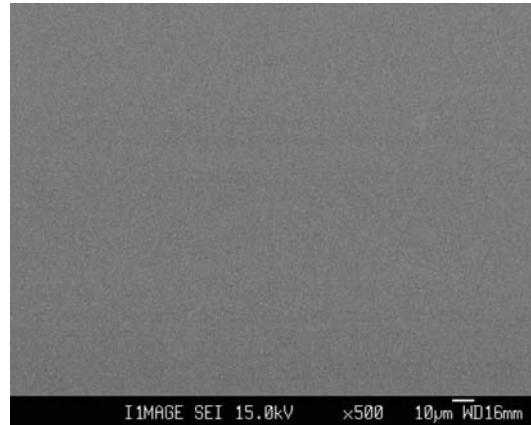


FIGURE 10: Polished cross-sectional view of sample hot pressed at 550°C under 600 MPa.

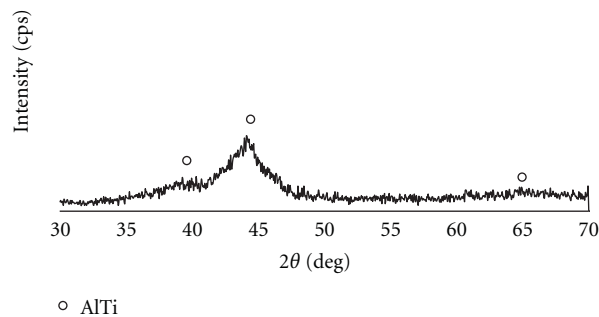


FIGURE 11: XRD pattern of sample hot pressed at 550°C under 600 MPa.

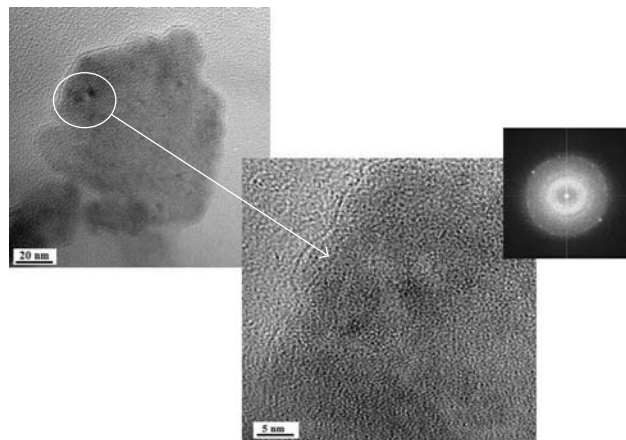


FIGURE 12: TEM image of sample hot pressed at 550°C under 600 MPa.

the consolidation processes and the produced bulk material is not fully amorphous.

3.4. Thermal Behavior of Produced Bulk Material. In order to investigate the thermal behavior and microstructural changes of the consolidated bulk amorphous alloy (below crystallization temperature), pressed samples were annealed at several temperatures for 3 h. XRD patterns of as-hot

pressed and annealed samples at 550°C, 600°C, 650°C, and 700°C are presented in Figure 14. During the consolidation of the amorphous powders at 550°C for 30 min, the AlTi phase precipitates in the amorphous matrix. Analysis of the XRD patterns in Figure 14 reveals that by annealing the samples at temperature above 550°C (below crystallization temperature), the AlTi diffraction peaks disappeared and several peaks corresponding to $\text{Al}_{13}(\text{Fe,Ni})_4$ and Al_3Ti intermetallic

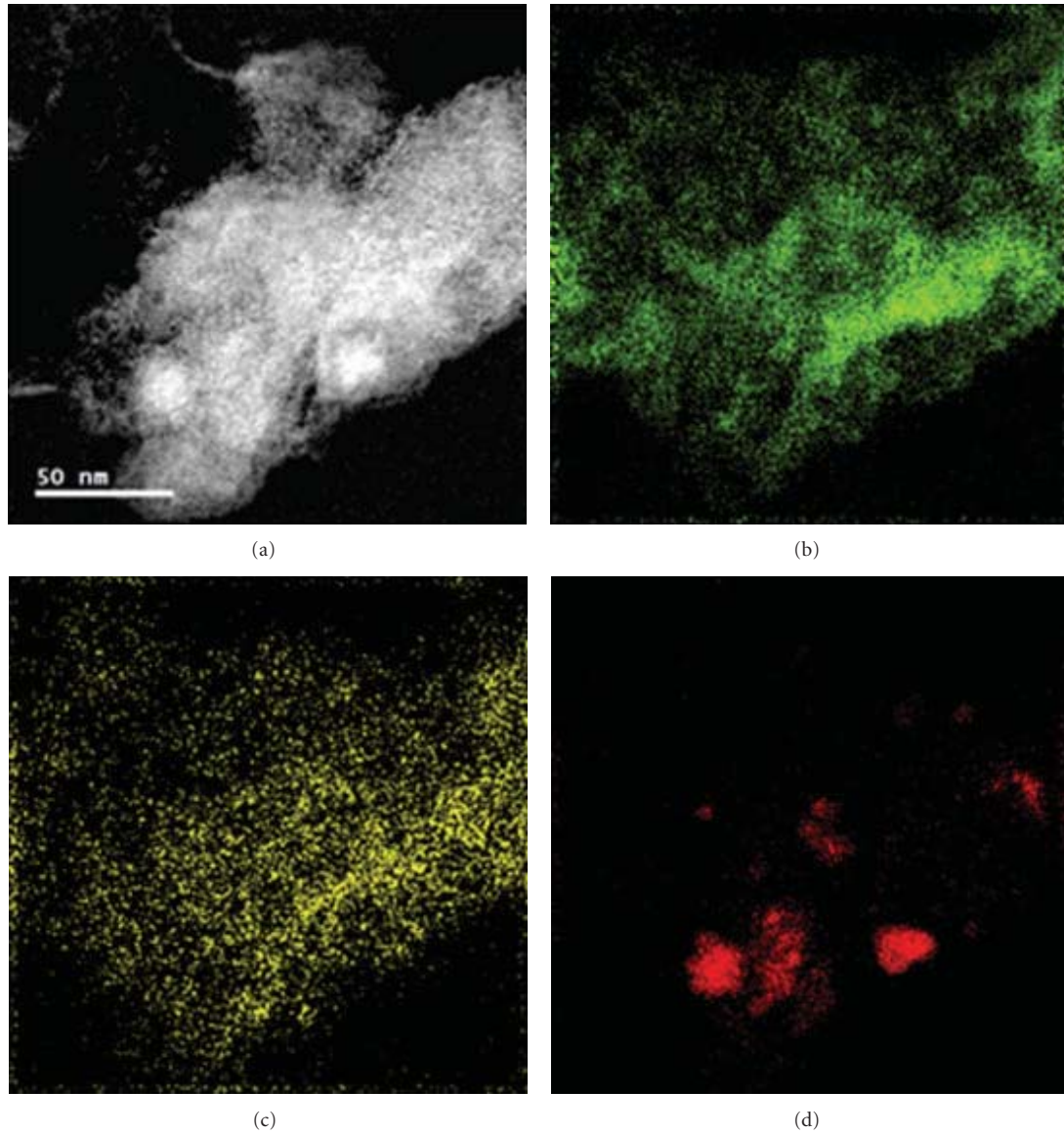


FIGURE 13: (a) Al, (b) Ni, (c) Fe, and (d) Ti elemental maps of the sample hot pressed at 550°C under 600 MPa.

phases appeared. By increasing the annealing temperature, the intensity of $\text{Al}_{13}(\text{Fe,Ni})_4$ and Al_3Ti peaks in the XRD patterns increases as a result of increasing the crystalline size and the fraction of this phase during annealing.

4. Conclusions

In the present work, we fabricated amorphous $\text{Al}_{80}\text{Fe}_{10}\text{Ti}_5\text{Ni}_5$ powders by milling elemental powder mixtures for 40 h. The crystallization process of this amorphous alloy is a one-stage mode of the $\text{Al}_{13}(\text{Fe,Ti})_4$ and Al_3Ti intermetallic compounds. The results showed that the as-milled amorphous $\text{Al}_{80}\text{Fe}_{10}\text{Ti}_5\text{Ni}_5$ powders were consolidated successfully into bulk metallic glasses by a hot pressing technique. The temperature and pressure for successful condensation of amorphous powders in the hot

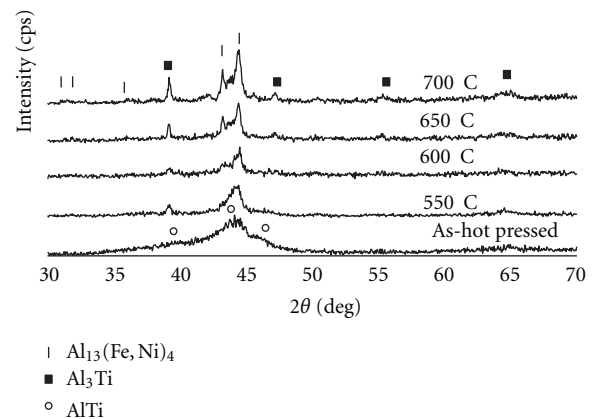


FIGURE 14: XRD patterns of samples as-hot pressed and annealed at 550°C, 600°C, 650°C, and 700°C for 3 h.

pressing method are 550°C and 600 MPa, respectively. During the consolidation, the amorphous phase does not remain and an AlTi intermetallic phase precipitates in the amorphous matrix.

Acknowledgments

This work was supported by the National Research Foundation of Korea (NRF) grant funded by the Korea government (MEST, no. 2010-0026981). H. S. Kim acknowledges the support of a grant (B551179-08-01-00) from the cooperative research project “Development of common manufacturing technology for high functional susceptor” funded by the Ministry of Knowledge Economy, Republic of Korea.

References

- [1] H. S. Kim, P. J. Warren, B. Cantor, and H. R. Lee, “Mechanical properties of partially crystallized aluminum based amorphous alloys,” *Nanostructured Materials*, vol. 11, no. 2, pp. 241–247, 1999.
- [2] H. S. Kim and S. I. Hong, “A model of the ductile-brittle transition of partially crystallized amorphous Al-Ni-Y alloys,” *Acta Materialia*, vol. 47, no. 7, pp. 2059–2066, 1999.
- [3] H. S. Kim, “Yield and compaction behavior of rapidly solidified Al-Si alloy powders,” *Materials Science and Engineering A*, vol. 251, no. 1-2, pp. 100–105, 1998.
- [4] H. Asgharzadeh, A. Simchi, and H. S. Kim, “Hot deformation of ultrafine-grained Al6063/Al₂O₃ nanocomposites,” *Journal of Materials Science*, vol. 46, no. 14, pp. 4994–5001, 2011.
- [5] S.-H. Lee and C.-S. Kang, “Fabrication and estimation of an ultrafine grained complex aluminum alloy sheet by the ARB process using dissimilar aluminum alloys,” *Journal of Korean Institute of Metals and Materials*, vol. 49, no. 11, pp. 893–899, 2011.
- [6] W.-D. Kang and H. G. Park, “Influence of Zr addition on TiB₂ modification and grain size in aluminium alloys,” *Journal of Korean Institute of Metals and Materials*, vol. 49, pp. 619–627, 2011.
- [7] K. J. Lee and K. D. Woo, “Effect of pre-aging conditions on bake-hardening response of Al-0.4 wt%Mg-1.2 wt%Si-0.1 wt%Mn alloy sheets,” *Journal of Korean Institute of Metals and Materials*, vol. 49, no. 6, pp. 448–453, 2011.
- [8] F. Cardellini, V. Contini, R. Gupta et al., “Microstructural evolution of Al-Fe powder mixtures during high-energy ball milling,” *Journal of Materials Science*, vol. 33, no. 10, pp. 2519–2527, 1998.
- [9] H. S. Kim, S. J. Kim, H. R. Lee, C. W. Won, S. S. Cho, and B. S. Chun, “Compaction behavior of rapidly solidified Al-Si-Fe-Cr alloy powders,” *Scripta Materialia*, vol. 37, no. 11, pp. 1715–1719, 1997.
- [10] M. Krasnowski, A. Grabias, and T. Kulik, “Phase transformations during mechanical alloying of Fe-50% Al and subsequent heating of the milling product,” *Journal of Alloys and Compounds*, vol. 424, no. 1-2, pp. 119–127, 2006.
- [11] M. Tavooi, M. H. Enayati, and F. Karimzadeh, “Crystallisation process of Al₈₀Fe₁₀Ti₁₀ amorphous phase,” *Powder Metallurgy*, vol. 54, no. 3, pp. 445–449, 2011.
- [12] M. Tavooi, F. Karimzadeh, M. H. Enayati, S. H. Joo, and H. S. Kim, “Amorphous phase formation in Al₈₀Fe₁₀M₁₀ (M = Ni, Ti, and V) ternary systems by mechanical alloying,” *Journal of Materials Science*, vol. 46, no. 23, pp. 7633–7638, 2011.
- [13] A. Inoue, “Amorphous, nanoquasicrystalline and nanocrystalline alloys in Al-based systems,” *Progress in Materials Science*, vol. 43, no. 5, pp. 365–520, 1998.
- [14] S. J. Hong, T. S. Kim, H. S. Kim, W. T. Kim, and B. S. Chun, “Microstructural behavior of rapidly solidified and extruded Al-14wt%Ni-14wt%Mm (Mm, Misch metal) alloy powders,” *Materials Science and Engineering A*, vol. 271, no. 1-2, pp. 469–476, 1999.
- [15] S.-C. Park, M.-S. Kim, K.-T. Kim, S.-Y. Shin, J.-K. Lee, and K.-H. Ryu, “Compressive deformation behavior of Al-10Si-5Fe-1Zr powder alloys consolidated by spark plasma sintering process,” *Journal of the Korean Institute of Metals and Materials*, vol. 49, pp. 853–859, 2011.
- [16] C. S. Han and S. O. Han, “A study on the fabrication and structural properties of Al-Co/AlN-Co thin films,” *Journal of Korean Institute of Metals and Materials*, vol. 49, no. 3, pp. 256–263, 2011.
- [17] I.-H. Kim, B.-S. Chun, and S.-J. Hong, “The effects of electron beam irradiation direction on mechanical properties and microstructural characteristics of thick Al 5052 alloy plate,” *Metals and Materials International*, vol. 17, no. 2, pp. 357–363, 2011.
- [18] D.-H. Ahn, H. S. Kim, and Y. Estrin, “A semi-phenomenological constitutive model for hcp materials as exemplified by alpha titanium,” *Scripta Materialia*, vol. 67, no. 2, pp. 121–124, 2012.
- [19] H. S. Kim, “Hardening behaviour of partially crystallised amorphous Al alloys,” *Materials Science and Engineering A*, vol. 304-306, no. 1-2, pp. 327–331, 2001.
- [20] H. Gleiter, “Materials with ultrafine microstructures: retrospectives and perspectives,” *Nanostructured Materials*, vol. 1, no. 1, pp. 1–19, 1992.
- [21] G. W. Nieman, J. R. Weertman, and R. W. Siegel, “Mechanical behavior of nanocrystalline metals,” *Nanostructured Materials*, vol. 1, no. 2, pp. 185–190, 1992.
- [22] C. Suryanarayana, “Mechanical alloying and milling,” *Progress in Materials Science*, vol. 46, no. 1-2, pp. 1–184, 2001.
- [23] F. Zhou, R. Lück, M. Scheffer, D. Lang, and K. Lu, “The crystallization process of amorphous Al₈₀Fe₂₀ alloy powders prepared by ball milling,” *Journal of Non-Crystalline Solids*, vol. 250–252, pp. 704–708, 1999.
- [24] Y. B. Kim, H. M. Park, W. Y. Jeung, and J. S. Bae, “Vacuum hot pressing of gas-atomized Ni-Zr-Ti-Si-Sn amorphous powder,” *Materials Science and Engineering A*, vol. 368, no. 1-2, pp. 318–322, 2004.
- [25] K. Hanada, Y. Murakoshi, H. Negishi, and T. Sano, “Microstructures and mechanical properties of Al-Li/SiCp composite produced by extrusion processing,” *Journal of Materials Processing Technology*, vol. 63, no. 1–3, pp. 405–410, 1997.
- [26] M. J. Tan and X. Zhang, “Powder metal matrix composites: selection and processing,” *Materials Science and Engineering A*, vol. 244, no. 1, pp. 80–85, 1998.
- [27] H. S. Kim and D. N. Lee, “Power-law creep model for densification of powder compacts,” *Materials Science and Engineering A*, vol. 271, no. 1-2, pp. 424–429, 1999.
- [28] S. C. Yoon, S. J. Hong, S. I. Hong, and H. S. Kim, “Mechanical properties of equal channel angular pressed powder extrudates of a rapidly solidified hypereutectic Al-20 wt% Si alloy,” *Materials Science and Engineering A*, vol. 449–451, pp. 966–970, 2007.
- [29] A. Saleh, S. Heshmati-Manesh, S. Sheibani, and A. Ataie, “Consolidation of nano-crystalline copper powder by cold and

- hot pressing," *Metals and Materials International*, vol. 17, no. 5, pp. 749–753, 2011.
- [30] H. Kwon, M. Leparoux, J.-M. Heintz, J.-F. Silvain, and A. Kawasaki, "Fabrication of single crystalline diamond reinforced aluminum matrix composite by powder metallurgy route," *Metals and Materials International*, vol. 17, no. 5, pp. 755–763, 2011.
- [31] JCPDS 50-0797, International Centre for Diffraction Data, 2012.
- [32] JCPDS 14-0451, International Centre for Diffraction Data, 2012.

Research Article

Elastic Modulus Determination of Al-Cu Film Alloys Prepared by Thermal Diffusion

E. Huerta,^{1,2} A. I. Oliva,¹ F. Avilés,³ J. González-Hernández,² and J. E. Corona¹

¹Departamento de Física Aplicada, Centro de Investigación y de Estudios Avanzados del IPN Unidad-Mérida, A.P. 73-Cordemex, 97310 Mérida, YUC, Mexico

²Materiales Nanoestructurados, Centro de Investigación en Materiales Avanzados, S.C., Avenida Miguel de Cervantes 120, Complejo Industrial Chihuahua, 31109 Chihuahua, CHIH, Mexico

³Unidad de Materiales, Centro de Investigación Científica de Yucatán A.C., Calle 43 No. 130 Col. Chuburná de Hidalgo, 97200 Mérida, YUC, Mexico

Correspondence should be addressed to E. Huerta, microsco@mda.cinvestav.mx

Received 8 May 2012; Accepted 19 June 2012

Academic Editor: Hamed Bahmanpour

Copyright © 2012 E. Huerta et al. This is an open access article distributed under the Creative Commons Attribution License, which permits unrestricted use, distribution, and reproduction in any medium, provided the original work is properly cited.

Elastic moduli of 50–250 nm thick Al-50 at % Cu film alloys deposited by thermal evaporation on Kapton substrates and postformed by thermal diffusion are investigated. Formation of the Al₂Cu alloy phase was confirmed by X-ray photoelectron spectroscopy (XPS). Surface morphology was examined by atomic force microscopy (AFM) and scanning electron microscopy (SEM) before and after tensile mechanical testing. Force-strain curves of the Al-Cu alloy were obtained by subtracting the effect of the force-strain Kapton curves from the corresponding curves of the Al-Cu/Kapton system. A reduction in the elastic modulus of the Al-Cu alloys from 106.1 to 77.8 GPa with the increase of alloy thickness was obtained. Measured elastic moduli were between the reported bulk modulus for Al and Cu. Reductions in the surface roughness and increments in the grain size were measured after tensile testing of the Al-Cu alloys.

1. Introduction

The current tendency in the electronic industry is to use flexible polymers as substrates to fabricate electronic circuits, rendering portable, low-cost, low-weight, and flexible electronic devices. For this reason, it is necessary to determine and understand the behavior of the physical properties of nanofilms deposited on flexible substrates [1, 2]. Particular attention needs to be paid to the understanding of the mechanical properties, especially the elastic modulus. Among the different methods used to estimate the elastic modulus of thin film materials are those based on vibrations [3], tensile [4], and bending testing [5]. In the electronic industry, the aluminum-copper alloys (Al-Cu) are used as metallic interconnectors [6], because of the reduction of the electromigration effects in aluminum [7]. The inclusion of polymeric materials as substrates in the electronic devices fabrication makes the interconnectors and electronic components suffer strains by Joule effect

during their operation. Thus, it is important to study the mechanical behavior of these devices by knowing the elastic modulus of the interconnector materials at nanothicknesses for improving their performance. Figure 1 shows the Al-Cu alloy phase diagram in bulk [8, 9] where different phases can be observed. Al-Cu alloy phases β_0 , β , γ_0 , and ε_2 are formed from 1373 to 823 K, while θ (Al₂Cu) [10], η_1 (AlCu), ξ_2 (Al₃Cu₄), δ (Al₂Cu₃), and γ_1 (Al₄Cu₉) appear as stable phases below 823 K. As can be seen, the formation of the different phases is mainly determined by the concentration of each element and the cooling rate during solidification [11, 12]. An important crystallographic phase with adequate electrical characteristics for the microelectronic industry is the AlCu phase (η_1), which is a stoichiometric phase formed below 823 K.

In this work, the elastic modulus of Al-50 at. % Cu alloy films with 50–250 nm thickness, prepared by thermal evaporation on Kapton 50HN flexible substrates and post thermal diffusion, is investigated. The morphology and

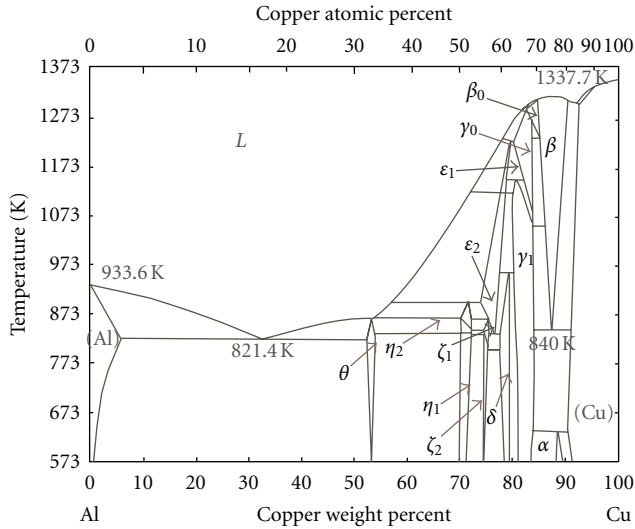


FIGURE 1: Phase diagram of the bulk Al-Cu alloy.

mechanical properties of the Kapton foil substrate and metallic alloys were investigated in order to determine features and properties of the formed Al-Cu alloy from differences with the bare substrate. Pure Al and Cu 50 nm thickfilms were also analyzed for comparison.

2. Materials and Methods

2.1. Alloys Preparation and Substrate Selection. For Al-Cu alloys preparation, high-purity Cu (99.999%) from CERAC was first deposited on 12.5 μm thick Kapton (50HN) foil substrates by thermal evaporation into a vacuum chamber with a pressure of 6.0×10^{-5} Torr and a deposition rate of 0.2 nm/s. Film thickness and deposition rate were measured and monitored in situ with a TM-400 controller with a quartz crystal sensor. High-purity Al (99.999%) was subsequently deposited on the Cu/Kapton system, forming an Al/Cu bilayer on top of the Kapton substrate. The chosen order of deposition is related to the rapid and continuous oxidation of Cu in comparison with the high stability of the Al oxide. The Al-Cu alloys were prepared with a nominal 50:50% atomic concentration and deposited with 50, 100, 150, 200, and 250 nm as total thickness. The corresponding individual film thicknesses for this atomic concentration were calculated as $t_{\text{Al}} = 58.4\%$ and $t_{\text{Cu}} = 41.6\%$ of the total thickness. Four samples were simultaneously deposited for each batch. Once the bilayers were formed, Al-Cu alloys were post-formed by thermal diffusion at 673 K by a thermal annealing process during 3 h into a vacuum oven with Argon gas to avoid oxidation. The natural cooling process of the oven, from 673 K to 313 K, required 2 additional hours of the films into the Argon atmosphere. Due to the annealing process, the Al-Cu/Kapton alloys suffered thermal stresses as observed by curling of the samples. The residual stress is assumed to arise from shrinkage of the substrate up to 1% at 673 K (as reported by the supplier) and by the thermal diffusion of the material [13–16]. Additionally, 50 nm thick

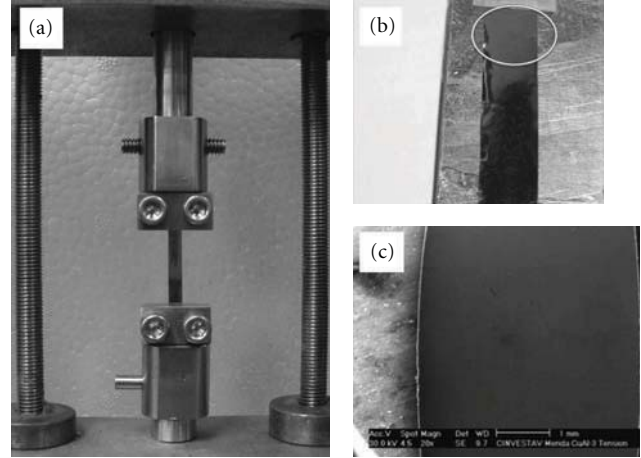


FIGURE 2: (a) Sample pressed by the clamps, (b) detail of the sample surface after tensile testing, and (c) micrograph of the nondamaged grip zone of the sample.

samples of only Al and only Cu were thermally deposited to prepare Al/Kapton and Cu/Kapton systems to be used as references. Kapton was selected as the substrate material due to its high melting temperature, smooth surface, and relatively low elastic modulus. The surfaces morphology of Kapton as-received and after thermal annealing at 673 K as well as used for the metallic alloys were examined by atomic force microscopy (AFM) in tapping-mode. AFM images of $2 \times 2 \mu\text{m}^2$ size, 512×512 pixels² of resolution, and 1 Hz as scanning rate were obtained. Preliminary results of the mechanical properties of Kapton 50HN substrates and Al-Cu/Kapton alloys were reported [17] and determined from strain-stress curves obtained from a homemade universal testing machine [18] with a load cell of 220 N. The sample strain was measured by using the machine cross-head displacement, taking into account the compliance of the universal testing machine. The machine compliance, estimated as $0.16 \mu\text{m}/\text{N}$, is small enough to avoid affectation on the elastic modulus determination. Tensile tests of samples were performed with a cross-head speed of $1 \mu\text{m}/\text{s}$ (strain rate of $6.0 \times 10^{-5} \text{ s}^{-1}$). The gauge length (distance between clamps) used for the tensile testing machine was 20 mm. Samples of rectangular geometry of 40 mm length and 4 mm wide were used for tensile tests. No damages with the clamps were produced on the sample surfaces after tensile testing during sample holding. This can be observed in Figure 2, where a sample pressed by the clamps is shown (Figure 2(a)); meanwhile in Figures 2(b) and 2(c), micrographs of the nondamaged grip zone of the sample after the tensile testing can be observed with different magnifications.

2.2. Characterization of the Al-Cu Alloys. Phases of the Al-Cu alloy were investigated by X-ray photoelectron spectroscopy (XPS). XPS analysis was performed by an ESCA/SAM 560 Perkin-Elmer equipment. The analysis was performed at 0.5–3.0 nm-depth from the sample surface (about 3 atomic layers), given the erosion rate used during analysis. Images of the surface morphology of the Al-Cu alloys surfaces

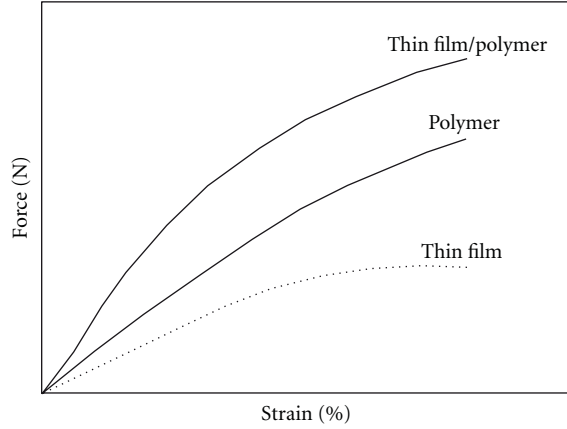


FIGURE 3: Force-strain curves of the thin film/polymer and polymer substrate systems, and the corresponding thin film curve obtained by subtraction.

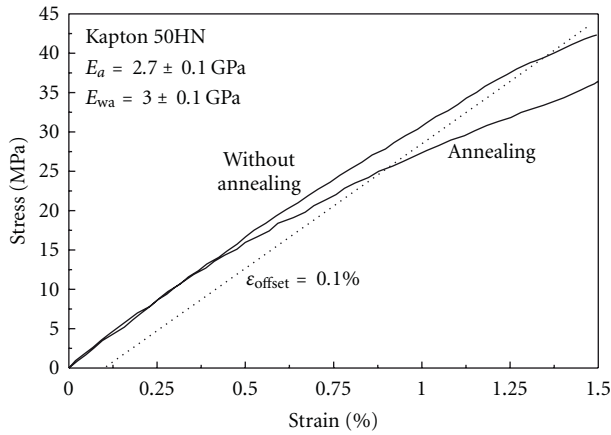


FIGURE 4: Stress-strain curves of 12.5 μm thick Kapton foil for as-received and after thermal annealing.

were examined by atomic force microscopy (AFM). Rms-roughness (R_{rms}) and grain size (D) before and after the tensile tests were measured using the scanning probe image processor (SPIP) software from Image Metrology Co. The microstructure of the Al-Cu alloys was examined by a scanning electron microscopy (SEM), both by secondary electrons (surface) and by backscattered electrons (to identify elemental composition on different zones of the alloy) with 25 keV using a SEM-Philips XL30 ESEM. Additionally, elemental concentration from different zones of the formed alloys was measured by energy dispersive spectroscopy (EDS).

2.3. Elastic Modulus of the Al-Cu Alloys. Two tensile tests were carried out for each system, one with the metallic alloy/substrate and the second one without the metallic film. The first tensile test was carried out to the Al-Cu alloy bonded to the Kapton substrate to obtain the force-strain curve of the complete Al-Cu/Kapton system. The Al-Cu film alloy was then removed from the Kapton substrate by etching

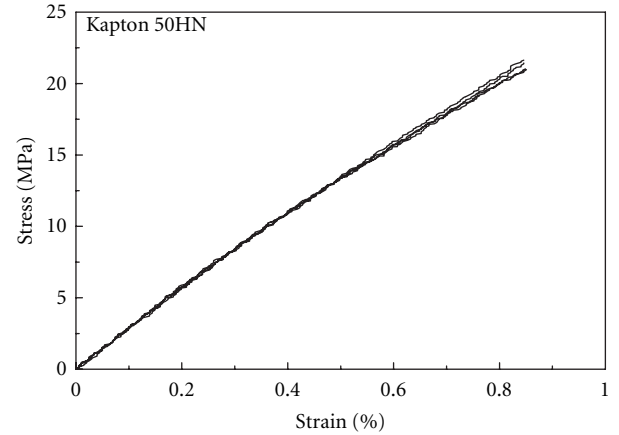


FIGURE 5: Four stress-strain curves obtained for 12.5 μm thick Kapton substrate after thermal annealing and etching. A high reproducibility was observed from the tensile tests presented in the plot.

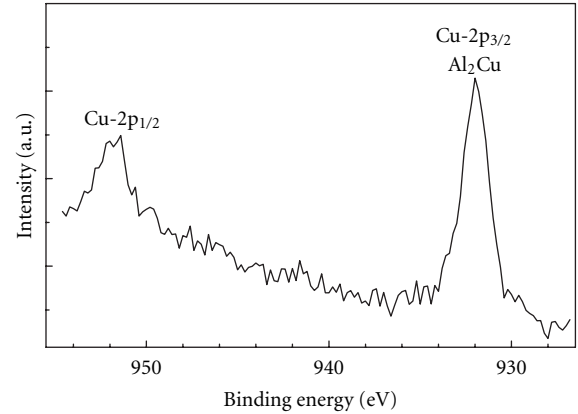


FIGURE 6: XPS spectrum as obtained for an Al-50 at % Cu alloy sample.

the alloy during 5 minutes into a weak sulfuric acid solution. This process etched the metallic film without affecting the elastic modulus of the substrate as was confirmed by the tensile testings of the Kapton substrates before and after film etching. The second tensile test was subsequently performed to the etched substrate to obtain the force-strain curve of the bare substrate. The tensile stress (σ) of the alloy as a function of applied strain (ϵ) was calculated by subtracting the force-strain curve of the Kapton substrate $F_{\text{sub}}(\epsilon)$, from the force-strain curve corresponding to the Al-Cu/Kapton foil $F_{\text{tot}}(\epsilon)$, according to the relation [19],

$$\sigma(\epsilon) = \frac{1}{t_f w_f} [F_{\text{tot}}(\epsilon) - F_{\text{sub}}(\epsilon)], \quad (1)$$

where t_f and w_f are the thickness and width of the alloy, respectively. Force-strain curves of the thin film/polymer system, polymer substrate, and the thin film curve, used to obtain the mechanical properties of the thin films, are plotted in Figure 3. The lower dashed-line curve in Figure 3 corresponds to the curve of the thin film, which was

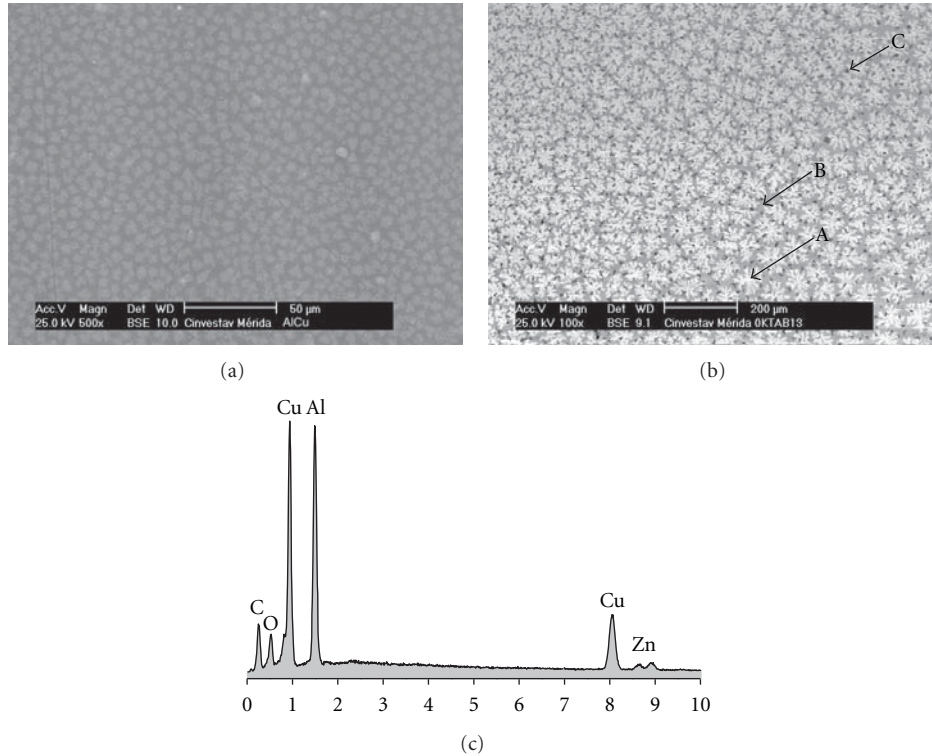


FIGURE 7: SEM images showing the microstructure evolution when the sample is annealed: (a) 1 h to (b) 3 h. (c) EDS results corresponding to the sample annealed for 3 h.

obtained by subtracting the measured force-strain curve of the polymer substrate from the force-strain curve of the thin film/polymer system.

Additionally, batches of only Al and Cu films of 50 nm thick deposited on similar Kapton substrates were analyzed by this method to estimate their corresponding elastic modulus.

3. Results and Discussion

3.1. Substrate Analysis. The surface morphology of Kapton substrate both before and after the annealing process was measured by AFM, finding no significant changes in the rms-roughness. Rms-roughness values of the Kapton surface were determined in a range of 1.1–2.9 nm, confirming that Kapton foil presents a uniform low-roughness surface which is suitable to use as a substrate for depositing alloy films with uniform thickness and low-roughness. Additionally, the mechanical properties of Kapton substrates were examined before and after thermal annealing. Figure 4 shows two stress-strain curves from Kapton foil obtained from as-received, and after 3 h of annealing treatment. Both as-received and annealed Kapton foil present an initial linear elastic behavior for low strain values ($\epsilon \leq 1.3\%$). The rule of $\epsilon = 0.1\%$ offset applied to both stress-strain curves yields deviations from linearity at $\epsilon = 1.3\%$ for the as-received Kapton and $\epsilon = 0.9\%$ for the annealed Kapton.

The corresponding elastic moduli were estimated by fitting a straight line into this region. The corresponding

mean value of the elastic modulus obtained in this way for as-received Kapton is $E_{wa} = 3.0 \pm 0.1$ GPa, meanwhile for annealed Kapton is $E_a = 2.7 \pm 0.1$ GPa, that is, a reduction of elastic modulus of $\sim 10\%$ for the annealed Kapton. This slight reduction of the elastic modulus was taken into account to estimate the elastic modulus of the Al-Cu alloys, such that the annealed curve was used for subsequent calculations. For the case of pure metallic films (Cu and Al), the elastic modulus was estimated using the mechanical properties of as-received Kapton since no annealing process is involved. Figure 5 shows the stress-strain curves corresponding to the elastic zone of only Kapton obtained after 3 h of thermal annealing and etching during 5 minutes into a weak sulfuric acid solution. The obtained stress-strain curves of the substrate show high reproducibility for the different replicates tested. For all tensile tests, a strain range of 0.9% was used to estimate the elastic modulus. Negligible variations in the estimated elastic modulus of the annealed Kapton ($E_a = 2.7$ GPa) after etching into a weak sulfuric acid solution were observed. At this strain range, Kapton substrate is into the elastic zone and does not suffer damage that can affect the mechanical properties of the films. Once Kapton substrate was characterized, the tensile tests of the Al-Cu/Kapton system were conducted.

3.2. Phase Alloy Analysis. The formed phases of the prepared Al-Cu/Kapton alloys were determined by XPS. XPS spectra in the 1000–0 eV energy range were obtained. Subsequent high-resolution XPS spectra of Al-2p, Cu-2p_{1/2}, and Cu-2p_{3/2}

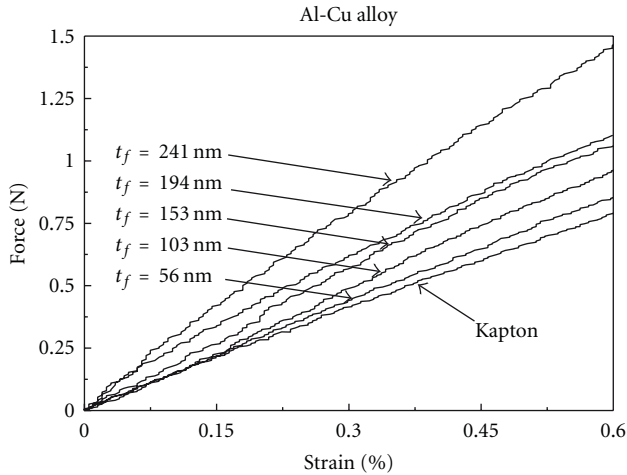


FIGURE 8: Measured force-strain curves of Kapton foil and Al-Cu/Kapton systems for different thicknesses. Thickness values correspond to the deposited values.

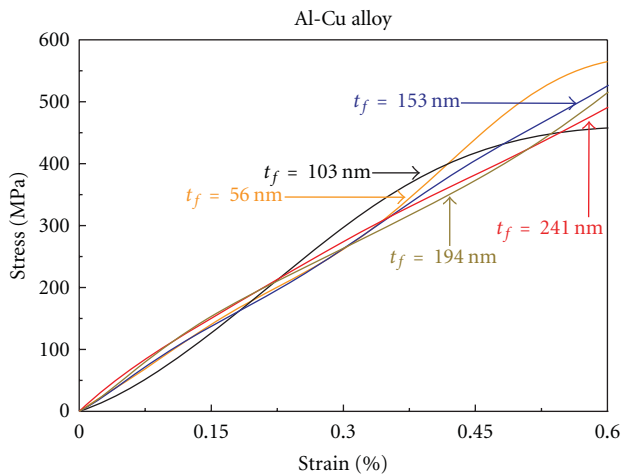


FIGURE 9: (color online) Stress-strain curves as obtained for Al-50 at % Cu alloys with different thicknesses.

were determined, as is shown in Figure 6. The main Al peak (Al-2p) appearing at 74 eV (not shown) corresponds to an oxidized state of Al. The Cu spectrum consists of a set of $2p_{1/2}$ and $2p_{3/2}$ peaks, associated to the Al_2Cu phase [20]. According to the Al-Cu bulk phases diagram for an Al-50 at % Cu, the expected phase is AlCu. However, Al_2Cu phase may also be produced during the cooling process [21].

3.3. Microstructure and Morphology of Al-Cu Alloys. The microstructure of the Al-Cu alloys was analyzed by EDS-SEM technique using the backscattered secondary electrons mode. Figures 7(a) and 7(b) show two SEM images of the alloy microstructure after the annealing time of 1 h and 3 h, respectively. As can be observed in Figure 7(a) the alloy is not formed completely given the minor time of the annealed

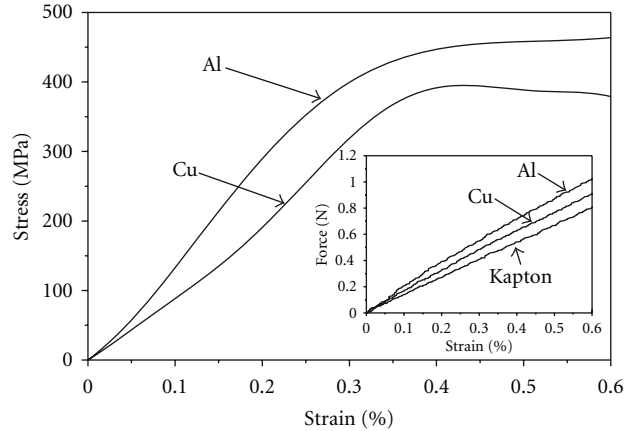


FIGURE 10: Stress-strain curves for 50 nm-thick of Al and Cu. Inset shows the corresponding force-strain curve.

treatment. Microstructure of the alloy annealed during 3 h shows to be more homogeneous than for annealed films after 1 h. Figure 7(b) shows three analyzed zones of the Al-Cu alloy which was labeled as: white zone (A), gray zone (B), and dark points (C). Zone A is characterized by the dendritic structures. Stoichiometry of the zone A yields concentrations of Al = 41.7% at and Cu = 58.3% at. Zone B is characterized by the peripheral dendritic structures, with atomic concentration of Al = 46.0% and Cu = 54.0%. Dark points C, with concentrations of Al = 53.2% and Cu = 46.8%, are characterized by the highest concentration of aluminum. From EDS analysis, zone A was found to be richer of Cu than the B and C zones. Figure 7(c) shows an EDS general analysis of the sample annealed for 3 h. Additionally, evidence of diffusion of Cu or Al into the Kapton foil during the annealing process was not found, which was confirmed by the EDS analysis carried out in localized areas of the Kapton where the Al-Cu alloy was removed.

3.4. Alloys Tensile Tests. Figure 8 shows representative force-strain curves of the Al-Cu/Kapton system deposited with different film thicknesses ($t_f = 50$ to 250 nm, nominal values) and of neat Kapton substrate as the baseline. Representative force-strain curves from four samples for each Al-Cu/Kapton system and the corresponding curve for Kapton substrate are included.

Reported thickness values correspond to the deposited thicknesses of the formed Al-Cu alloy as measured by the quartz crystal sensor during thermal evaporation. As can be observed, the slope of the force-strain curve increases as the film thickness increases. The corresponding stress-strain curves of the Al-Cu alloys prepared with different thickness were calculated using Figure 8 and Equation (1) and are shown in Figure 9. From each curve of Figure 9, the elastic moduli of different Al-Cu alloys were estimated.

The elastic modulus values were estimated as the initial slope of the straight line of each curve in the range of $0 \leq \epsilon \leq 0.6\%$, that is, within the linear elastic regime. The mean values and the corresponding standard deviations estimated

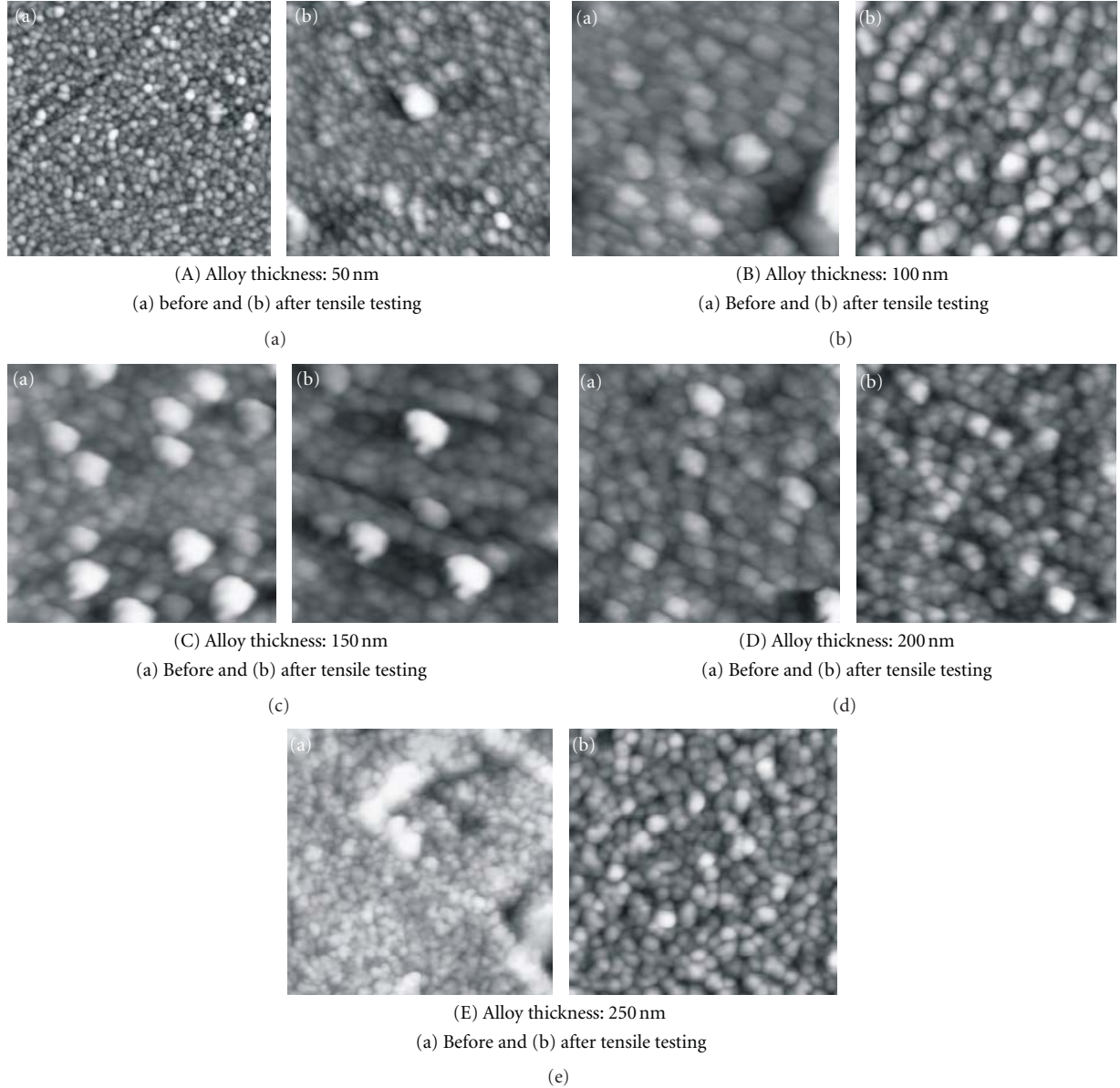


FIGURE 11: AFM images ($2 \times 2 \mu\text{m}^2$) of the Al-Cu film morphology for different thicknesses, before and after tensile testing, (A) 50 nm, (B) 100 nm, (C) 150 nm, (D) 200 nm, and (E) 250 nm.

TABLE 1: The mean elastic modulus of Al-Cu alloys, Al and Cu with different thickness.

Thickness (nm)	Al-Cu (GPa)	Al (GPa)	Cu (GPa)
50	104.6 ± 6.2	129.1 ± 4.2	107.1 ± 4.6
100	99.1 ± 1.8	—	—
150	106.1 ± 5.5	—	—
200	77.8 ± 1.6	—	—
250	82.7 ± 5.6	—	—

for the elastic modulus are shown in Table 1. From Table 1, it can be observed that the elastic modulus decreases as the alloy thickness increases. Table 1 also includes the elastic modulus as obtained for 50 nm thickness of Al and Cu films.

As known, the reported elastic modulus for Al and Cu in bulk is 70 and 130 GPa, respectively [22]. The elastic moduli of the Al-Cu film alloys fall between the bulk moduli of Al and Cu, approaching to the bulk modulus of Al as the alloy thickness increases. Additionally, the elastic moduli of 50 nm thick thermally evaporated samples of Al/Kapton and Cu/Kapton were measured for comparison. The corresponding stress-strain curves of 50 nm thick Al and Cu are shown in Figure 10. These curves were obtained from the force-strain curves shown inset. For Al films, a mean elastic modulus of 129.1 ± 4.2 GPa was obtained, a significantly higher value than its bulk value (70 GPa).

The obtained elastic modulus for Cu films was 107.1 ± 4.6 GPa, a lower value as compared with its bulk value (130 GPa). Values of 108.8 ± 11.7 GPa of the elastic modulus

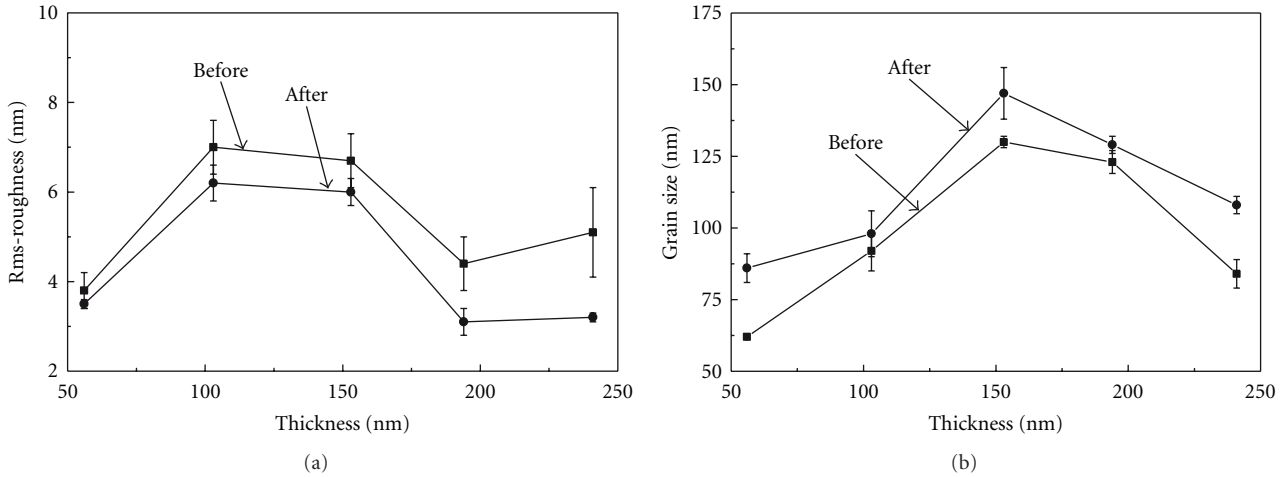


FIGURE 12: Changes on the: (a) rms-roughness, and (b) grain size both before and after tensile testing.

for Cu films have been reported by other authors [23] by using an optical diffraction technique. They report this elastic modulus value for Cu in a range of 0.1 to 2.0 μm film thickness. The lower elastic modulus value obtained herein for 50 nm-thick Cu film may be explained by the lack of coalescence among grains or clusters for such a small film thickness, which seems to be particularly relevant for copper. This affirmation is also supported by the high electrical resistivity reported for Cu films of 50 nm thickness [24].

After mechanical testing, the elongated surfaces of the tested alloys were examined by SEM. SEM analysis did not show microcracks on the surface of the elongated alloys, confirming that loading was kept within the elastic regime. The surface morphology was also obtained by AFM in order to examine differences with the pristine condition (prior to testing). Figure 11 shows sequential AFM images of the Al-Cu alloys deposited with different thickness, corresponding to scenarios before and after tensile testing (images do not correspond to the same zone). As-grown images obtained from different zones of each alloy showed similar rms-roughness values, suggesting a homogeneous growth condition during evaporation.

From AFM images, the rms-roughness (R_{rms}) and the mean grain size (D_{mean}) were measured for each thickness of Al-Cu alloy both before and after tensile testing. Their corresponding mean values and standard deviations are shown in Figure 12. Both R_{rms} and D_{mean} show an initial increment with increased film thickness until maximum values are reached at alloy thickness of 150 nm; after alloy thickness of 150 nm, the R_{rms} and D_{mean} values show a slight reduction. The largest values of the roughness and grain size both before and after tensile testing were found for the 150 nm thick alloy. After deformation, the initial surface roughness value decreases, meanwhile the initial grain size increases.

After annealing (alloy formation), diffusion process and diffusion time affect the final surface of alloys given the dependence of R_{rms} and D_{mean} with the film thickness

and formation temperature. In our case, the 150 nm thick Al-Cu film suffered the largest surface morphology changes may be due to the combined action of the alloy thickness, diffusion temperature, and diffusion time. The diffusion process discussed here for Al-Cu film formation was found to be a different behavior than the growth process, where according to the scaling laws, the rms-roughness value and the grain size of the surface increase with increased thickness (or deposition time) until a saturation is reached.

4. Conclusions

The elastic modulus of 50–250 nm thick Al-50 at.% Cu alloys thermally evaporated onto Kapton substrates and postformed by thermal diffusion has been investigated. Al₂Cu phase was the dominant crystalline phase formed as determined by XPS. Force-strain curves of the Al-Cu alloys were obtained by subtracting the force-strain curve of the Kapton substrate from the force-strain curve of the Al-Cu/Kapton material system, and elastic modulus was obtained from the slope of the corresponding stress-strain curves. Elastic modulus of the Al-Cu alloys decreased when the film thickness increased, and their values were determined in the range from 106.1 to 77.8 GPa for 50 to 250 nm thick alloys, respectively. The elastic modulus of the studied Al-Cu alloys was found between the corresponding bulk values of the Al and Cu films. The elastic modulus measured for 50 nm thick Al was higher than its corresponding bulk value, while the elastic modulus of 50 nm thick Cu was smaller than its bulk value. The highest values of the mean grain size and rms-roughness were found for the 150 nm thick Al-Cu alloy. Overall, application of a tensile strain/stress yielded a tendency to increase the grain size and decrease the surface roughness of the alloys. The methodology used to obtain the elastic modulus does not yield alloy microfractures because of the small strains (<1%) applied during tensile testing.

Acknowledgments

The authors thank the technical assistance given by Dora Huerta, W. Cauch, O. Ceh, P. Bartolo, and Alejandro May (CICY).

References

- [1] C.-T. Huang, C.-L. Shen, C.-F. Tang, and S.-H. Chang, "A wearable yarn-based piezo-resistive sensor," *Sensors and Actuators A*, vol. 141, no. 2, pp. 396–403, 2008.
- [2] S. A. Wilson, R. P. J. Jourdain, Q. Zhang et al., "New materials for micro-scale sensors and actuators. An engineering review," *Materials Science and Engineering R*, vol. 56, no. 1–6, pp. 1–129, 2007.
- [3] J. D. Shi, K. H. Wu, and G. Larkins, "A Method for measuring the elastic modulus of thin films," *Materials Characterization*, vol. 38, no. 4-5, pp. 301–303, 1997.
- [4] F. Ebrahimi and Z. Ahmed, "The effect of substrate on the microstructure and tensile properties of electrodeposited nanocrystalline nickel," *Materials Characterization*, vol. 49, no. 5, pp. 373–379, 2003.
- [5] H.-C. Hsu, S.-C. Wu, S.-K. Hsu, Y.-C. Sung, and W.-F. Ho, "Effects of heat treatments on the structure and mechanical properties of Zr-30Ti alloys," *Materials Characterization*, vol. 62, no. 2, pp. 157–163, 2011.
- [6] J. H. Han, M. C. Shin, S. H. Kang, and J. W. Morris, "Effects of precipitate distribution on electromigration in Al-Cu thin-film interconnects," *Applied Physics Letters*, vol. 73, pp. 762–764, 1998.
- [7] C. M. Tan and A. Roy, "Electromigration in ULSI interconnects," *Materials Science and Engineering R*, vol. 58, no. 1-2, pp. 1–75, 2007.
- [8] F. Habashi, *Alloy: Preparation, Properties, Application*, Edited by Q.C. Fathi Habashi, chapter 10, Wiley-VCH, 1998.
- [9] V. Zolotarevsky, N. Belov, and M. Glazoff, *Casting Aluminum Alloys*, chapter 1, Elsevier, 2007.
- [10] A. I. Oliva, J. E. Corona, and V. Sosa, "AlCu alloy films prepared by the thermal diffusion technique," *Materials Characterization*, vol. 61, no. 7, pp. 696–702, 2010.
- [11] S. S. Babu, M. K. Miller, J. M. Vitek, and S. A. David, "Characterization of the microstructure evolution in a nickel base superalloy during continuous cooling conditions," *Acta Materialia*, vol. 49, no. 20, pp. 4149–4160, 2001.
- [12] T. B. Massalski, L. F. Vassamillet, and Y. Bienvenu, "Metastable phase relationships in zinc-rich copper and silver alloys produced by rapid freezing," *Acta Metallurgica*, vol. 21, no. 5, pp. 649–661, 1973.
- [13] G. Schmitz, C. B. Ene, and C. Nowak, "Reactive diffusion in nanostructures of spherical symmetry," *Acta Materialia*, vol. 57, no. 9, pp. 2673–2683, 2009.
- [14] D. L. Beke, A. I. Szabo, Z. Erdelyi, and G. Opposits, "Diffusion-induced stresses and their relaxation," *Materials Science and Engineering A*, vol. 387–389, pp. 4–10, 2004.
- [15] D. Gupta, "Diffusion in several materials relevant to Cu interconnection technology," *Materials Chemistry and Physics*, vol. 41, no. 3, pp. 199–2005, 1995.
- [16] S. Lee, W. L. Wang, and J. R. Chen, "Diffusion-induced stresses in a hollow cylinder: constant surface stresses," *Materials Chemistry and Physics*, vol. 64, no. 2, pp. 123–130, 2000.
- [17] E. Huerta, A. I. Oliva, J. E. Corona, and J. González-Hernández, "Mechanical properties of AlCu alloys thin films prepared by thermal diffusion," in *Proceedings of the 8th International Conference on Electrical Engineering, Computing Science and Automatic Control*, pp. 1042–1047, Mérida, México, 2011.
- [18] E. Huerta, J. E. Corona, A. I. Oliva, F. Avilés, and J. González-Hernández, "Universal testing machine for mechanical properties of thin materials," *Revista Mexicana de Física*, vol. 56, no. 4, pp. 317–322, 2010.
- [19] F. Macionczyk and W. Brückner, "Tensile testing of AlCu thin films on polyimide foils," *Journal of Applied Physics*, vol. 86, no. 9, pp. 4922–4929, 1999.
- [20] L. B. Hazell, "Quantitative XPS analysis of aluminium in the presence of copper," *Surface and Interface Analysis*, vol. 33, no. 10-11, pp. 791–795, 2002.
- [21] J. P. Lokker, A. J. Böttger, W. G. Sloof, F. D. Tichelaar, G. C. A. M. Janssen, and S. Radelaar, "Phase transformations in Al-Cu thin films: precipitation and copper redistribution," *Acta Materialia*, vol. 49, no. 8, pp. 1339–1349, 2001.
- [22] P. Enghag, *Encyclopedia of the Elements*, Wiley-VCH Verlag GmbH & Co. KGaA, Weinheim, Germany, 2004.
- [23] D. Y. W. Yu and F. Spaepen, "The yield strength of thin copper films on Kapton," *Journal of Applied Physics*, vol. 95, no. 6, pp. 2991–2997, 2004.
- [24] J. M. Camacho and A. I. Oliva, "Morphology and electrical resistivity of metallic nanostructures," *Microelectronics Journal*, vol. 36, no. 3–6, pp. 555–558, 2005.

Research Article

Synthesis of Bulk Nanostructured DO₂₂ Superlattice of Ni₃(Mo, Nb) with High Strength, High Ductility, and High Thermal Stability

H. M. Tawancy

Center for Engineering Research, Research Institute, King Fahd University of Petroleum and Minerals, P.O. Box 1639, Dhahran 31261, Saudi Arabia

Correspondence should be addressed to H. M. Tawancy, tawancyhm@yahoo.com

Received 8 May 2012; Accepted 2 June 2012

Academic Editor: Amir Kajbafvala

Copyright © 2012 H. M. Tawancy. This is an open access article distributed under the Creative Commons Attribution License, which permits unrestricted use, distribution, and reproduction in any medium, provided the original work is properly cited.

We show that a bulk nanostructured material combining high strength, high ductility, and high thermal stability can be synthesized in a Ni-Mo-Nb alloy with composition approaching Ni₃(Mo, Nb). By means of a simple aging treatment at 700°C, the grains of the parent face-centered cubic phase are made to transform into nanosized ordered crystals with DO₂₂ superlattice maintaining a size of 10–20 nm after up to 100 hours of aging and corresponding room-temperature yield strength of 820 MPa and tensile ductility of 35%. Deformation of the superlattice is found to predominantly occur by twinning on {111} planes of the parent phase. It is concluded that, although the respective slip systems are suppressed, most of the twinning systems are preserved in the DO₂₂ superlattice enhancing the ductility.

1. Introduction

A common feature of bulk nanostructured materials [1–9] and intermetallic compounds [10] is relatively low ductility, which limits their usefulness as engineering materials. In the case of nanostructured materials, deformation behavior is more controlled by grain boundary migration and twinning as opposed to dislocation motion and multiplication. To improve ductility by promoting those deformation modes, research efforts have been focusing on synthesis techniques particularly severe plastic deformation [11–17]. Likewise, there has been an increasing interest in improving the ductility of intermetallic compounds and ordered alloys because of their unique combination of physical and chemical properties [18, 19].

Recently, it has been demonstrated that long-range ordering in Ni-Mo-based alloy can be used to synthesize bulk nanostructured superlattices combining high strength and high ductility [20–24]. It has been shown that the closely-related Pt₂Mo-type (Ni₂Mo), DO₂₂ (Ni₃Mo), and D1_a (Ni₄Mo) superlattices coexist during long-range ordering in these systems [22, 23], which form the basis for many

commercial alloys with important applications in the chemical process, petrochemical and power generation industries [25]. Each of these superlattices can directly be derived from the parent face-centered cubic structure by minor atoms rearrangement on {420}_{fcc} planes. In the case of the Pt₂Mo-type superlattice, every third plane is occupied by Mo atoms and planes in-between contain only Ni atoms. Likewise, for the DO₂₂ superlattice, every fourth plane is occupied by Mo atoms, and every fifth plane is occupied by Mo atoms in the case of the D1_a superlattice. Long-range ordering in these systems results in considerable strengthening corresponding to room-temperature yield strength of 800 MPa or higher [22]. However, the corresponding tensile ductility ranges from less than 5% to about 40% depending upon the exact chemical composition, which determines the most stable ordered phase and its morphology. Therefore, by balancing the chemical composition it is possible to synthesize bulk nanostructured superlattices with high strength and high ductility as demonstrated in the case of the D1_a superlattice of Ni₄Mo alloy [21, 22] and Ni-Mo-Cr alloys where the metastable Ni₂Mo with Pt₂Mo-type superlattice is stabilized by controlled amounts of Cr [23, 24]. In the case of binary

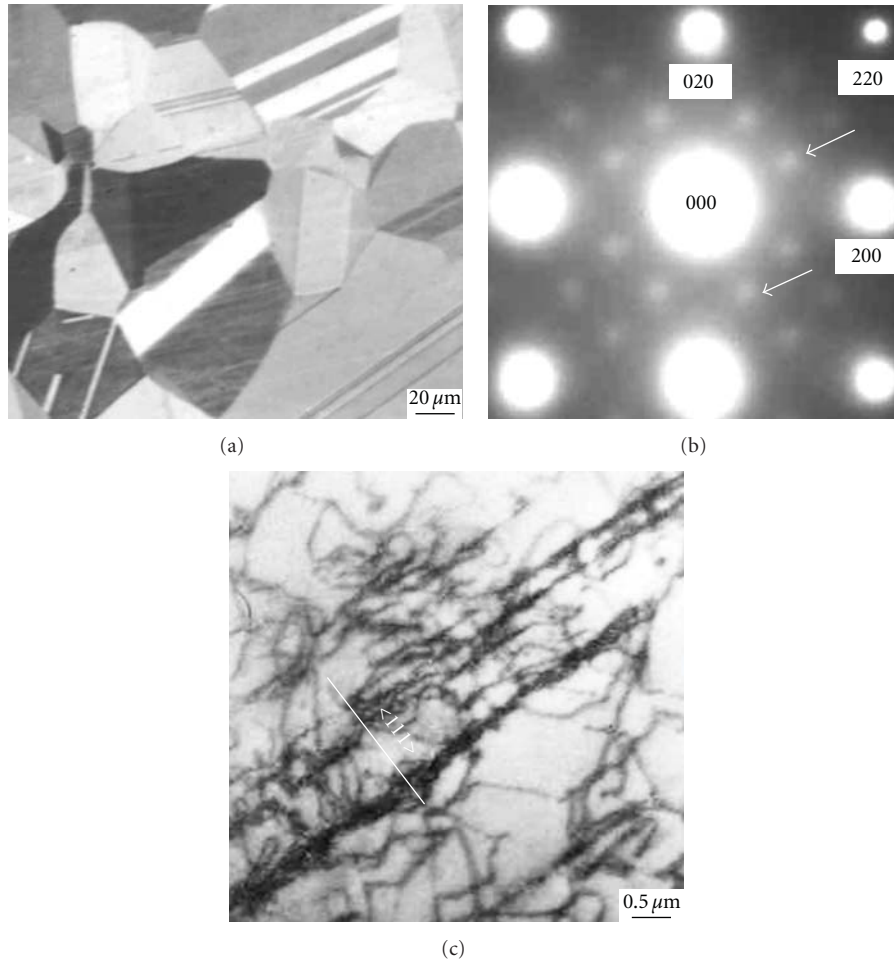


FIGURE 1: Characteristic structural features of the Ni-Mo-Nb alloy in the annealed condition (15 minutes at 1065°C). (a) Light optical micrograph showing the gross grain structure. (b) $\langle 100 \rangle$ selected-area electron diffraction pattern showing $\{1\ 1/2\ 0\}$ short-range order reflections as indicated by the arrows. (c) Bright-field TEM image showing typical deformation substructure corresponding to 10% tensile elongation at room temperature.

Ni_3Mo alloy, large thin platelets of Ni_3Mo form during the earlier stages of thermal aging rendering the material extremely hard and brittle [26]. The objective of this paper is to show that bulk nanostructured DO_{22} -type superlattice with high strength, high ductility, and high thermal stability can be synthesized in a Ni-Mo-Nb alloy with a composition approaching $\text{Ni}_3(\text{Mo}, \text{Nb})$.

2. Experimental Procedure

The alloy studied had a composition of 64.95 Ni-27.12 Mo-7.93 Nb in weight % corresponding to about 75.2 Ni-18.7 Mo-6.1 Nb in atomic %, approaching the $\text{Ni}_3(\text{Mo}, \text{Nb})$ composition. Sheets of the alloy about 1.5 mm in thickness were processed by standard techniques of vacuum induction melting, electroslag remelting, forging, hot rolling, and cold rolling. Metallographic specimens (25.4 mm \times 25.4 mm \times 1.5 mm) and tensile test specimens with 50.8 mm gage length were given recrystallization anneal at 1065°C for 15 minutes followed by water quenching.

Specimens for light optical metallography were etched in a solution consisting of 80% HCl and 20% of 15 mol % chromic acid to reveal the initial grain structure. Thermal aging experiments were carried out at 700°C for up to 100 hours followed by air cooling. All tensile tests were conducted at room temperature and the fracture surfaces were examined in the secondary electron mode of a scanning electron microscope operating at 20 keV. Thin foils for transmission electron microscopy were prepared by the jet polishing technique in a solution of 30% nitric acid in methanol. All the foils were examined at an accelerating voltage of 200 keV. Since the parent fcc structure and DO_{22} superlattice are closely related, all diffraction patterns are indexed in terms of the fcc structure.

3. Results and Discussion

Figure 1 summarizes characteristic structural features of the alloy studied in the annealed condition. The gross grain structure is shown in the light optical micrograph of

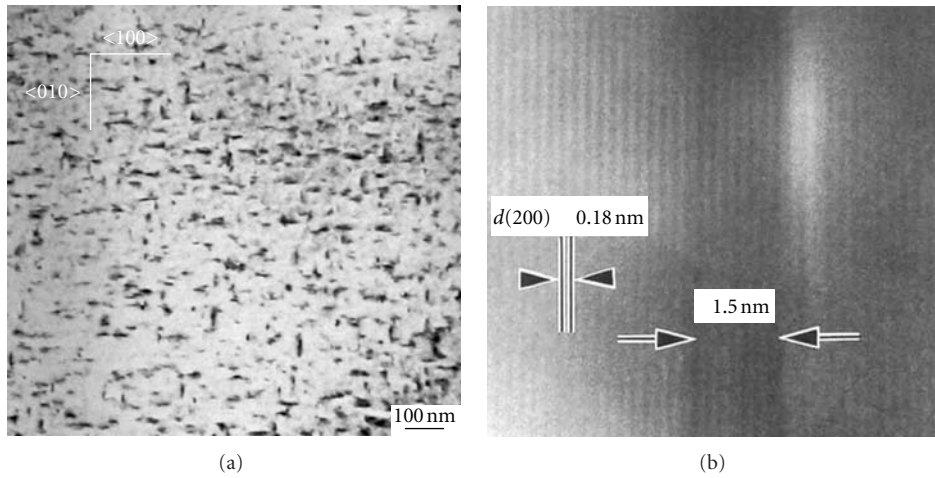


FIGURE 2: Typical microstructural features observed during the early stages of aging (15 minutes at 700°C). (a) Bright-field TEM image showing nanosized precipitates viewed along $\langle 100 \rangle$ direction. (b) Corresponding one-dimensional lattice image of $\{200\}$ planes showing a highly coherent precipitate with a thickness of about 1.5 nm.

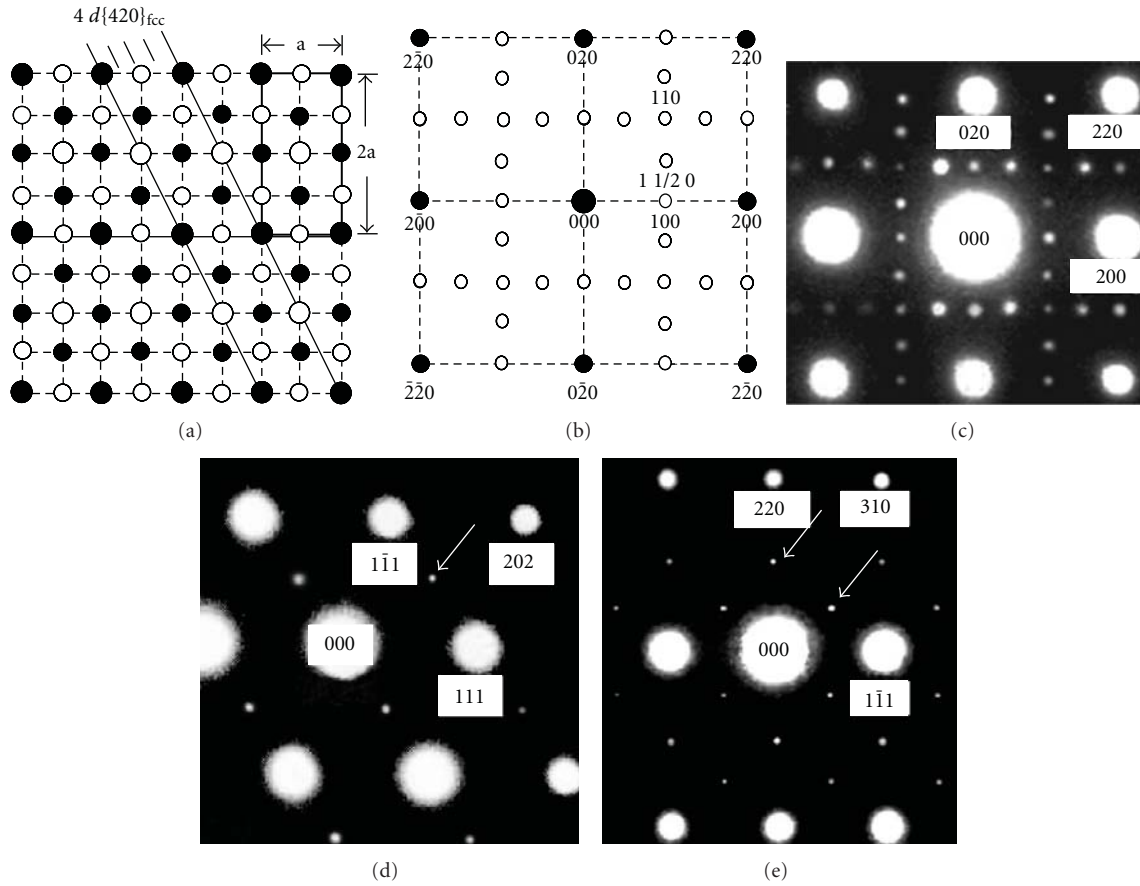


FIGURE 3: Crystallographic features of the DO_{22} superlattice. (a) Atoms arrangement viewed along $\langle 100 \rangle$ direction of the parent fcc lattice showing the tetragonal unit cell of the DO_{22} superlattice: large circles are Mo/Nb atoms (closed circles are atoms at level 0, 1 and open circles are atoms at level 1/2). (b) A schematic of the corresponding $\langle 100 \rangle$ reciprocal lattice intersection showing the characteristic DO_{22} superlattice reflections at $\{1 \frac{1}{2} 0\}$, $\{100\}$, and $\{110\}$ positions as indicated by the arrows. (c), (d), and (e) are selected-area diffraction patterns derived from specimens aged 24 hours at 700°C in $\langle 100 \rangle$, $\langle 110 \rangle$, and $\langle 112 \rangle$ orientations, respectively; the superlattice reflections are indicated by the arrows.

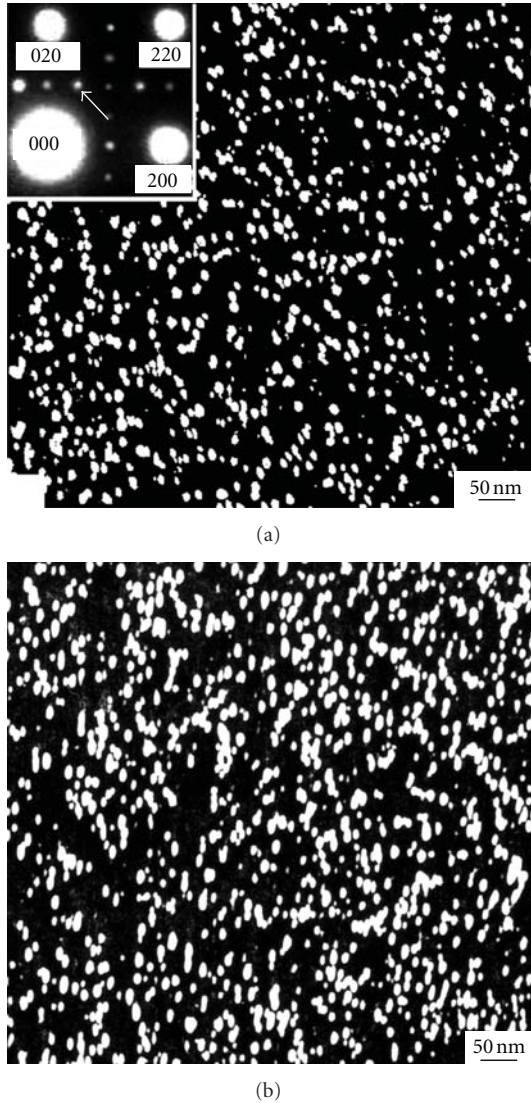


FIGURE 4: Dark-field TEM images showing effect of aging time at 700°C on the morphology of one variant of the DO₂₂ superlattice. (a) 24 hours of aging; the inset is a section of corresponding <100> diffraction pattern showing the superlattice reflection used to form the image as indicated by the arrow. (b) 100 hours of aging.

Figure 1(a). Full recrystallization is indicated by the high density of annealing twins, which typifies an fcc material with relatively low stacking fault energy [27]. Similar to the case of binary Ni-Mo alloys, the alloy contained short-range order as indicated by the appearance of diffuse intensity maxima at $\{1\ 1/2\ 0\}$ positions in the <100> electron diffraction pattern of Figure 1(b). It has been reported in an earlier study that short-range order tends to lower the stacking fault energy [28]. This is found to be consistent with the observed deformation substructure. As an example, Figure 1(c) is a bright-field TEM image showing the deformation substructure corresponding to 10% tensile elongation at room temperature. Visible slip lines (traces of $\{111\}$ planes) and the relatively low tendency for

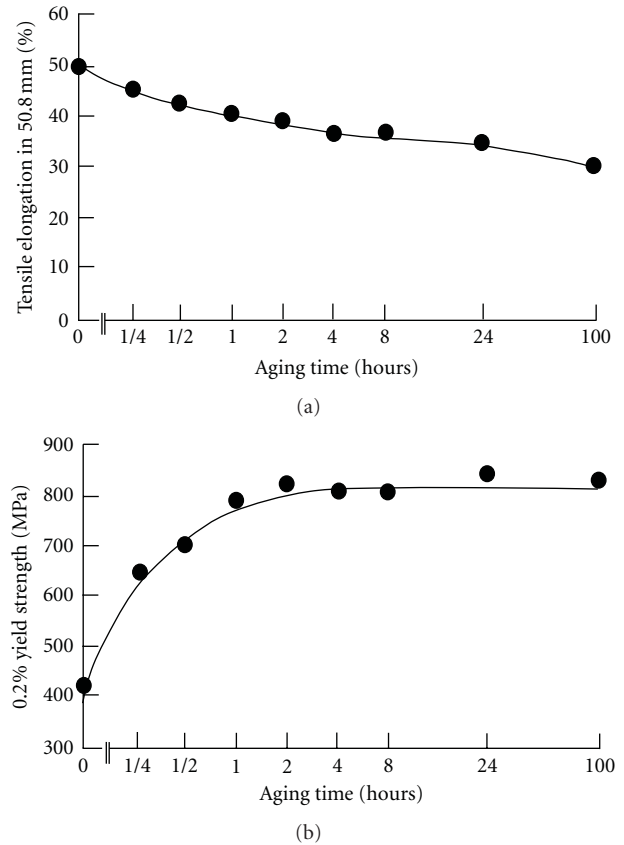


FIGURE 5: Effect of aging time up to 100 hours at 700°C on the room-temperature tensile properties. (a) Tensile elongation in 50.8 mm gage length. (b) 0.2% yield strength.

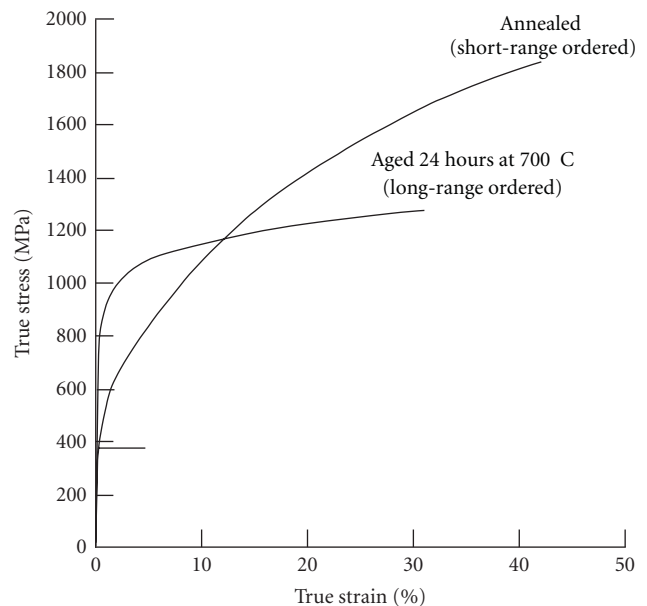


FIGURE 6: Effect of long-range ordering to the DO₂₂ superlattice on the shape of true tensile stress-strain diagram derived at room temperature.

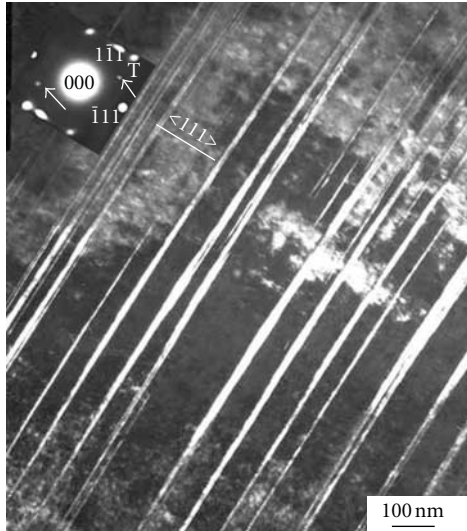
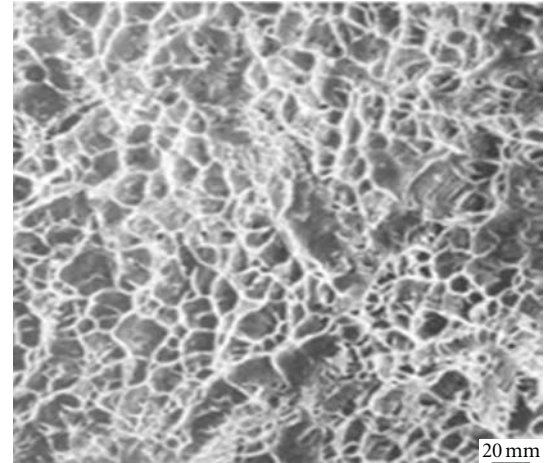


FIGURE 7: Dark-field TEM image showing $\{111\}$ twins in the deformation substructure of the DO_{22} superlattice corresponding to 10% tensile elongation at room temperature (the specimen was aged 24 hours at 700°C prior to testing). The inset is the corresponding $\langle 110 \rangle$ diffraction pattern showing the twin reflection (T) used to form the image.

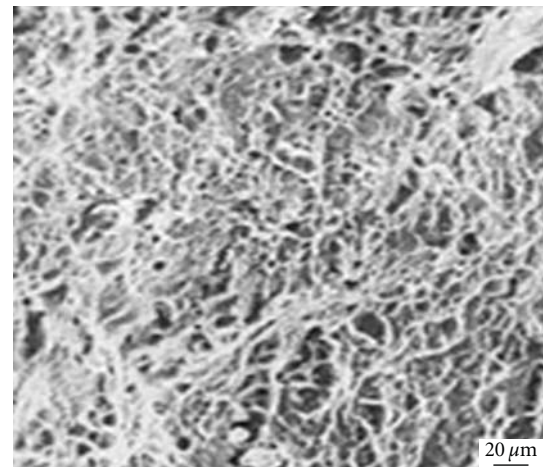
dislocation to cross slip are common features of fcc materials having relatively low stacking fault energy [27]. This has an important implication on the preferred deformation mode in the ordered state, which enhances ductility as shown later.

During the early stages of thermal aging (15 minutes at 700°C) very fine precipitates were observed as shown in the example of Figure 2. The bright-field TEM image of Figure 2(a) shows that the precipitates assume the morphology of thin short platelets revealed by elastic strain contrast. At this stage, the precipitates appeared to be too fine to produce characteristic diffraction effects. Figure 2(b) is a one-dimensional lattice image of $\{200\}$ planes showing a highly coherent precipitate with a thickness of about 1.5 nm. However, with continued thermal exposure, characteristic reflections of the DO_{22} superlattice at $\{100\}$, $\{1\ 1/2\ 0\}$, and $\{110\}$ positions were observed as demonstrated in Figure 3. A schematic illustration of the crystallographic relationship between the parent fcc lattice and DO_{22} superlattice is given in Figure 3(a). The corresponding $\{100\}$ reciprocal lattice intersection is shown in Figure 3(b), which is to be compared with the observed $\langle 100 \rangle$ diffraction pattern of Figure 3(c) obtained after 24 hours of aging at 700°C . As can be seen, the observed diffraction pattern contains the characteristic reflections of the DO_{22} superlattice. Figures 3(d) and 3(e) show corresponding diffraction patterns in $\langle 110 \rangle$ and $\langle 112 \rangle$ orientations, respectively, where only $\{110\}$ reflections can be present in the $\langle 110 \rangle$ pattern, and the $\langle 112 \rangle$ pattern can contain both the $\{1\ 1/2\ 0\}$, and $\{110\}$ superlattice reflections.

Figure 4 shows dark-field TEM images illustrating the ordered microstructure of one crystallographic variant of the DO_{22} superlattice. Both images were formed with



(a)



(b)

FIGURE 8: Secondary electron SEM images illustrating comparative tensile fracture surfaces. (a) Annealed (short-range ordered). (b) Aged 24 hours at 700°C (long-range ordered).

$\{1\ 1/2\ 0\}$ superlattice reflections as illustrated in the inset of Figure 4(a). It is observed that the superlattice assumes the morphology of nanosized particles with an average size of 10–20 nm. Also, it is observed as the aging time was extended from 24 hours (Figure 4(a)) to 100 hours (Figure 4(b)), the change in superlattice morphology was insignificant demonstrating its relatively high thermal stability. The corresponding effect of short-range order \rightarrow long-range order transformation on the room temperature tensile properties is summarized in Figure 5. After 1 hour of aging at 700°C , the 0.2% yield strength was nearly doubled reaching about 800 MPa. However, the material retained about 80% of its initial ductility in the short-range ordered state. With continued aging up to 100 hours, the material maintained a combination of high yield strength of about 820 MPa and high tensile ductility of about 35% consistent with the observed high thermal stability of the DO_{22} superlattice.

Comparative true tensile stress-strain diagrams in the short-range and long-range ordered states are shown in

Figure 6. It is noted that the strain hardening rate is significantly lowered by long-range ordering to the DO₂₂ superlattice reflecting a change in the deformation behavior. In contrast with the short-range ordered state where deformation behavior typifies an fcc material with relatively low stacking fault energy as demonstrated in Figure 1(c), twinning on {111} planes is found to be the predominant deformation mode in the long-range ordered state as illustrated in the example of Figure 7. This indicates that although long-range ordering could suppress most of the slip systems characteristic of the parent fcc lattice, many of the twinning systems remain active suggesting that the stacking fault energy of the material is further lowered by long-range ordering enhancing deformation by twinning. A similar behavior is found to occur in ordered Ni-Mo [21, 22] and Ni-Mo-Cr [23, 24] alloys.

Figure 8 shows secondary electron SEM images illustrating the morphology of tensile fractures surfaces in the annealed (short-range ordered) and aged (long-range ordered) states. Typical of ductile materials, in both cases, fracture occurred by dimple-type rupture. However, in the long-range ordered state, the dimples can be seen to be finer and shallower, which could be related to higher density of crack nucleation sites as well as relatively lower ductility in the long-range ordered state.

4. Conclusion

It is concluded that a bulk nanostructured DO₂₂ superlattice with high strength, high ductility, and high thermal stability can be synthesized in a Ni-Mo-Nb alloy with composition approaching Ni₃(Mo, Nb) by a simple aging heat treatment at 700°C. Upon thermal aging, the grains of the high-temperature fcc phase are subdivided into ordered crystals on the nanoscale (10–20 nm) with room-temperature yield strength of about 820 MPa and tensile ductility of 35%. Plastic deformation in the ordered state is found to predominantly occur by twinning on {111} planes of the parent fcc structure indicating that the superlattice preserves the twinning systems of the parent phase leading to the observed high ductility.

Acknowledgment

It is a pleasure to acknowledge the continued support of King Fahd University of Petroleum and Minerals.

References

- [1] Y. Zhao and X. Liao, "Ductility of bulk nanostructured materials," in *Materials Science Forum*, vol. 633-634, Trans Technical, Zurich, Switzerland, 2010.
- [2] C. C. Koch, "Nanostructured materials: an overview," in *Bulk Nanostructured Materials*, M. J. Zehetbauer and Y. T. Zhu, Eds., pp. 1–20, Wiley-VCH, Weinheim Germany, 2009.
- [3] E. Bitzek, C. Brandl, P. M. Derlet, and H. Van Swygenhoven, "Dislocation cross-slip in nanocrystalline fcc metals," *Physical Review Letters*, vol. 100, no. 23, Article ID 235501, 4 pages, 2008.
- [4] H. Van Swygenhoven and J. R. Weertman, "Deformation in nanocrystalline metals," *Materials Today*, vol. 9, no. 5, pp. 24–31, 2006.
- [5] Y. T. Zhu and X. Liao, "Nanostructured metals: retaining ductility," *Nature Materials*, vol. 3, no. 6, pp. 351–352, 2004.
- [6] Z. Budrovic, H. Van Swygenhoven, P. M. Derlet, S. Van Petegem, and B. Schmitt, "Plastic deformation with reversible peak broadening in nanocrystalline nickel," *Science*, vol. 304, no. 5668, pp. 273–276, 2004.
- [7] C. C. Koch, "Optimization of strength and ductility in nanocrystalline and ultrafine grained metals," *Scripta Materialia*, vol. 49, no. 7, pp. 657–662, 2003.
- [8] H. Van Swygenhoven and J. R. Weertman, "Preface to the viewpoint set on: mechanical properties of fully dense nanocrystalline metals," *Scripta Materialia*, vol. 49, no. 7, pp. 625–627, 2003.
- [9] D. Jia, Y. M. Wang, K. T. Ramesh, E. Ma, Y. T. Zhu, and R. Z. Valiev, "Deformation behavior and plastic instabilities of ultrafine-grained titanium," *Applied Physics Letters*, vol. 79, no. 5, pp. 611–613, 2001.
- [10] R. W. Cahn, "Intermetallics: new physics," *Contemporary Physics*, vol. 42, no. 6, pp. 365–375, 2001.
- [11] P. Xue, B. L. Xiao, and Z. Y. Ma, "High tensile ductility via enhanced strain hardening in ultrafine-grained Cu," *Materials Science and Engineering A*, vol. 532, pp. 106–110, 2012.
- [12] D. G. Morris and M. A. Munoz-Morris, "Microstructural refinement in alloys and intermetallics by severe plastic deformation," *Journal of Alloys and Compounds*. In press.
- [13] K. V. León, M. A. Muñoz-Morris, and D. G. Morris, "Optimisation of strength and ductility of Cu-Cr-Zr by combining severe plastic deformation and precipitation," *Materials Science and Engineering A*, vol. 536, pp. 181–189, 2012.
- [14] Y. Zhao, Y. Zhu, and E. J. Lavernia, "Strategies for improving tensile ductility of bulk nanostructured materials," *Advanced Engineering Materials*, vol. 12, no. 8, pp. 769–778, 2010.
- [15] M. A. Muñoz-Morris and D. G. Morris, "Severe plastic deformation processing of Al-Cu-Li alloy for enhancing strength while maintaining ductility," *Scripta Materialia*, vol. 63, no. 3, pp. 304–307, 2010.
- [16] Y. Zhao, T. Topping, J. F. Bingert et al., "High tensile ductility and strength in bulk nanostructured nickel," *Advanced Materials*, vol. 20, no. 16, pp. 3028–3033, 2008.
- [17] R. Z. Valiev, "The new trends in fabrication of bulk nanostructured materials by SPD processing," *Journal of Materials Science*, vol. 42, no. 5, pp. 1483–1490, 2007.
- [18] K. A. Gschneidner, M. Ji, C. Z. Wang et al., "Influence of the electronic structure on the ductile behavior of B2 CsCl-type AB intermetallics," *Acta Materialia*, vol. 57, no. 19, pp. 5876–5881, 2009.
- [19] K. Gschneidner, A. Russell, A. Pecharsky et al., "A family of ductile intermetallic compounds," *Nature Materials*, vol. 2, no. 9, pp. 587–590, 2003.
- [20] H. M. Tawancy, "Corrosion resistant Nickel-Base Alloys," US Patent no. 7, 922, 969, 2011.
- [21] H. M. Tawancy and M. O. Aboelfotoh, "Yttrium-doped nanocrystalline Ni₄Mo: ultrahigh strength and high ductility combined with useful intermetallic properties," *Journal of Materials Science*, vol. 45, no. 13, pp. 3413–3418, 2010.
- [22] H. M. Tawancy, "Long-range ordering: an approach to synthesize nanoscale Ni-Mo-based superlattices with high strength and high ductility," *Materials Science Forum*, vol. 633-634, pp. 421–435, 2010.
- [23] H. M. Tawancy and M. O. Aboelfotoh, "Application of long-range ordering in the synthesis of a nanoscale Ni₂ (Cr,Mo)

- superlattice with high strength and high ductility,” *Materials Science and Engineering A*, vol. 500, no. 1-2, pp. 188–195, 2009.
- [24] H. M. Tawancy and M. O. Aboelfotoh, “High strength and high ductility in a nanoscale superlattice of $\text{Ni}_2(\text{Cr},\text{Mo})$ deformable by twinning,” *Scripta Materialia*, vol. 59, no. 8, pp. 846–849, 2008.
- [25] F. G. Hodge, “Nickel and high-nickel alloys,” in *Corrosion and Corrosion Protection Handbook*, P. A. Schweitzer, Ed., pp. 65–69, Marcel-Dekker, New York, NY, USA, 1983.
- [26] H. M. Tawancy, “Long-range ordering behaviour and mechanical properties of Ni-Mo-based alloys,” *Journal of Materials Science*, vol. 30, no. 2, pp. 522–537, 1995.
- [27] P. R. Swann, “Dislocation arrangements in face-centered cubic materials,” in *Electron Microscopy and Strength and Crystals*, G. Thomas and J. Washburn, Eds., pp. 131–181, Wiley Interscience, New York, NY, USA, 1963.
- [28] P. R. Okamoto and G. Thomas, “On short range order and micro-domains in the Ni_4Mo system,” *Acta Metallurgica*, vol. 19, no. 8, pp. 825–841, 1971.

Research Article

Align Ag Nanorods via Oxidation Reduction Growth Using RF-Sputtering

Zhan-Shuo Hu,¹ Fei-Yi Hung,² Shoou-Jinn Chang,¹ Wei-Kang Hsieh,¹ and Kuan-Jen Chen³

¹Institute of Microelectronics, Center for Micro/Nano Science and Technology, National Cheng Kung University, Tainan 701, Taiwan

²Department of Materials Science and Engineering, Center for Micro/Nano Science and Engineering, National Cheng Kung University, Tainan 701, Taiwan

³The Instrument Center, Institute of Nanotechnology and Microsystems Engineering, National Cheng Kung University, Tainan 701, Taiwan

Correspondence should be addressed to Fei-Yi Hung, fyhung@mail.ncku.edu.tw

Received 2 March 2012; Revised 23 April 2012; Accepted 23 April 2012

Academic Editor: Amir Kajbafvala

Copyright © 2012 Zhan-Shuo Hu et al. This is an open access article distributed under the Creative Commons Attribution License, which permits unrestricted use, distribution, and reproduction in any medium, provided the original work is properly cited.

Silver nanorod arrays grew on the individual metallic silver particles after the thermal decomposition of the silver oxides. The formation of silver oxide came from the input of oxygen during sputtering. The subsequent growth of the Ag nanorods started from the single silver grain that originated from the decomposition caused by thermal reduction. This method for oxidation reduction growth used no catalysts and improved the interface effect for the lattice match. Photoluminescence of Ag nanorods was detected at 2.17 eV.

1. Introduction

One-dimensional (1D) metal nanostructures, including rods, wires, and tubes, have recently attracted interest and been applied to optical-electronic and sensing nanodevices due to their unique optical and conductive properties and thermal conductivity [1–5]. Among the various metals, silver exhibits effective thermal conductivity and the highest electrical conductivity and can be synthesized into Ag-based compounds with different compositions. Silver is more reactive than gold or platinum; therefore, silver is the most favorable candidate for various applications [6, 7]. For the silver oxide system (Ag_xO), silver can be reduced by a thermal decomposition reaction due to its low melting point and active energy [8].

One-dimensional (1D) silver nanostructures are used as the substrates to detect surface enhanced Raman scattering (SERS) and surface plasmon resonance (SPR) and for enhancing the photoluminescence of the ZnO system [9–14]. Over the last decade, many methods have been used to fabricate Ag nanowires and nanorods. Xu et al. used porous alumina templates to carry out chemical deposition for the fabrication of silver nanorod arrays [15]. Chen et al.

fabricated Ag nanowires via a polybasic process [16]. Murphy and Jana demonstrated a seed-mediated method for obtaining Ag nanowires [17]. All the aforementioned methods require a chemical solution or template to fabricate the Ag 1D nanostructure. To obviate the chemical solutions and reduce complexity, Zhao et al. grew Ag nanorod arrays using oblique angle deposition [18]. Mohanty et al. used vapor-solid phase synthesis to produce Ag nanowires [19]. Besides the aforementioned fabrications, a few literatures have demonstrated the formation of the various nanostructures by sputtering [20–23], and oxide-assisted growth has been developed for one-dimensional nanostructures in previous studies [24–26]. Notably, oxidation reduction growth (ORG) of 1D metal structures prepared using a sputtering method has never been reported. Additionally, when the bulk metal reduces to nanoscale, the luminescence will affect the electron-hole recombination due to the larger aspect ratio [27, 28].

This study has demonstrated an oxidation reduction growth (ORG) technique with mixed-gas sputtering to create Ag nanorod arrays without any chemical solutions or contamination from aqueous solution via oxide-assisted growth [29]. The ORG methodology is used to deposit an Ag buffer layer with silver oxide nanoclusters to obtain Ag

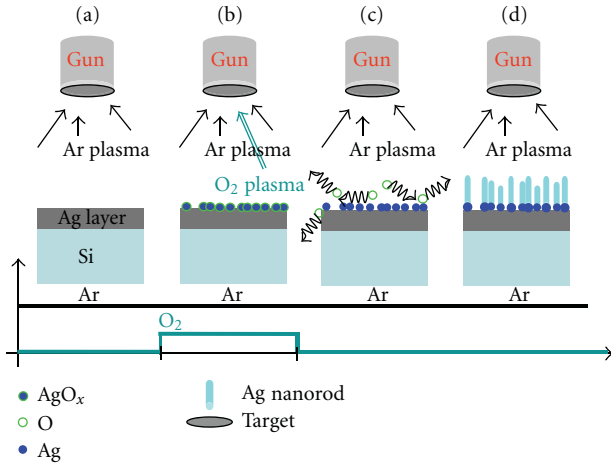


FIGURE 1: Growth mechanism of Ag nanorod arrays during sputtering process.

nanorods arrays using a two-step mixed gaseous process. The success of the technique provides support for the oxidation reduction growth (ORG) mechanism and proves suitable for fabrication of Ag nanorods in the semiconductor industry.

2. Experiment

Prior to sputtering, a p-Si (100) substrate was first cleaned in acetone and then cleaned in isopropanol for 300 s. The p-Si substrate was then dipped into hydrofluoric acid to remove the native oxide and finally rinsed with deionized water. For RF sputtering, the cleaned p-Si was loaded into the sputter chamber to perform sputtering, and the distance between the sample surface and silver target was approximately 3 cm.

The RF sputter system was evacuated to below 1.8×10^{-4} Torr, and argon gas was introduced with the flow rate controlled at 15 sccm. The gas pressure was fixed at 15×10^{-3} Torr during the sputtering process, and the RF power was set at 80 W. The sputtering times are 20 and 30 min for silver oxide clusters and silver nanorods, respectively. The deposition rates of silver, silver oxide, and nanorods are 3, 1, and 10 nm/min, respectively. The amount of the introduced oxygen is 1 sccm during reactive sputtering.

A schematic diagram for the oxidation reduction growth of silver nanorods is illustrated in Figure 1. The whole sputtering process was continuous without venting until Ag nanorods had grown. In Figure 1(a), at the beginning of sputtering, a thin silver film was predeposited on the Si surface with a constant flow of 15 sccm argon gas. Next, a trace of oxygen was introduced and mixed with argon as the source of plasma to form the silver oxide seed during sputtering, as shown in Figure 1(b). The silver oxide seed randomly dispersed over the Ag buffer layer and was able to form the contiguous thin film due to the trace amounts of oxygen. Notably, the melting point of silver oxide is normally approximately 300°C and even lower at the nanoscale [8]. When engaged in the sputtering process, the temperature of the sample will rise to between 200°C and 300°C allowing silver oxide to dissolve and release O_2 and return the silver

to the original silver oxide site (Figure 1(c)). In Figure 1(d), sputtering is performed without oxygen, and the silver nanorods start to grow from the reduction metal silver site. The oxidation reduction growth (ORG) of silver nanorods is a novel and continual process, which uses sputtering.

The morphology of the Ag nanorods was investigated by scanning electron microscopy (SEM), and the crystallization of the silver nanorods and silver oxide seeds were examined using X-ray diffraction (XRD). The incident angle of X-ray was fixed 1° for the phase identification of the extreme surface. For the detailed structure, the orientation was detected by transmission electron microscopy (TEM), and the selected area electron diffraction (SAED) was observed on the body of the nanorods and the silver buffer layer. For PL measurements, a 405 nm laser was used as an excitation light, and detection was performed in a photomultiplier tube.

3. Results and Discussions

Figure 2 shows tilted view SEM images and glancing angle XRD for the silver oxide seeds under sputtering 20 min and Ag nanorods under sputtering 30 min. As shown in Figures 2(a) and 2(b), not only were the silver oxide seeds observed but also the Ag nanorods uniformly distributed over the sample surface. Notably, the density of the silver oxide seeds was approximately $150/\mu\text{m}^2$, approaching that of Ag nanorods. The range for the diameters of the Ag nanorods was from 40 to 55 nm while the diameter of the silver oxide seeds was approximately 60 nm. The average diameter of the Ag nanorods was slightly smaller than that of the silver oxide seeds.

The energy dispersive spectrometer (EDS) data of the Ag nanorods is exhibited in Figure 2(c). A main peak of silver and a weak oxygen signal can be observed on the spectrum. According to the ratio of weight between Ag and oxygen, most of the peaks were Ag, and these were initially identified as pure Ag nanorods. The inset of Figure 2(c) is a cross section view of the Ag nanorods using a focused ion beam and most of the Ag nanorods aligned to the substrate. A silver buffer layer existed beneath the Ag nanorods, and this result is consistent with previous reports (not the present growth method) that one-dimensional aligned nanostructures also require the same material layer to grow due to the lattice match [30–33]. The thickness of the present Ag buffer layer was about 45 nm, and the length of the Ag nanorods was from 250 to 300 nm.

The crystallization of both the silver oxide nanoseeds and Ag nanorods was investigated using glancing angle XRD. Figure 2(d) shows the main Ag peaks, including (111), (200), (220), and (311), which coincide with the thin silver film [34]. In Ag nanorods case, all signals really came from Ag nanorods due to glancing angle XRD with 1° incidence, but the peaks of Ag signal in silver oxide nanoseeds resulted from the Ag buffer layer. Notably, the signal of silver oxide ($11\bar{1}$) appears at 28° in some of the silver oxide nanoclusters in addition to the Ag peaks. The silver oxide phase was Ag_3O_4 and was produced during the mixed-gas sputtering process with the input of oxygen [35, 36]. After the thermal

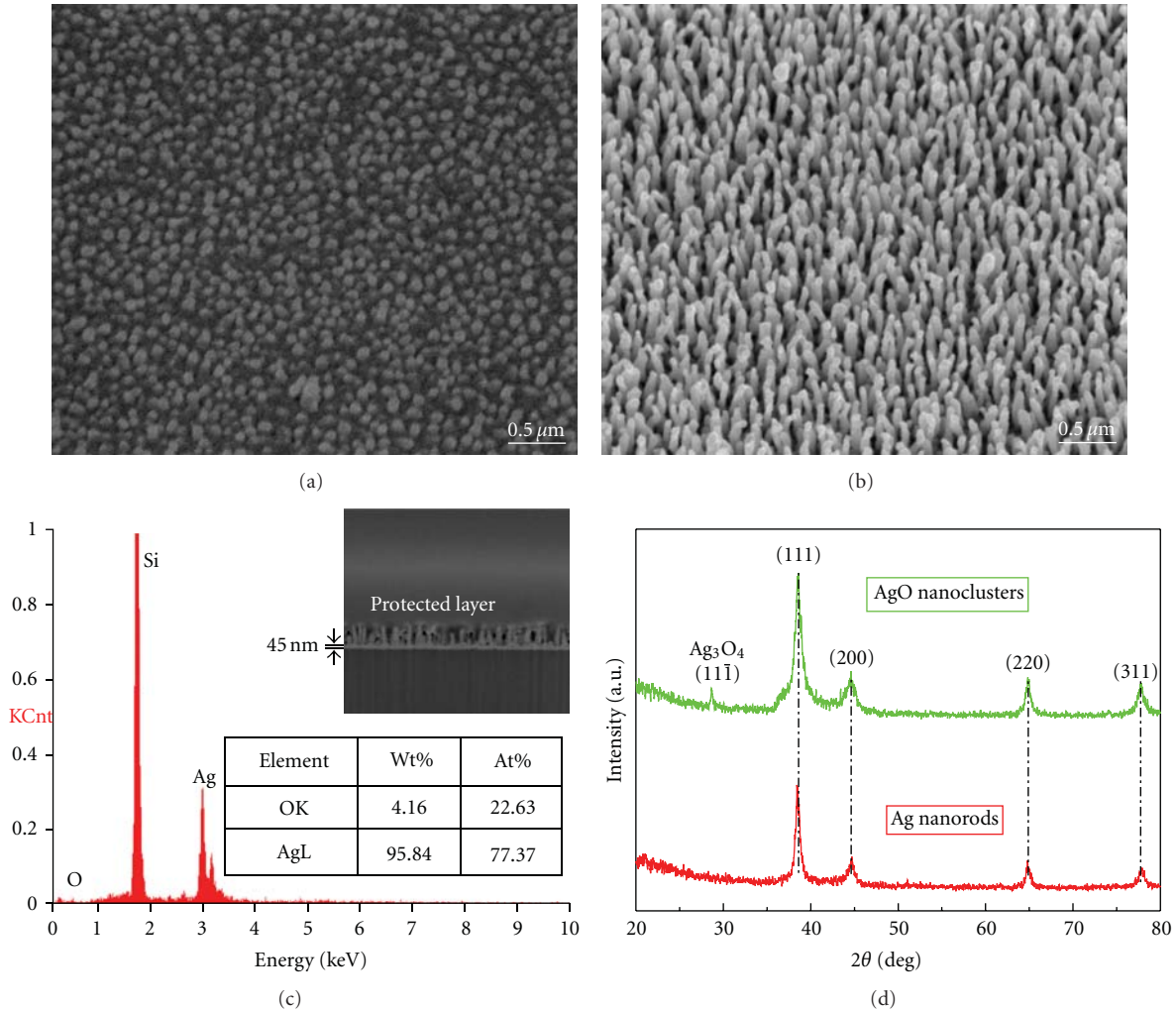


FIGURE 2: SEM images of (a) silver oxide nuclei, (b) Ag nanorod arrays, (c) EDS of Ag nanorods. The inset SEM image is a cross-section of Ag nanorods. (d) XRD spectra of Ag nanorods and silver oxide clusters.

decomposition, the oxygen resulting from the reduction reaction of silver oxides was pumped out. In addition, the production of silver oxides reduced metallic silver seeds for the growth of Ag nanorods. However, when the Ag_3O_4 phase is compared with the AgO phase, the Ag_3O_4 phase is more thermodynamically unstable (lower free energy) [37, 38]; therefore, the Ag_3O_4 can easily react in the consequent sputtering process to induce the growth of Ag nanorods with a chemical reaction of $\text{Ag}_3\text{O}_{4(s)} \rightarrow 3\text{Ag}_{(s)} + 2\text{O}_{2(g)}$ [39]. This two-step oxidation reduction process is responsible for the growth of the nanorods. Therefore, the present oxidation reduction growth (ORG) mechanism can also be applied to other metal systems with low melting point [40].

Figure 3(a) shows TEM observations with Ag nanorods aligned to the Ag buffer layer, and the corresponding SAED pattern from the white circle zone is shown in Figure 3(b). According to the electron diffraction pattern, the Ag nanorods were ascertained to be the single-crystal structure; the high resolution TEM image is shown in Figure 3(c). Additionally, the Ag nanorods grow from the thermal-reduced

Ag nucleus above the Ag buffer layer. A lattice image of the interfacial layer between the Ag nanorods and the grain is shown in the Figure 3(d), which demonstrates a perfect lattice arrangement. Figure 3(b) also shows that the Ag nanorods are crystalline and the interface zones between the Ag nanorods and the thermal-reduced Ag nucleus are coherent. From the cross-section observation, the Ag buffer layer was composed of many silver grains and this result was coincident with the phases of XRD spectra (Figure 2(d)). Notably, the Ag nanorods of the ORG structure also possessed excellent properties.

A PL spectrum of the Ag nanorod arrays under the irradiation of a 408 nm laser could be seen in Figure 4. The spectra ranges of all samples, which exhibit the strongest intensity near 2.17 eV, were from ~1.9 to ~2.45 eV. Basically, PL peaks in the visible wavelength can be regarded as a radiative recombination between Fermi level electrons and *sp*- or *d*-band holes [39, 41]. However, silver oxide forms easily in air and it may also provide a possible route of luminescence for photoreduced metallic Ag under visible

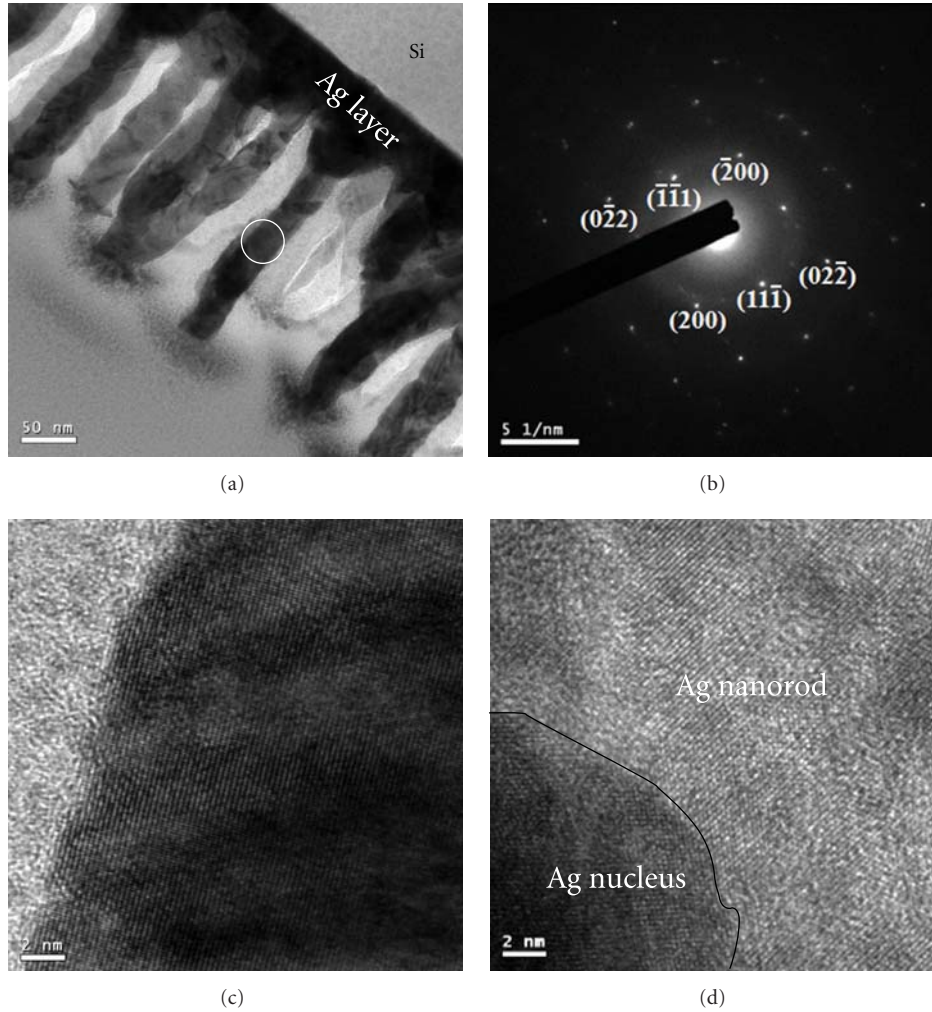


FIGURE 3: (a) A typical TEM image of Ag nanorods. (b) SAED of the white circle in (a), (c) the HRTEM image of Ag nanorod, (d) the interface between Ag nanorod and reduced metal nucleus.

illumination [27, 42]. Herein, PL spectrum of Ag nanorods was also measured under the vacuum to avoid the formation of silver oxide during the irradiation of laser in air, and there is no shift for the spectra of Ag nanorods both in air and in vacuum.

4. Conclusion

In summary, Ag nanorods were fabricated using an oxidation reduction growth (ORG) method by sputtering without catalysts or chemical solutions. The Ag nanorods grew in the original locations of reduced metal nuclei after thermal composition of silver oxide nanoclusters. The Ag nanorods stood vertically on the Ag buffer interlayer and grew from the interface between the Ag grains and the Ag buffer interlayer. PL spectra of Ag nanorods both in air and vacuum were observed at 2.17 eV due to the photoactivation caused by a radiative recombination of Fermi level electrons and d-band holes.

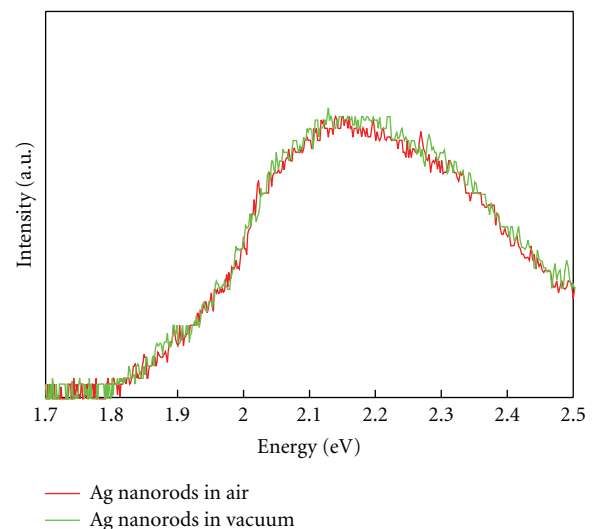


FIGURE 4: Room temperature PL spectra of Ag nanorods and silver oxide clusters.

Acknowledgments

The authors are grateful to The Instrument Center of National Cheng Kung University, the Center for Micro/Nano Science and Technology (D101-2700) and NSC 100-2221-E-006-093; NSC 100-2221-E-006-094; NSC 100-2622-E-006-030-CC for the financial support.

References

- [1] J. I. Pascual, J. Méndez, J. Gómez-Herrero et al., "Properties of metallic nanowires: from conductance quantization to localization," *Science*, vol. 267, no. 5205, pp. 1793–1795, 1995.
- [2] M. C. Daniel and D. Astruc, "Gold Nanoparticles: assembly, supramolecular chemistry, quantum-size-related properties, and applications toward biology, catalysis, and nanotechnology," *Chemical Reviews*, vol. 104, no. 1, pp. 293–346, 2004.
- [3] A. R. Tao and P. Yang, "Polarized surface-enhanced Raman spectroscopy on coupled metallic nanowires," *Journal of Physical Chemistry B*, vol. 109, no. 33, pp. 15687–15690, 2005.
- [4] I. R. Gould, J. R. Lenhard, A. A. Muentner, S. A. Godleski, and S. Farid, "Two-electron sensitization: a new concept for silver halide photography," *Journal of the American Chemical Society*, vol. 122, no. 48, pp. 11934–11943, 2000.
- [5] B. J. Murray, E. C. Walter, and R. M. Penner, "Amine vapor sensing with silver mesowires," *Nano Letters*, vol. 4, no. 4, pp. 665–670, 2004.
- [6] Y. Sun, "Conversion of Ag nanowires to AgCl nanowires decorated with Au nanoparticles and their photocatalytic activity," *Journal of Physical Chemistry C*, vol. 114, no. 5, pp. 2127–2133, 2010.
- [7] U. Lee, S. Ham, C. Han, Y. J. Jeon, N. Myung, and K. Rajeshwar, "Mild and facile synthesis of Ag₂S nanowire precursor using mercaptoacetic acid as a reductant/stabilizer and its subsequent conversion to Ag₂S or CdS nanowires," *Materials Chemistry and Physics*, vol. 121, no. 3, pp. 549–554, 2010.
- [8] G. I. N. Waterhouse, G. A. Bowmaker, and J. B. Metson, "The thermal decomposition of silver (I, III) oxide: a combined XRD, FT-IR and Raman spectroscopic study," *Physical Chemistry Chemical Physics*, vol. 3, no. 17, pp. 3838–3845, 2001.
- [9] Q. Zhou, Y. Yang, J. Ni, Z. Li, and Z. Zhang, "Rapid recognition of isomers of monochlorobiphenyls at trace levels by surface-enhanced Raman scattering using Ag nanorods as a substrate," *Nano Research*, vol. 3, no. 6, pp. 423–428, 2010.
- [10] P. H. C. Camargo, C. M. Cobley, M. Rycenga, and Y. Xia, "Measuring the surface-enhanced Raman scattering enhancement factors of hot spots formed between an individual Ag nanowire and a single Ag nanocube," *Nanotechnology*, vol. 20, no. 43, Article ID 434020, 2009.
- [11] Y. J. Liu, Z. Y. Zhang, Q. Zhao, R. A. Dluhy, and Y. P. Zhao, "Surface enhanced Raman scattering from an Ag nanorod array substrate: the site dependent enhancement and layer absorbance effect," *Journal of Physical Chemistry C*, vol. 113, no. 22, pp. 9664–9669, 2009.
- [12] W. Wei, L. Shuzhou, Q. Lidong et al., "Surface Plasmon-Mediated energy transfer in heterogap Au-Ag nanowires," *Nano Letters*, vol. 8, no. 10, pp. 3446–3449, 2008.
- [13] J. Zhu, "Surface plasmon resonance from bimetallic interface in Au-Ag core-shell structure nanowires," *Nanoscale Research Letters*, vol. 4, no. 9, pp. 977–981, 2009.
- [14] P. Cheng, D. Li, X. Li, T. Liu, and D. Yang, "Localized surface plasmon enhanced photoluminescence from ZnO films: extraction direction and emitting layer thickness," *Journal of Applied Physics*, vol. 106, no. 6, Article ID 063120, 2009.
- [15] J. Xu, G. A. Cheng, and R. T. Zheng, "Controllable synthesis of highly ordered Ag nanorod arrays by chemical deposition method," *Applied Surface Science*, vol. 256, no. 16, pp. 5006–5010, 2010.
- [16] C. Chen, L. Wang, G. Jiang et al., "The influence of seeding conditions and shielding gas atmosphere on the synthesis of silver nanowires through the polyol process," *Nanotechnology*, vol. 17, no. 2, pp. 466–474, 2006.
- [17] C. J. Murphy and N. R. Jana, "Controlling the aspect ratio of inorganic nanorods and nanowires," *Advanced Materials*, vol. 14, no. 1, pp. 80–82, 2002.
- [18] Y. P. Zhao, S. B. Chaney, and Z. Y. Zhang, "Absorbance spectra of aligned Ag nanorod arrays prepared by oblique angle deposition," *Journal of Applied Physics*, vol. 100, no. 6, Article ID 063527, 2006.
- [19] P. Mohanty, I. Yoon, T. Kang et al., "Simple vapor-phase synthesis of single-crystalline Ag nanowires and single-nanowire surface-enhanced Raman scattering," *Journal of the American Chemical Society*, vol. 129, no. 31, pp. 9576–9577, 2007.
- [20] U. Schürmann, W. Hartung, H. Takele, V. Zaporozhchenko, and F. Faupel, "Controlled syntheses of Ag-polytetrafluoroethylene nanocomposite thin films by co-sputtering from two magnetron sources," *Nanotechnology*, vol. 16, no. 8, pp. 1078–1082, 2005.
- [21] D. K. Avasthi, Y. K. Mishra, D. Kabiraj, N. P. Lalla, and J. C. Pivin, "Synthesis of metal-polymer nanocomposite for optical applications," *Nanotechnology*, vol. 18, no. 12, Article ID 125604, 2007.
- [22] Y. T. Lin, C. Y. Chen, C. P. Hsiung, K. W. Cheng, and J. Y. Gan, "Growth of RuO₂ nanorods in reactive sputtering," *Applied Physics Letters*, vol. 89, no. 6, Article ID 063123, 2006.
- [23] K. W. Cheng, Y. T. Lin, C. Y. Chen et al., "In situ epitaxial growth of TiO₂ on RuO₂ nanorods with reactive sputtering," *Applied Physics Letters*, vol. 88, no. 4, Article ID 043115, pp. 1–3, 2006.
- [24] X. M. Meng, J. Q. Hu, Y. Jiang, C. S. Lee, and S. T. Lee, "Oxide-assisted growth and characterization of Ge/SiO_x nanocables," *Applied Physics Letters*, vol. 83, no. 11, pp. 2241–2243, 2003.
- [25] R. Q. Zhang, Y. Lifshitz, and S. T. Lee, "Oxide-assisted growth of semiconducting nanowires," *Advanced Materials*, vol. 15, no. 7–8, pp. 635–640, 2003.
- [26] C. L. Pint, S. T. Pheasant, A. N. G. Parra-Vasquez, C. Horton, Y. Xu, and R. H. Hauge, "Investigation of optimal parameters for oxide-assisted growth of vertically aligned single-walled carbon nanotubes," *Journal of Physical Chemistry C*, vol. 113, no. 10, pp. 4125–4133, 2009.
- [27] L. A. Peyser, A. E. Vinson, A. P. Bartko, and R. M. Dickson, "Photoactivated fluorescence from individual silver nanoclusters," *Science*, vol. 291, no. 5501, pp. 103–106, 2001.
- [28] M. Nirmal and L. Brus, "Luminescence photophysics in semiconductor nanocrystals," *Accounts of Chemical Research*, vol. 32, no. 5, pp. 407–414, 1999.
- [29] A. Borrás, M. Maclas-Montero, P. Romero-Gomez, and A. R. Gonzalez-Elipe, "Supported plasma-made 1D heterostructures: perspectives and applications," *Journal of Physics D*, vol. 44, no. 17, Article ID 174016, 2011.
- [30] H. Jung, R. Kuljic, M. A. Stroschio, and M. Dutta, "Confinement in PbSe wires grown by rf magnetron sputtering," *Applied Physics Letters*, vol. 96, no. 15, Article ID 153106, 2010.
- [31] S. W. Kang, S. K. Mohanta, Y. Y. Kim, and H. K. Cho, "Realization of vertically well-aligned ZnO:Ga nanorods by magnetron

- sputtering and their field emission behavior,” *Crystal Growth and Design*, vol. 8, no. 5, pp. 1458–1460, 2008.
- [32] C. Li, G. Fang, L. Yuan et al., “Field emission from carbon nanotube bundle arrays grown on self-aligned ZnO nanorods,” *Nanotechnology*, vol. 18, no. 15, Article ID 155702, 2007.
- [33] M. Suzuki, K. Nagai, S. Kinoshita et al., “Vapor phase growth of Al whiskers induced by glancing angle deposition at high temperature,” *Applied Physics Letters*, vol. 89, no. 13, Article ID 133103, 2006.
- [34] S. Iida, T. Okui, T. Tai, and S. Akao, “Thin Ag film formation onto Si/SiO₂ substrate,” *Applied Surface Science*, vol. 166, no. 1, pp. 160–164, 2000.
- [35] Z. S. Hu, F. Y. Hung, S. J. Chang et al., “Effects of Ag nanoshape and AgGa phase in Ag-Si nanostructure using 2-step etching process,” *Journal of Alloys and Compounds*, vol. 509, no. 3, pp. 758–763, 2011.
- [36] Z.-S. Hu, F.-Y. Hung, S.-J. Chang, K.-J. Chen, and Y.-Z. Chen, “Crystallization effect of Al-Ag alloying layer in PL enhancement of ZnO thin film,” *Intermetallics*, vol. 18, no. 8, pp. 1428–1431, 2010.
- [37] R. O. Suzuki, T. Ogawa, and K. Ono, “Use of ozone to prepare silver oxides,” *Journal of the American Ceramic Society*, vol. 82, no. 8, pp. 2033–2038, 1999.
- [38] T. Rosenqvist, *Principles of Extractive Metallurgy*, McGraw-Hill, New York, NY, USA, 1974.
- [39] G. I. N. Waterhouse, J. B. Metson, and G. A. Bowmaker, “Synthesis, vibrational spectra and thermal stability of Ag₃O₄ and related Ag₇O₈X salts (X = NO₃⁻, ClO₄⁻, HSO₄⁻),” *Polyhedron*, vol. 26, no. 13, pp. 3310–3322, 2007.
- [40] V. I. Yukhvid, S. V. Maklakov, P. V. Zhirkov, V. A. Gorshkov, N. I. Timokhin, and A. Y. Dovzhenko, “Combustion synthesis and structure formation in a model Cr-CrO₃ self-propagating high-temperature synthesis system,” *Journal of Materials Science*, vol. 32, no. 7, pp. 1915–1924, 1997.
- [41] R. Sarkar, P. Kumbhakar, A. K. Mitra, and R. A. Ganeev, “Synthesis and photoluminescence properties of silver nanowires,” *Current Applied Physics*, vol. 10, no. 3, pp. 853–857, 2010.
- [42] C. Bürgel, R. Mitrić, and V. Bonacic-Koutecky, “Emissive properties of silver particles at silver oxide surface defects,” *Applied Physics A*, vol. 82, no. 1, pp. 117–123, 2006.

Research Article

Thermal Stability of Neodymium Aluminates High- κ Dielectric Deposited by Liquid Injection MOCVD Using Single-Source Heterometallic Alkoxide Precursors

P. Taechakumput,¹ C. Z. Zhao,^{1,2} S. Taylor,¹ M. Werner,³ P. R. Chalker,³ J. M. Gaskell,⁴
H. C. Aspinall,⁴ A. C. Jones,⁴ and Susu Chen¹

¹ Department of Electrical Engineering and Electronics, University of Liverpool, Liverpool L69 3GJ, UK

² Department of Electrical and Electronic Engineering, Xi'an Jiaotong-Liverpool University, Suzhou 215123, China

³ Department of Engineering, Materials Science and Engineering, University of Liverpool, Liverpool L69 3GH, UK

⁴ Department of Chemistry, University of Liverpool, Liverpool L69 3ZD, UK

Correspondence should be addressed to C. Z. Zhao, cezhou.zhao@xjtlu.edu.cn

Received 7 December 2011; Accepted 8 February 2012

Academic Editor: Mohammad H. Maneshian

Copyright © 2012 P. Taechakumput et al. This is an open access article distributed under the Creative Commons Attribution License, which permits unrestricted use, distribution, and reproduction in any medium, provided the original work is properly cited.

Thin films of neodymium aluminate (NdAlO_x) have been deposited by liquid injection metalorganic chemical vapor deposition (MOCVD) using the bimetallic alkoxide precursor $[\text{NdAl}(\text{OPr}^i)_6(\text{Pr}^i\text{OH})]_2$. The effects of high-temperature postdeposition annealing on NdAlO_x thin films are reported. The as-deposited thin films are amorphous in nature. X-ray diffraction (XRD) and medium energy ion scattering (MEIS) show, respectively, no crystallization or interdiffusion of metal ions into the substrate after annealing at 950°C . The capacitance-voltage (C - V) and current-voltage (I - V) characteristics of the thin films exhibited good electrical integrity following annealing. The dielectric permittivity (κ) of the annealed NdAlO_x was 12, and a density of interface states at flatband (D_{it}) of $4.01 \times 10^{11} \text{ cm}^{-2} \text{ eV}^{-1}$ was measured. The deposited NdAlO_x thin films are shown to be able to endure high-temperature stress and capable of maintaining excellent dielectric properties.

1. Introduction

Recently, considerable effort has been exerted in developing high- κ rare earth oxide, M_2O_3 ($\text{M} = \text{La}, \text{Pr}, \text{Nd}, \text{etc.}$), as a replacement of the conventional SiO_2 -based gate dielectric material [1]. The incorporation of neodymium (Nd) ions in insulating layers has important applications for solid-state laser materials, luminescent materials, protective coatings, and gate dielectric applications [2, 3]. However, Nd_2O_3 is thermally unstable upon annealing and can be partially transformed to $\text{NdO}(\text{OH})$ when exposed to atmospheric conditions [4]. One of many solutions to enhance the thermal stability is the incorporation of aluminium (Al) to develop innovative multifunctional advanced lanthanide-aluminates-based ceramics, MAlO_3 ($\text{M} = \text{La}, \text{Pr}, \text{Gd}, \text{and Nd}$). The lanthanide aluminates are promising high- κ candidates as they combine the advantages of the high permittivity

of the lanthanide oxide with the chemical and thermal stability of Al_2O_3 . Furthermore, they remain amorphous up to high temperatures, leading to a large reduction in leakage current relative to polycrystalline M_2O_3 films during CMOS processing [5, 6].

Work on NdAlO_x was mostly reported as a ceramic material for microwave applications and as a diffusion barrier in solid-oxide fuel cells [7, 8]. Growth of NdAlO_x thin films have previously been achieved by various deposition methods, including pulsed laser deposition [9], chemical vapor deposition [10, 11], e-beam evaporation [8], and atomic layer deposition [4]. To date, however, little is still known about the physical and electronic characteristics of NdAlO_x due to a lack of suitable precursors with appropriate stability, volatility, and decomposition characteristics. This has motivated us to further exploit these perovskite thin films

for gate dielectric applications using an alternative single-source precursor. The use of single-source precursor allows better mixing of the components at atomic level, significantly lower decomposition temperature, and free from halide ions contamination [11].

In this work, the effects of high-temperature postdeposition annealing (PDA) on the properties of the NdAlO_x thin films, deposited by metalorganic chemical vapor deposition (MOCVD) using single-source precursor, were studied.

2. Experimental

Near stoichiometric NdAlO_x thin films ($\text{Nd/Al} = 0.87$) were deposited on n-type silicon (100) substrates by liquid injection MOCVD at 450°C on an Aixtron AIX 200FE AVD reactor fitted with the “TriJet”TM liquid injector system [12], utilizing the single-source precursor $[\text{NdAl}(\text{OPr}^i)_6(\text{Pr}^i\text{OH})]_2$. Selected films were subjected to high-temperature (750 – 950°C) postdeposition annealing (PDA) in pure nitrogen (N_2) ambient for 60 seconds. Subsequently, a postmetallization forming gas anneal (FGA) was carried out at 400°C for 30 minutes using $\text{H}_2:\text{N}_2$ in the ratio 1:9, together with a control as-deposited sample.

X-ray diffraction (XRD) was performed on the studied films using nickel-filtered $\text{Cu K}\alpha$ radiation ($\lambda = 1.5405 \text{ \AA}$) with a 2θ increment of 0.2° per second. The samples were scanned over a $\theta/2\theta$ range of 20° to 40° . Medium energy ion scattering (MEIS) experiments were carried out using a nominal 200 keV He^+ ion beam and a 70.5° scattering angle. Cross-section transmission electron microscopy (TEM) was carried out using a JEOL 2000 FX operated at 500 kV. Capacitance-voltage (C - V) measurements were conducted on the MOS capacitors of the structure ($\text{Au}/\text{NdAlO}_x/\text{SiO}_2/\text{n-Si}$) using a HP4192 impedance analyzer, with 30 mV RMS probe signal, at various frequencies (1 kHz–1 MHz). Leakage current (I - V) measurements were obtained using a Keithley K230 programmable voltage source and a 617 type electrometer.

3. Results and Discussion

Phase transitions of the gate dielectric, as a function of PDA temperatures, were accessed by X-ray diffraction (XRD). The X-ray diffraction traces of the as-deposited and PDA samples (regardless of PDA temperature) exhibited a diffraction peak consistent with the (200) peak from the silicon substrate. No other diffraction features were observed (Figure 1(a)), suggesting that they were essentially amorphous. In addition, MEIS results indicated that no significant level of crystallinity or movement of metal ions was in evidence in the 950°C PDA film as demonstrated in Figure 1(b).

Figure 2 shows TEM micrographs in which the thicknesses of the high- κ stack, including the interfacial layer, were evaluated. The high- κ thickness and a thin native oxide interlayer, adjacent to the silicon substrate, changed from 11 nm and 1.5 nm, respectively, and to 10.4 nm and 2.5 nm respectively, after 950°C PDA. This could be due to interdiffusion of oxygen between SiO_2 and NdAlO_x . The growth

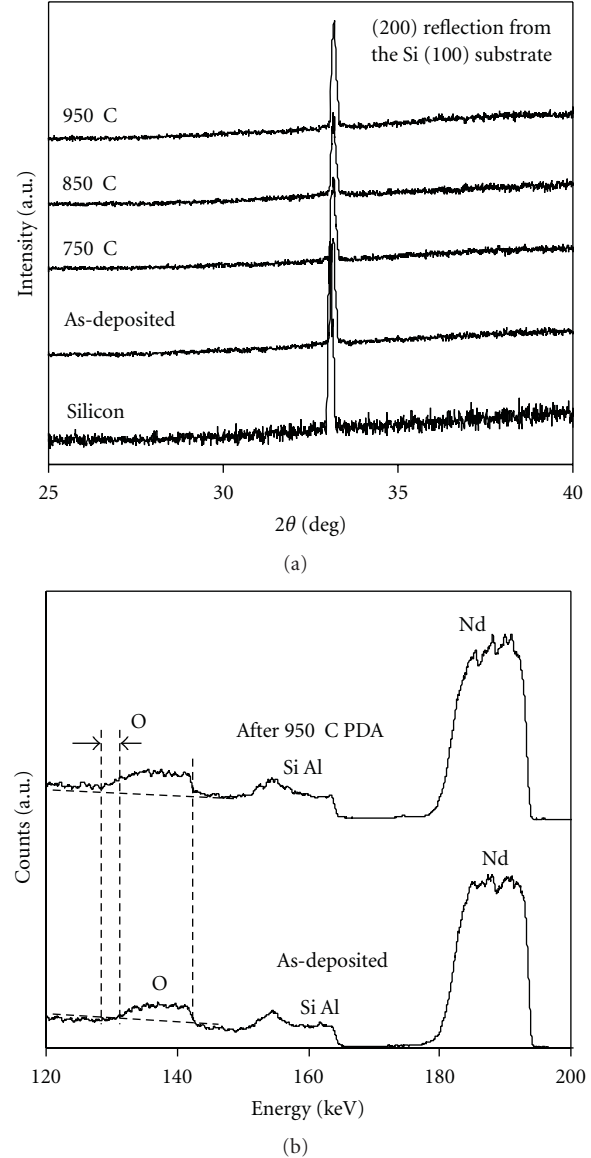


FIGURE 1: (a) X-ray diffraction traces for $\text{NdAlO}_x/\text{SiO}_2$ stacks as a function of RTA temperatures. (b) A comparison of MEIS data of a $\text{NdAlO}_x/\text{SiO}_2$ stack prior to and after RTA in pure N_2 ambient for 1 min.

of the SiO_2 layer, following annealing, is also visible in the MEIS energy spectrum (Figure 1(b)). The amorphous nature of the thin films is also observed in the TEM analysis (Figure 2) confirming the XRD findings.

The high-frequency C - V characteristics of as-deposited and PDA samples are shown in Figure 3. Both as-deposited and PDA samples exhibited small counter-clockwise hysteresis ($<0.1 \text{ V}$). A positive shift of flatband voltage (V_{FB}) (the shift of V_{FB} is 0.97 V) in the as-deposited sample was observed and contributed to fixed negative oxide charges. However, a near-ideal flatband voltage ($V_{\text{FB}} = 0.65 \text{ V}$) was obtained in the 950°C PDA sample. This may indicate that negative fixed oxide charges could be compensated by nitrogen-induced positive fixed oxide charges generated

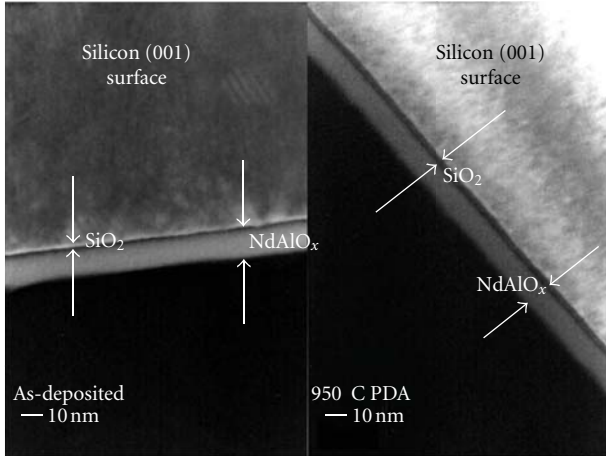


FIGURE 2: TEM image of the as-deposited and 950°C PDA $\text{NdAlO}_x/\text{SiO}_2$ stacks shows the thicknesses of oxide layers change from 1.5 nm/11 nm to 2.5 nm/10.4 nm, respectively.

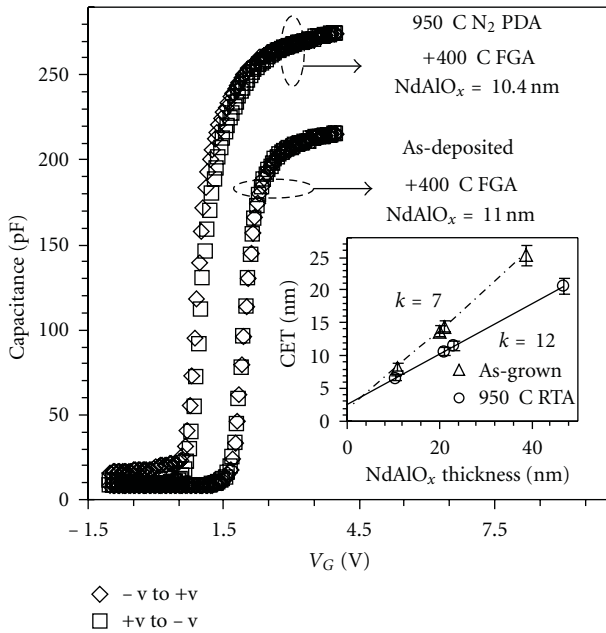


FIGURE 3: A comparison of high-frequency C - V curves with and without N_2 PDA treatment. MOSCs with $[\text{Au}/\text{NdAlO}_x/\text{SiO}_2/\text{n-Si}/\text{Al}]$ structure were fabricated with an effective area of $4.9 \times 10^{-4} \text{ cm}^2$. The inset is a plot of capacitance equivalent thickness (CET) versus NdAlO_x physical thickness, which shows an increase in the dielectric permittivity (7 to 12) and changes of the interfacial layer (1.5 to 2.5 nm) after PDA treatment.

during annealing at the $\text{NdAlO}_x/\text{SiO}_2$ interface. Terman analysis [13] yields an interface density of states, D_{it} , of $4.94 \times 10^{11} \text{ cm}^{-2} \text{ eV}^{-1}$ and $4.01 \times 10^{11} \text{ cm}^{-2} \text{ eV}^{-1}$ at midgap for as-deposited and 950°C PDA samples, respectively. This is lower than D_{it} of other recent high- κ candidates, D_{it} of $2.5 \times 10^{12} \text{ cm}^{-2} \text{ eV}^{-1}$ found in $\text{La}_{1.3}\text{Hf}_{1.0}\text{O}_{4.1}$ [14], but higher than the interface state density of $5 \times 10^{10} \text{ cm}^{-2} \text{ eV}^{-1}$ shown by $\text{Y}_x\text{Hf}_{1-x}\text{O}_y$ ($x = 0.065$) [15].

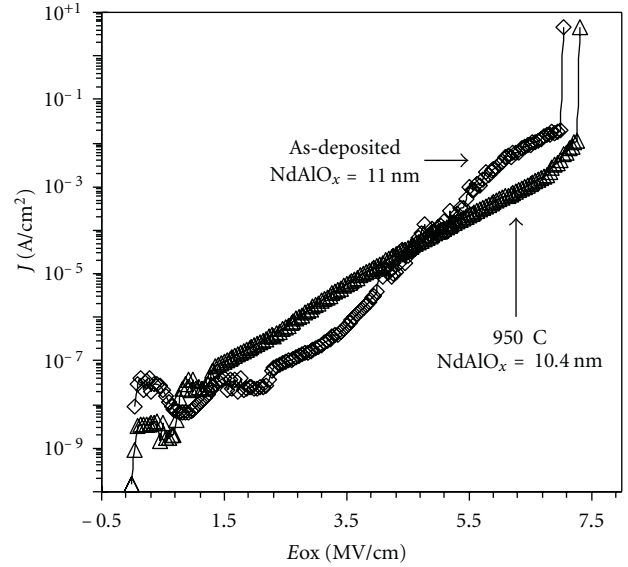


FIGURE 4: Leakage current density (J) versus electric field (E_{ox}) applied across the $\text{NdAlO}_x/\text{SiO}_2$ stacks as a function of PDA temperatures. The NdAlO_x films thickness was $t_{\text{high-}\kappa} \sim 10.4$ to 11 nm.

Despite an increase of the interfacial layer in the PDA samples, the measured capacitance in strong accumulation was found to be higher than that of the as-deposited samples. The inset of Figure 3 shows a plot of the high- κ dielectric thickness against capacitance equivalent thickness (CET). The slope revealed the NdAlO_x dielectric permittivity (κ) to be 7 and 12 in the as-deposited and 950°C PDA films, respectively. The increase of dielectric permittivity (κ), observed after receiving thermal treatment, could be due to a small change of the crystal symmetry, with the formation of some small nanometer scale crystallites with higher permittivity phases of NdAlO_x [16, 17].

The leakage current densities (J) at 2 MV cm^{-1} in all samples, even after 950°C PDA, were below $1 \times 10^{-7} \text{ A cm}^{-2}$ (Figure 4), which is comparable with other leading edge high- κ dielectrics [18]. The average breakdown, regardless the annealing treatment, also occurs at the equivalent field strength of 7 MV cm^{-1} .

4. Conclusions

The NdAlO_x thin films deposited by liquid injection MOCVD have been shown to remain amorphous up to 950°C as shown by XRD analysis. No significant level of crystallinity or movements of metal ions was also in evidence after annealing at 950°C as indicated in MEIS energy spectra. Electrical properties of NdAlO_x samples, after high-temperature annealing, were presented. Good electrical integrity was maintained even after 950°C PDA as shown by C - V and I - V results, showing the extracted dielectric permittivity of 12, a low leakage density of $7 \times 10^{-7} \text{ A cm}^{-2}$ at 2 MV cm^{-1} , and a density of interface states at flatband D_{it} of $4.01 \times 10^{11} \text{ cm}^{-2} \text{ eV}^{-1}$. These features

make the neodymium aluminate a potential candidate for the dielectric replacement.

Acknowledgments

This research was funded in part by the Engineering and Physical Science Research Council of UK under Grants nos. EP/D068606/1 and GR/S76632/01, from the National Natural and Science Foundation of China under the Grant no. 60976075, and from the Suzhou Science and Technology Bureau of China under the Grant no. SYG201007. Special appreciation is extended to Mr. Kevin Molloy for technical assistance with sample metallization, Dr. N. Pham for XRD measurements, and Mr. R. T. Murray for TEM measurements.

References

- [1] M. Leskelä and M. Ritala, "Rare-earth oxide thin films as gate oxides in MOSFET transistors," *Journal of Solid State Chemistry*, vol. 171, no. 1-2, pp. 170–174, 2003.
- [2] G. Bonnet, M. Lachkar, J. C. Colson, and J. P. Larpin, "Characterization of thin solid films of rare earth oxides formed by the metallo-organic chemical vapour deposition technique, for high temperature corrosion applications," *Thin Solid Films*, vol. 261, no. 1-2, pp. 31–36, 1995.
- [3] S. Chevalier, G. Bonnet, and J. P. Larpin, "Metal-Organic Chemical Vapor Deposition of Cr₂O₃ and Nd₂O₃ coatings. Oxide growth kinetics and characterization," *Applied Surface Science*, vol. 167, no. 3, pp. 125–133, 2000.
- [4] A. Kosola, J. Päiväsari, M. Putkonen, and L. Niinistö, "Neodymium oxide and neodymium aluminate thin films by atomic layer deposition," *Thin Solid Films*, vol. 479, no. 1-2, pp. 152–159, 2005.
- [5] J. M. Gaskell, A. C. Jones, H. C. Aspinall et al., "Liquid injection ALD and MOCVD of lanthanum aluminate using a bimetallic alkoxide precursor," *Journal of Materials Chemistry*, vol. 16, no. 39, pp. 3854–3860, 2006.
- [6] M. Nieminen, T. Sajavaara, E. Rauhala, M. Putkonen, and L. Niinistö, "Surface-controlled growth of LaAlO₃ thin films by atomic layer epitaxy," *Journal of Materials Chemistry*, vol. 11, no. 9, pp. 2340–2345, 2001.
- [7] E. A. Nenasheva, L. P. Mudroliubova, and N. F. Kartenko, "Microwave dielectric properties of ceramics based on CaTiO₃-LnMO₃ System (Ln-La, Nd; M-Al, Ga)," *Journal of the European Ceramic Society*, vol. 23, no. 14, pp. 2443–2448, 2003.
- [8] C. Brugnoni, U. Ducati, C. Chemelli, M. Scagliotti, and G. Chiodelli, "SOFC cathode/electrolyte interfaces. Part II: study of NdAlO₃ diffusion barriers," *Solid State Ionics*, vol. 76, no. 3-4, pp. 183–188, 1995.
- [9] M. Henini, "High quality YBa₂Cu₃O_{7-x}/NdAlO₃/YBa₂Cu₃O_{7-x} trilayers on (100) MgO for microwave applications," *Thin Solid Films*, vol. 306, no. 1, pp. 141–146, 1997.
- [10] S. Mathur, M. Veith, H. Shen, N. Lecerf, and S. Hüfner, "Effect of Al₂O₃ matrix on the optical properties of NdAlO₃ in NdAlO₃/Al₂O₃ ceramic-ceramic composite," *Scripta Materialia*, vol. 44, no. 8-9, pp. 2105–2109, 2001.
- [11] M. Veith, S. Mathur, N. Lecerf, K. Bartz, M. Heintz, and V. Huch, "Synthesis of a NdAlO₃/Al₂O₃ ceramic-ceramic composite by single-source precursor CVD," *Chemistry of Materials*, vol. 12, no. 2, pp. 271–274, 2000.
- [12] J. M. Gaskell, S. Przybylak, A. C. Jones et al., "Deposition of Pr- and Nd-aluminate by liquid injection MOCVD and ALD using single-source heterometallic alkoxide precursors," *Chemistry of Materials*, vol. 19, no. 19, pp. 4796–4803, 2007.
- [13] L. M. Terman, "An investigation of surface states at a silicon/silicon oxide interface employing metal-oxide-silicon diodes," *Solid State Electronics*, vol. 5, no. 5, pp. 285–299, 1962.
- [14] Y. F. Loo, S. Taylor, R. T. Murray, A. C. Jones, and P. R. Chalker, "Structural and electrical characterization of amorphous lanthanum hafnium oxide thin films," *Journal of Applied Physics*, vol. 99, no. 10, Article ID 103704, 2006.
- [15] E. Rauwel, C. Dubourdieu, B. Holländer et al., "Stabilization of the cubic phase of HfO₂ by y addition in films grown by metal organic chemical vapor deposition," *Applied Physics Letters*, vol. 89, no. 1, Article ID 012902, 2006.
- [16] S. Govindarajan, T. S. Boscke, P. Sivasubramani et al., "Higher permittivity rare earth doped HfO₂ for sub-45-nm metal-insulator-semiconductor devices," *Applied Physics Letters*, vol. 91, no. 6, Article ID 062906, 3 pages, 2007.
- [17] T. S. Boscke, S. Govindarajan, P. D. Kirsch et al., "Stabilization of higher-κ tetragonal HfO₂ by SiO₂ admixture enabling thermally stable metal-insulator-metal capacitors," *Applied Physics Letters*, vol. 91, no. 7, Article ID 072902, 3 pages, 2007.
- [18] C. Vahlas, "Cyclic atomic layer deposition of hafnium aluminate thin films using tetrakis(diethylamido)hafnium, trimethyl aluminum, and water," *Chemical Vapor Deposition*, vol. 12, no. 2-3, pp. 125–129, 2006.